INFORMATION TO USERS

This manuscript has been reproduced from the microfilm master. UMI films the text directly from the original or copy submitted. Thus, some thesis and dissertation copies are in typewriter face, while others may be from any type of computer printer.

The quality of this reproduction is dependent upon the quality of the copy submitted. Broken or indistinct print, colored or poor quality illustrations and photographs, print bleedthrough, substandard margins, and improper alignment can adversely affect reproduction.

In the unlikely event that the author did not send UMI a complete manuscript and there are missing pages, these will be noted. Also, if unauthorized copyright material had to be removed, a note will indicate the deletion.

Oversize materials (e.g., maps, drawings, charts) are reproduced by sectioning the original, beginning at the upper left-hand corner and continuing from left to right in equal sections with small overlaps.

Photographs included in the original manuscript have been reproduced xerographically in this copy. Higher quality 6" x 9" black and white photographic prints are available for any photographs or illustrations appearing in this copy for an additional charge. Contact UMI directly to order.

ProQuest Information and Learning
300 North Zeeb Road, Ann Arbor, MI 48106-1346 USA
800-521-0600

Microwave Detection of Breast Cancer:

a cylindrical configuration for confocal microwave imaging

by Elise C. Fear

B.A.Sc., University of Waterloo, 1995
M.A.Sc., University of Victoria, 1997

A Thesis Submitted in Partial Fulfillment of the
Requirements for the Degree of

DOCTOR OF PHILOSOPHY

in the Department of Electrical and Computer Engineering

We accept this thesis as conforming to the required standard.

Dr. M.A. Stuchly, Supervisor, (Department of Electrical and Computer Engineering)

Dr. J. Bornemann, Departmental Member, (Department of Electrical and Computer Engineering)

Dr. W.J.R. Hoefer, Departmental Member, (Department of Electrical and Computer Engineering)

Dr. D. Olesky, Outside Member, (Department of Computer Science)

Dr. F. Spelman, External Examiner (Department of Bioengineering, University of Washington)

Supervisor: Dr. M.A. Stuchly

Abstract

Microwave imaging creates images of electrical property distributions in tissue, and has promise for breast tumor detection due to the contrast in electrical properties of normal and malignant breast tissues and the accessibility of the breast for imaging. Confocal microwave imaging (CMI) is a recently introduced technique that avoids limitations associated with classical microwave imaging. CMI detects areas of increased scatter (e.g. tumors) by scanning the synthetic focus of an array of antennas through the breast. As the object is illuminated with ultra-wideband signals, this corresponds to computing time delays to the focal point, resulting in simple image reconstruction algorithms. Additionally, the resolution is determined primarily by the bandwidth of the illuminating signal, allowing for detection of small tumors with appropriate selection of this bandwidth. CMI appears to be a simple and effective technique for breast tumor detection. The development and evaluation of a new approach to confocal microwave imaging is the contribution of this thesis.

CMI was only very recently introduced, and many key issues need to be addressed. Most importantly, the CMI system must be designed for physical compatibility with the breast examination. The previously introduced CMI system is planar, and involves placing an array of antennas directly on the naturally flattened breast (of a woman who is lying on her back). In this thesis, a cylindrical CMI configuration is developed. A woman lies on her stomach, the breast extends through a hole in the examination table, and is immersed in a low-loss material. The breast is encircled by an array of antennas, which is placed at a distance from the skin. The cylindrical configuration is likely more appropriate for clinical implementation.

The development of cylindrical CMI involves design of appropriate sensing elements and development of image reconstruction algorithms. Construction of appropriate models and simulations of the system are required to test the feasibility of the proposed sensors and algorithms. The finite difference time domain (FDTD) method is well suited to these

feasibility studies, as ultra-wideband signals are efficiently simulated in the time domain. In this thesis, four alternative antenna designs are characterized with measures appropriate for ultra-wideband radiation and this specific imaging application. The selected antenna is scanned in a circle around the breast and at a distance from the skin. This is repeated for a number of rows at different heights in order to synthesize a cylindrical or conical array. The returns recorded at each antenna location are processed to reduce clutter, then synthetically focussed at points in the domain of interest. Results indicate that the proposed antenna and algorithms provide the capability to detect and localize (in three dimensions) small spherical tumors at reasonable depths in the breast models. The detection capability achieved with the cylindrical system is comparable to that obtained with the previously introduced planar system.

Examiners:

Dr. M.A. Stuchly, Supervisor, (Department of Electrical and Computer Engineering)

Dr. J. Bornemann, Departmental Member, (Department of Electrical and Computer Engineering)

Dr. W.J.R. Hoefer, Departmental Member, (Department of Electrical and Computer Engineering)

Dr. D. Olesky, Outside Member, (Department of Computer Science)

Dr. F. Spelman, External Examiner (Department of Bioengineering, University of Washington)

Table of Contents

List of Figures

List of Tables

Acknowledgements

I would like to acknowledge the support of the Natural Sciences and Engineering Research Council of Canada (PGS-B scholarship).

The Minerva High Performance Computing Facility at the University of Victoria was used to perform many of the simulations presented in this thesis. I am grateful to the University for allowing me to use this resource.

I would like to thank my supervisor, Maria Stuchly, for encouraging me to do a Ph.D. and for letting me change my mind about what I wanted to research. I am also grateful to Maria for her constant enthusiasm about my work, and all of the opportunities that she has given me to present this work and to pursue collaborative efforts.

Dr. Susan Hagness of the University of Wisconsin-Madison has been supportive of this work from the beginning, and I would like to thank her for all of her encouragement and advice. Thank you also to Susan and her graduate student, Xu Li, for making collaboration so much fun.

I thank my colleagues in the BioElec Lab for many interesting discussions and contributions to this work. In particular, I would like to thank Kris Caputa for endless patience, technical support and coffee, and Mike Potter for his good advice.

I would like to thank Nicole Fear for lending me her considerable artistic talents (Figures 3.3 and 3.4), and all of my family for their support throughout my Ph.D. studies. I also thank Rob Douglas for his encouragement, friendship and perspectives.

1 Introduction

1.1 Motivation

Breast cancer is the most prevalent cancer in women, as well as the second leading cause of death due to cancer in women [1]. Earlier detection results in more effective treatment and increased patient comfort, as demonstrated by the introduction of breast screening programs across Canada [8]. Mammography, or x-ray imaging of a compressed breast, is the imaging modality used in screening programs. Therefore, tumor detection is based on density differences between normal tissues and lesions. Mammography detects up to 95% of lesions in the breast [6], however has a positive predictive value of approximately 8% [8]. That is, only 8% of the abnormalities detected with mammography correspond to malignancies. Additional imaging or biopsy is generally required to determine the status of a suspicious lesion. Other issues include false negatives, discomfort due to breast compression, difficulty in imaging women with dense breasts (25% of the population [6]) and health concerns related to ionizing radiation exposure. The latter two issues are of particular concern to younger women. These factors have motivated the search for alternative or complementary screening methods.

Although many conventional medical imaging techniques have been proposed and investigated for breast cancer detection, no techniques have yet been identified as sensitive and cost effective enough to replace mammography. The specificity limitations of mammography are accepted in light of the high sensitivity of this method: the cost of missing a tumor is much greater than that of performing a biopsy on a benign lesion. New technologies proposed to replace mammography must have high sensitivity to the presence of tumors, as well as the ability to image tumors of diameter 3 mm and microcalcifications of diameter 0.2 mm [6]. Complementary technologies must be capable of discriminating benign and malignant lesions. While ultrasound is used to differentiate cysts from solid lesions, traditional medical imaging modalities have not succeeded in providing the complementary information needed. The lack of success with conventional medical imaging methods has generated interest in new approaches to

breast imaging. Microwave imaging creates images of electrical property distributions in tissue, and has promise for breast tumor detection due to the contrast in electrical properties of normal and malignant breast tissues. This contrast provides a strong physical basis for tumor detection. Additionally, microwave breast imaging does not involve exposure to ionizing radiation or uncomfortable breast compression.

Although microwave imaging of the human body has been of interest for years, it is only now approaching clinical use. Advances in image reconstruction algorithms and computational power have recently produced promising results from prototype systems. Even with improvements in reconstruction algorithms, images have resolution limited to about a tenth of a wavelength, resulting in difficulty with the detection of small (sub-cm) tumors. Resolution can be improved by increasing frequency, however this decreases the penetration of the microwaves. Confocal microwave imaging (CMI) is a recently introduced technique that detects areas of increased scatter (e.g. tumors) by scanning the synthetic focus of an array of antennas through the breast. The object is illuminated with ultra-wideband pulses, so synthetic focussing involves computing the time delay from each antenna to the focal point of interest. Therefore, the reconstruction algorithms are simple, and do not involve iterative approaches to image reconstruction algorithm that match measured data to data computed with a model. Such approaches are used in microwave imaging, as well as optical and ultrasound tomography. Although CMI does not recover estimates of material properties as these techniques do, it does identify areas of contrast in the tissue of interest. This information is likely sufficient for detection of tumors, and is arrived at in a very straightforward manner with CMI. Additionally, the resolution of CMI is determined primarily by the bandwidth of the illuminating signal, allowing for detection of small tumors with appropriate selection of the bandwidth. CMI is selected as a promising approach for this thesis investigation, as it appears to be a simple and effective technique for breast tumor detection. The development and evaluation of a new approach to confocal microwave imaging is the main contribution of this thesis.

Confocal microwave imaging was very recently introduced, and many key issues need to be addressed. Most importantly, the CMI system must be designed for physical compatibility with the breast examination. This involves design of a system configuration, suitable sensing elements and development of image reconstruction algorithms. Appropriate models and simulations of the system are required to test the feasibility of the proposed approaches. The finite difference time domain (FDTD) method is well suited to these feasibility studies, as ultra-wideband signals are efficiently simulated in the time domain. Additionally, the discretization of the problem space in FDTD allows for the incorporation of more complex and realistic breast models. Another aspect of the development of the CMI system is experimental verification. This is particularly important because the literature lacks proof that CMI will work for breast tumor detection in practice. This experimental work is a topic of future investigation, and will not be addressed in this thesis.

1.2 Research objectives and contributions

The main objective of this research is the development of a new approach to confocal microwave imaging for breast tumor detection. At the start of this research, a planar configuration for CMI had been recently introduced [41]. With this system, the woman undergoing examination lies on her back and the breasts are naturally flattened. The sensor, or an array of sensors, is placed directly on the skin of the breast. The initially proposed sensor consists of a bowtie antenna of 8 cm in length, or two crossed bowtie antennas [48]. Because the antenna array is assumed flat, this system is referred to as the planar CMI system. The objectives of this thesis research are to develop a system for confocal microwave imaging that:

- incorporates smaller antennas than the initially proposed bowties,
- has minimal contact with the woman to be scanned (i.e. is less intrusive),
- provides a frame of reference for image reconstruction by using antenna positions determined prior to the scan, and
- is capable of detecting sub-cm tumors at realistic depths in the breast.

In the system proposed in this thesis, a woman lies in a prone position with the breast extending through a hole in the examination table. The breast is encircled by an array of small antennas, which are 1.5 cm or less in length and located at a distance from the breast skin. To interrogate the breast in three dimensions (3D), the array is scanned to several vertical positions, thus forming a cylindrical or conical array. The proposed system is referred to as cylindrical CMI, and the main contribution of this thesis is the development of this system for detection and localization of sub-cm tumors in a three dimensional breast volume.

Contribution 1: Design and evaluation of alternative sensors for confocal microwave imaging.

An antenna that provides reasonable performance while being physically small is required. Performance is evaluated with measures appropriate for radiation of an ultra-wideband signal and this specific imaging application. Resistively loaded dipoles, a vee dipole and a bowtie antenna are compared, and the best candidate design is selected. Additionally, the feasibility of using sufficiently separated multiple antennas for data acquisition is demonstrated.

Contribution 2: Development of image reconstruction algorithms for a 3D scan of the breast with cylindrical CMI.

The final images presented in this thesis demonstrate the feasibility of tumor detection and localization in 3D. Achieving these results involves signal processing procedures that reduce clutter and enhance the tumor response. Techniques to reduce the dominant reflections from the skin are presented, and various methods of signal processing are compared to identify the most effective of the proposed methods for robust tumor detection. Additionally, the influences of the number of data samples and two different immersion media are investigated.

Contribution 3: Tumor detection in a realistic breast model with cylindrical CMI.

Initial feasibility testing uses cylindrical breast models with random variations of up to +/-10% in electrical properties, representing the natural variations expected in breast tissue. In later work, the cylindrical CMI system is tested on a breast model that incorporates a chest wall, more realistic shape and glands with contrasts in permittivity of more than 60% compared to fatty breast tissue. Results demonstrate the ability to detect sub-centimeter tumors at depths of several centimeters.

The results of the investigations reported in the thesis are highly promising and have been recognized as such, e.g. by well respected researchers in the field who state:

> "Following a similar approach [to Hagness et al], Fear and Stuchly have introduced a microwave-breast-imaging technique that is more suitable to clinical implementation. These results are encouraging and further support the notion that microwave breast imaging should be aggressively pursued in a variety of forms." [113].

General performance of the system developed in this thesis is similar to that of the planar CMI system, as recently reported [114]. However, the cylindrical CMI presented here is compatible with practical implementation as it incorporates spatial locations of the antennas determined before the scan, creating a reference system for image reconstruction. Lack of such a reference system remains the main drawback and limitation of the planar CMI system.

1.3 Outline

Chapter 2 presents an overview of breast imaging, including various approaches to microwave breast imaging. A review of the studies of dielectric properties of breast tissues and malignancies is provided to demonstrate that the contrast in electrical properties of normal and malignant tissues is a reasonable assumption. An introduction to confocal microwave imaging and a review of work with the planar system are given in Chapter 3. The cylindrical system is presented, and compared to the planar system.

Chapter 4 presents methods and results for antenna design and selection. First, the four candidate designs are described. Measures appropriate for ultra-wideband radiation and

the imaging application are applied to each design. The results for antenna 1 are presented in the chapter to illustrate use of the measures, and an appendix contains results for antennas 2 to 4. Results for all antennas are compared to select the most appropriate of the candidate designs.

Breast imaging methods and results are included in Chapter 5. The breast models used in this work are described, and simulation methods discussed. The signal processing methods used to reconstructed images are outlined, and measures of success presented. The influence of each procedure is evaluated, both with respect to the relative tumor enhancement and the quality of the images. Successful detection and localization of tumors in 3D are demonstrated. A summary of results is given in Chapter 5, however most details are included in an appendix. Finally, a summary of the work presented in this thesis and recommendations for future research are given in Chapter 6.

2 Breast imaging

Effective breast imaging is important for breast tumor detection. In this chapter, the structure of the breast and the clinical indicators of benign and malignant breast diseases are outlined in order to provide understanding of the issues in breast imaging. Mammography is the most commonly used breast imaging method, however many other medical imaging modalities have been proposed and evaluated for this application. A summary of the effectiveness of mammography and alternative breast imaging methods is provided. Microwave breast imaging has recently become of interest due to developments in this technology. The electrical properties of tissues are reviewed, with emphasis on studies examining breast tissues and malignancies. The large contrast between normal and malignant tissues in the breast indicates the potential for successful tumor detection with microwave breast imaging. Several different approaches to microwave breast imaging have been explored, and these methods are described.

2.1 Breast and tumor morphology

The breast is located on the chest wall muscle, and extends upwards towards the clavicle and laterally towards the armpit [2]. The upper outer section of the breast is the thickest, and most tumors occur in this area (Figure 2-1a) [2]. The breast consists of glandular, fat and connective tissue [3], [4]. Blood vessels, nerves and lymphatic drainage systems are also present. The breast is supported by Coopers ligaments, which attach to the chest wall muscle [2]. The gland itself consists of 15 to 20 lobes (Figure 2-1b), which are separated by connective tissue and fat. The lobes are separated into smaller units called lobules, which end in a cluster of sack-like secretory units (alveoli). The alveoli drain into the lobules and lobes through a system of ducts. The duct draining each lobe terminates on the nipple. The nipple consists of the openings of ducts, sweat glands and is highly enervated.

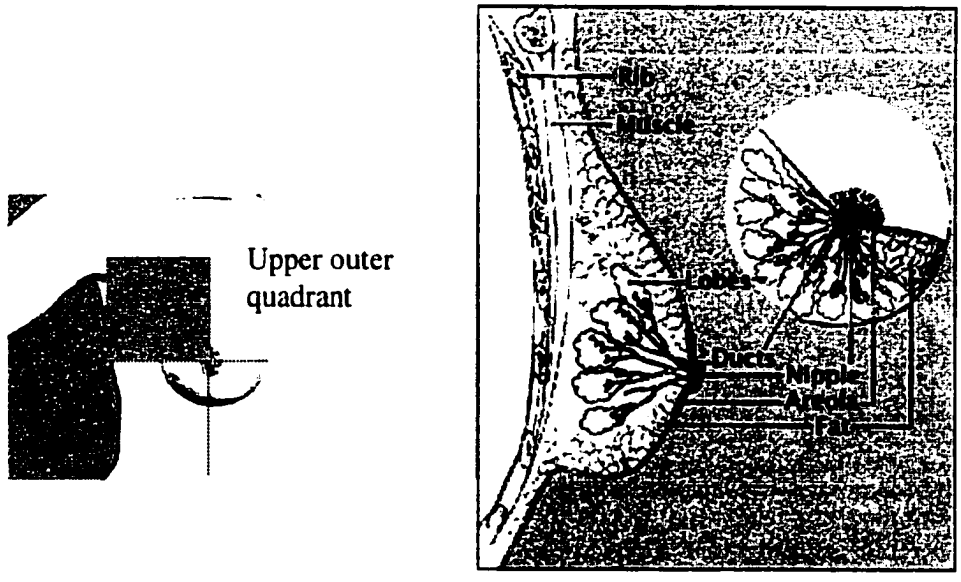

a) b)

Figure 2-1 a) Location of upper outer quadrant of the breast, and b) breast structure (from http://cancernet.nci.nih.gov/wyntk_pubs).

A woman may experience benign or malignant breast changes. Palpable lumps are common indicators of these changes, which makes identifying the disease or differentiating between benign and malignant changes challenging. Benign diseases include fibrocystic changes, which are common in younger women [2]. One possible result of these changes is the presence of cysts, which are spherical fluid-filled masses. Another type of benign disease is fibroadenoma, which results in fibrous solid lesions consisting of connective tissue and ducts [2]. These tumors tend to be symmetric and have well-defined edges. Malignant diseases, or breast cancers, are usually classified by location. Ductal cancers are most common (75%), while lobular cancers occur in about 15% of cases [5]. Malignant tumors may be identified by a spiculated appearance compared to smoother benign lesions, or by clustering of microcalcifications. If the malignancy invades the skin, then thickening or dimpling of the skin may be evident. Increased vascularization may occur around the tumor, as a greater blood supply is required to support the tumor growth. While changes such as cysts, fibroadenomas and malignancies may be identified by breast examination (palpation), it is difficult to differentiate between these lesions without additional information. Breast imaging is required to differentiate between normal and malignant tissues, and to detect changes in breast structure (e.g. skin thickening) and vascularization due to tumor growth.

2.2 Breast imaging techniques

Mammography, which involves x-ray imaging a compressed breast, is currently the "gold standard" breast imaging technique. With specialized mammography systems, tumors of greater than 3 mm diameter and microcalcifications of greater than 0.2 mm diameter can be detected [6]. Additionally, mammography detects 85-95% of lesions in the breast [6]. However, a recent study of Canadian breast screening programs suggests that mammography has a positive predictive value of 7.8% [8]. That is, if an abnormality is detected on a mammogram, then this corresponds to a malignancy in 7.8% of cases. After detection of an abnormality, additional mammography (58% of cases), ultrasound (26% of cases) or biopsy were required for diagnosis [8]. Biopsy is an invasive procedure, and less than half of the biopsies performed indicated malignancies. In British Columbia, the averaging waiting time between an abnormal mammogram and diagnosis was 3.4 weeks without biopsy, or 7.1 weeks with biopsy (in 1993) [9]. These studies demonstrate the need for e.g. complementary breast imaging techniques that provide specific information on the type of lesion, thus reducing waiting time and patient anxiety. A summary of alternative modalities tested for breast imaging is provided in Table 2-1. This table does not include passive tumor detection methods such as thermography, in which tumors are detected by difference in temperature compared to normal tissue [13]. Although thermography was not well received initially, advances in the technology and new approaches may result in future clinical applications [13]. Currently, ultrasound is frequently used clinically to differentiate cysts and solid lesions. Otherwise, the alternative techniques in Table 2-1 are not commonly used clinically, as some methods are experimental, and others are expensive or do not provide additional diagnostic information. Recently, microwave imaging has received interest due to advances in image reconstruction methods and new approaches. Microwave imaging is especially attractive because of the physical basis on which tumors are detected, namely the contrast in electrical properties of normal and malignant breast tissue. Electrical properties of breast tissue are examined in 2.3, and approaches to microwave breast imaging are outlined in 2.4.

Table 2-1 Alternative breast imaging modalities.

Method	Physical property	Specific application	Issues
Digital mammography [6,7]	Tissue density	Mammography with uncoupled image capture and display	• Development of effective image processing algorithms • Computer aided detection methods easily applied to images [10]
X-ray CT	Tissue density	Reconstruction of multiple slices	Increased radiation exposure
Breast angiography	Density of contrast medium in vessels	Increased vascularization of tumors	Radiation exposure and detection of small (non-vascularized) tumors
MRI [6]	Hydrogen distribution and binding in tissues	Tumors lack a characteristic signature, so uptake of a contrast enhancement agent is monitored	• breast coils and appropriate imaging sequence required • expensive method • proposed for staging of cancer and imaging women with implants
SPECT, PET	Differential uptake of tracer by tumor	^{99m}Tc-sestamibi for detection and staging [16, 17]	• radiation exposure • expensive method
Optical mammography [14]	Transmission and absorption of red or near-infrared light	Vascularization of tumor, as blood absorbs more light than breast tissue	Images of 17 volunteers have been created, and tumors of less than 1 cm in diameter detected.
Impedance imaging: • Mammoscan or T-scan [15]) • Electrical impedance tomography [18]	Electrical property distribution (i.e. tumor has higher conductivity and permittivity than normal breast tissue [21])	Contrast in electrical properties of normal and malignant tissues	• Approved by FDA, T-scan assists in biopsy decisions • Prototype multi-frequency electric impedance imaging system has been developed for breast imaging [20] • Images of 13 volunteers demonstrate detection of abnormalities matching clinical information.
Microwave + Ultrasound hybrid	Heat absorption	Differential heating of tumors	Prototype system developed for breast imaging (section 2.4.2)
Microwave imaging	Electrical property distributions	Contrast in normal and malignant tissue	Several approaches discussed in 2.4

2.3 Electrical properties of breast tissue

Biological tissues can be described as lossy dielectrics with complex relative permittivity [22]:

$$\varepsilon^* = \varepsilon' - j\varepsilon'' = \varepsilon_r - j\frac{\sigma}{\omega\varepsilon_o} \tag{2.1}$$

The permittivity of biological materials generally changes with frequency, and the Debye equation is often used to describe these changes [22]. It is essentially a simple description of first-order system relaxation plus a static conductivity (for ion movement):

$$\varepsilon^* = \varepsilon_\infty + \frac{\varepsilon_s - \varepsilon_\infty}{1 + j\omega\tau} - j\frac{\sigma_s}{\omega\varepsilon_o} \tag{2.2}$$

where τ is the relaxation time, ε_s is the static permittivity, ε_∞ is the permittivity at frequencies well above the relaxation frequency and σ_s is the static conductivity. In real tissues, there is often a broad distribution of relaxation times due to the presence of several different mechanisms, higher order processes, and interactions between particles in suspension [22]. A better fit to dielectric data, which accounts for a spread of relaxation times, is the Cole-Cole equation:

$$\varepsilon^* = \varepsilon_\infty + \frac{\varepsilon_s - \varepsilon_\infty}{1 + (jf/f_c)^{1-\alpha}} - j\frac{\sigma_s}{\omega\varepsilon_o} \tag{2.3}$$

where f_c is the relaxation frequency and is related to τ by:

$$\tau = \frac{1}{2\pi f_c} \tag{2.4}$$

Generally, tissues exhibit 3 distinct relaxations related to the underlying physical structure of tissues [22]. Below the first relaxation, tissues tend to have high permittivity. The alpha relaxation occurs at low frequencies (kHz), and is due to ionic diffusion in the layer of charged particles surrounding the cell. This creates an induced dipole moment and polarization, which results in a large decrease in permittivity. The beta relaxation occurs at RF, and is caused by the charging of interfaces between the insulating cell membranes, the cell interiors, and extracellular suspension. This relaxation results in a

large decrease in permittivity and an increase in conductivity due to increased conduction through cell membranes. The gamma relaxation is primarily due to dipolar relaxation of water in the tissues, and occurs near 20 to 25 GHz. The variation in permittivity with frequency for high and low water content tissues is shown in Figure 2-2.

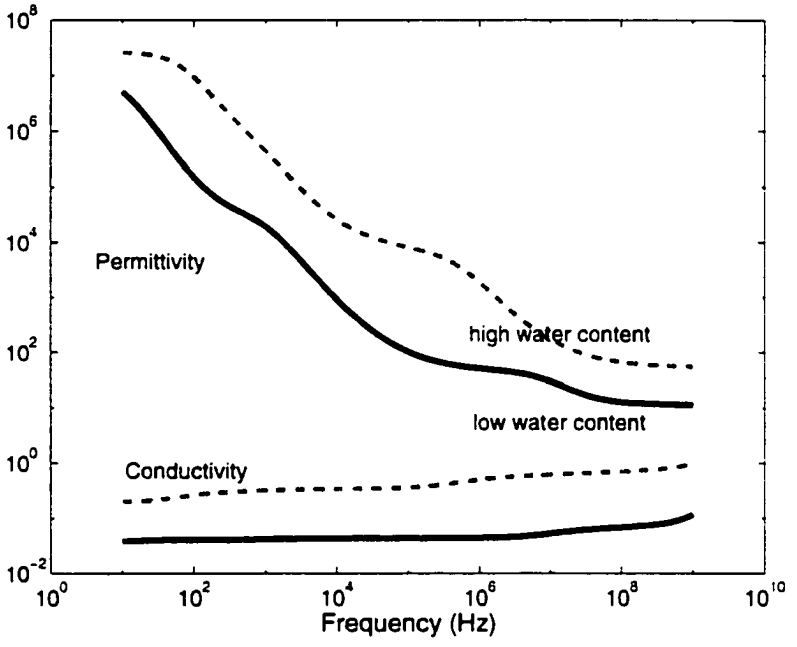

Figure 2-2 Dielectric relaxation of high and low water content tissues. The figure shows a Cole-Cole model fit to measured data from [24].

With breast imaging, the frequency must be high enough to obtain reasonable resolution and low enough for penetration into tissue. Therefore, the frequency range of interest is between the beta and gamma relaxations.

Extensive characterization of different tissue types in the frequency range 10 Hz to 20 GHz has been performed by Gabriel et al [23, 24]. At RF frequencies, factors to consider in measurements of tissues include changes in properties with temperature, and changes in water content with excision of tissue. Although many tissues have been well characterized, limited data are available for breast tissue. The differences between normal and benign tissues have been examined for various species and tumor locations.

2.3.1 Malignant Tissue

Tumors tend to have larger permittivity and conductivity than normal tissues. The significantly higher water content in tumors (due to cell changes and increased vascularization) is considered to be responsible for these increases in conductivity and permittivity at microwave frequencies [22]. The properties of malignant tissue have been studied traditionally for use in hyperthermia treatment of cancer. Pelso et al [26] measured rat mammary tumors from 1 MHz to 1 GHz, and found that tumors had properties similar to muscle, a higher water content tissue. Comparisons with normal mammary tissues were not made. Rogers et al [27] measured properties of mouse muscle and tumor (in thigh) tissues from 50 MHz to 10 GHz. Their results indicated greater relative permittivities in tumor tissues at the lower frequencies studied, with this difference increasing with decrease in frequency. Joines et al [28] measured human normal and malignant tissues from 50 to 900 MHz, finding greater conductivity and permittivity in malignant tissues when compared to normal tissues. These studies of malignant tissues indicate that a contrast between normal and malignant tissues persists over the frequency range.

2.3.2 Breast Tissue

The breast tissue is composed primarily of fat, glandular and connective tissues. Fat cells are filled with lipid, and thus have lower water content than other tissues. At microwave frequencies, this results in lower permittivity and conductivity, as these quantities increase with water content [22]. This also suggests the existence of a large contrast between high water content tumors and low water content normal breast tissue. Benign tumors consist primarily of fibrous tissue and ducts, and are likely therefore to have different properties from the high water content malignancies.

Measurements of normal and malignant breast tumors were made as early as 1926, indicating greater permittivity in malignant tissues at the measurement frequency of 20 kHz [29]. Early measurements of dielectric properties of breast tumors in the microwave

region (3 GHz to 24 GHz) showed greater attenuation in the tumors than in breast fat tissue [31], [32]. It was later suggested that the differences in reflected and transmitted power in the presence of a tumor (compared to the normal breast) could be used to identify breast cancer [33].

Electrical properties of breast tissues have been investigated at lower frequencies (below 10 MHz) for use in electrical impedance imaging. Of the studies in the literature, the most relevant results involve practical imaging systems [15, 21], as well as comprehensive measurements of excised tissue by Jossinett [37]. The T-scan has been approved by the FDA, and provides complementary information for ambiguous mammograms, indicating the need for biopsy [15, 16]. The patient holds an electrode, a low intensity current flows through the body and is detected by a probe (or electrode) that is scanned over the breast. The recorded data are used to create a map of impedance changes in the breast, and tumors are identified by increases in permittivity and conductivity (compared to normal breast tissue). An impedance imaging system incorporating more complex image reconstruction algorithms has also been developed [20,21]. Images of volunteers acquired with a multifrequency impedance imaging system from 10 to 950 kHz indicated differences in electrical properties of normal and malignant tissues [21]. Generally, images of normal breasts displayed a high degree of homogeneity. For identification of malignancies, permittivity images appeared to be more useful and showed larger values for malignant tissues in most cases. Jossinett has measured the impedance of excised normal tissue (mammary gland, connective tissue, adipose tissue) and pathological tissue (mastopathy, fibroadenoma and carcinoma) over the frequency range 488 Hz to 1 MHz [37]. The normal and benign tissues had similar properties, while the carcinoma tissue differed from all other types. While these results are obtained at lower frequencies, they demonstrate the existence of a contrast in the electrical properties of normal and malignant tissues, as well as potential use of imaging these properties for diagnosis.

Dielectric properties of tumors and normal breast tissues have been measured at radio frequencies [38]. Samples of excised human tissues were obtained from the center of the

tumors, the margins of the tumors and from normal breast tissue. In total, 28 samples from 7 excised specimens were examined. The samples were examined within 4 hours of excision, and cut from the excised tissue in the form of thin discs (diameter of 6 mm and thickness of 1 mm cut from larger tissue samples). An end-of-line coaxial sensor measured the input reflection coefficient at 101 frequencies from 100 kHz to 100 MHz. The sensor incorporated a water bath, so the tissue was maintained at 37°C. The measurements were repeated 10 to 15 times. Three different ranges of dielectric constants were identified from the measurements (Table 2-2). These ranges correspond to differences in tissue structures of normal breast tissue, tumors, and the tumor margins. A Cole-Cole fit to the data found broader distributions of relaxation times for the tumor and samples from the tumor margins when compared to normal tissue. This further reflected structural differences in the tissues. When examining the data for normal tissue samples more closely, a standard deviation of 125 was noted for the samples with permittivity less than 500. Each specimen containing normal and malignant tissues exhibited contrasts between these tissues. Overall, significant differences were found between normal and cancerous tissues, and these differences persisted over the measurement range.

Table 2-2 Measurement of breast tissues from [38]. The permittivity and conductivity ranges are determined at 100 kHz, while the conductivity increment is the difference in conductivity between 100 kHz and 100 MHz.

Tissue	ε_r	σ (S/m)	σ increment (S/m)
Bulk tumor	2000 to 6000	0.2 to 0.4	0.4 to 0.5
Tumor margins	2500 to 8000	0.4 to 0.7	0.5 to 0.7
Normal	< 500	0.1	< 0.05

Joines et al [28] measured properties of normal and malignant tissues between 50 and 900 MHz. Freshly excised tissues were measured with a flat-ended coaxial probe, and each sample was measured 3 times at different positions. Results indicated that breast tissue had the largest contrast between normal and malignant tissues of the tissue types investigated (colon, kidney, liver, lung, breast, and muscle). The permittivity was an average of 3.4 times higher, and the conductivity was an average of 6.8 times higher over the frequency range.

Another significant study was performed by Chaudhary et al [39] who measured normal breast tissues and carcinoma from 3 MHz to 3 GHz. Between 3 and 100 MHz, the sample was placed in a chamber at the center of a parallel plate capacitor. An impedance meter was used to obtain measurements, which were corrected for lead inductance. Measurements from 100 MHz to 3 GHz were performed with a time-domain method. Normal and malignant tissues from 15 patients were examined. The average of the set of measurements showed an increase in electrical properties of malignant tissues when compared to normal tissues. The increase in both permittivity and conductivity is a factor of at least 4 at 3 GHz.

Other measurements of dielectric properties of breast tissues have been made by Land et al [40]. Dielectric properties of breast tissues at 3.2 GHz were measured using a resonant cylindrical cavity with sample holders. Measurements did not indicate significant differences in normal and malignant tissues, which is not in agreement with the rest of the information in the literature. This is likely attributable to sample preparation techniques causing changes in properties due to cutting, fluid loss, etc. or air pockets may have been present in the samples.

A recent study of clinical microwave breast imaging [113] reported permittivities larger than measured in previous studies (e.g. [28]), and appeared to be related to radiographic breast density. The properties were obtained from reconstructed images, not direct measurements of the tissue. Estimates of the electrical properties of tumors or images of tumor bearing breasts were not provided. However, variations corresponding to e.g. breast reduction were evident in images, demonstrating that microwave imaging is a promising method of breast imaging.

The studies cited in this section generally suggest that a large contrast in electrical properties of normal and malignant breast tissues persists over a wide frequency range. For tissue measurements, Gabriel et al estimate measurement reproducibility at 1% and natural variations in dielectric properties due to tissue structures as 10-15% [23]. This certainly seems reasonable for breast tissue, as it contains fatty tissue and glands. Factors

such as age and radiographic breast density may provide insight into the likely range of permittivity values. However, at the time of this thesis research, detailed information on the dielectric properties of breast tissue was not available. In order to characterize the behavior of breast tissues over a frequency range of interest for confocal microwave imaging, extensive measurement programs are ongoing at the University of Wisconsin-Madison and the University of Calgary. The preliminary data suggest that contrasts between normal breast tissue and tumors, as well as benign and malignant lesions, exist [42]. For modeling the confocal microwave imaging system, Hagness et al [41] have extrapolated to higher frequencies the data of Joines et al [28] and Chaudhary et al [39], which describe normal breast tissue. The Debye model was selected to fit the data, and the following parameters were determined: ε_s=10, ε_∞=7, τ=6.37 ps and σ=0.15 S/m. These properties are also used for normal breast tissue in this work. It is emphasized that the frequency range for CMI is selected in order to provide reasonable resolution without excessive attenuation. This requires a wideband signal with frequency content not exceeding 10 GHz. It appears likely that a contrast between normal and malignant tissues exists over the frequency range of interest.

Electrical properties of interest for breast imaging include those of skin, as a layer of skin surrounds the breast. The electrical properties of both dry and wet skin have been measured over the frequency range 10 Hz to 100 GHz by Gabriel et al [23,24], and fit with a Cole-Cole model. For dry skin, the electrical properties may be described as:

$$\hat{\varepsilon}(\omega) = 4 + \sum_n \frac{\Delta\varepsilon_n}{1+(j\omega\tau_n)^{1-\alpha_n}} + \frac{0.0002}{j\omega\varepsilon_o} \tag{2.5}$$

where $\Delta\varepsilon_1$=32, τ_1=7.23, α_1=0, ε_2=1100, τ_2=32.48, and α_2=0.2.

2.4 Microwave breast imaging

Breast tumor detection with microwave imaging is based on the contrast in electrical properties between normal and malignant breast tissues. Although breast tissue has not been well characterized over a wide frequency range, the few studies that have been completed and reviewed in 2.3 suggest that this contrast is relatively large. This contrast provides a specific, physical basis for microwave approaches to breast tumor detection.

Many previously investigated alternative approaches to breast imaging rely upon factors related to the tumor, such as increases in temperature. This suggests that microwave imaging may meet with greater success due to the stronger physical basis for tumor detection. Additionally, there is potential for distinguishing between benign and malignant tumors if benign lesions have characteristic electrical properties or share those of normal breast tissue.

Microwave imaging of the human body has been of interest for years, and an overview of this work is provided in Appendix A. A summary of prototype systems based on classical approaches to microwave imaging is provided in Table 2-3. The system developed at Dartmouth is undergoing clinical trials for breast tumor detection, and is further described in 2.4.1. An adaptation of another microwave imaging system for breast screening has also been proposed [79]. For breast tumor detection, a number of approaches in addition to classical microwave imaging are of interest, including hybrid methods combining ultrasound and microwaves, as well as confocal microwave imaging. Brief overviews of these techniques are provided in sections 2.4.2 and 2.4.3.

Table 2-3 Microwave Imaging Systems.

	Reference	Dartmouth	Bolomey (France)	Barcelona	Carolinas
System Characteristics	Number of transmitters	16	36	64	32
	Number of receivers	9	25	33	16
	Frequency	900 MHz	2.45 GHz	2.33 GHz	2.36 GHz
	Dynamic range	135 dB	-	-	120 dB
	Imaging region	Cylindrical: 13 cm diameter	Planar: object 6.5 cm from receivers	Cylindrical: 25 cm diameter	Cylindrical: receivers 9.5 cm and transmitter 17.3 cm from center
Models experimentally imaged	External dimensions	• 8.2 cm diameter cylinder • clinical studies	6 cm diameter cylinder	4 cm diameter cylinder	5.5 by 5.5 by 6.5 cm ellipsoid with 2 semi-spherical holes
	Electrical properties	• Excised fat with 1.2% saline inclusions (1.1 and 2.5 cm diameter) • Bone/fat phantom (εr=5.48, σ=0.02 S/m)	• Saline with contrasts of 0.8% in εr and 40% in $\varepsilon r''$ • Saline with contrasts of 3% in $\varepsilon r'$ and 150% in $\varepsilon r''$	4% ethyl alcohol (εr=73, σ=11) with 96% alcohol inclusion (εr=10, σ=8.3 S/m)	• Ellipsoid: εr=70, σ=17 S/m • Holes (water): εr=77, σ=9.7 S/m
	Immersion medium	0.9% saline (εr=76.6, σ=2.48 S/m)	Water at 37C	Water at 25C (εr=73, σ=11 S/m)	Water

2.4.1 Classical microwave imaging

A prototype system for microwave breast imaging was introduced by Paulsen et al [44,45]. Images of the real and imaginary components of the wave number variation in the object of interest are created. For breast imaging, the woman lies prone with the

breast extending through a hole in the examining table, and immersed in a saline solution. The breast was surrounded by an array of 16 monopole antennas. The tissue was illuminated at a frequency between 300 and 900 MHz by each antenna in turn, and measurements were recorded at 9 antennas positioned opposite. To reconstruct the image, the Newton-Raphson iterative method was applied. An initial guess of the material properties was used to compute the scattered fields at the antenna positions with the hybrid finite-element boundary-element method. A model of non-active antenna elements was incorporated. The differences between measured and computed fields were related to the material property update by the Jacobian matrix, which was computed using results from the forward problem (please see Appendix A for details). This process was repeated with updated material properties until convergence.

This imaging technique has been used to examine excised breast tissue placed in an 8.2 cm diameter thin-walled cylindrical container, and immersed in a 0.9% saline solution. Inclusions of 1.1 and 2.5 cm diameter tubes filled with 1.2% saline were used to represent tumors. Images indicated the presence of the tubes, with better visibility in the image of the real component. The need for greater resolution suggests that increasing the illumination frequency may be required. Initial clinical trials are on going, and images of 5 volunteers were presented in [113]. All volunteers had recent clear mammograms, however some had previously undergone lumpectomy or breast reduction. Images were reconstructed at 900 MHz for several 2D slices of the breast at positions ranging from the nipple to chest wall. As mentioned in Section 2.3.2, electrical properties recorded from images were larger than previous measurements indicated, however variations due to e.g. breast reduction were evident on images. This imaging method has great promise for tumor detection, especially with the proposed increase in frequency to 3 GHz to provide increased resolution and the ability to detect smaller tumors.

2.4.2 Microwave-ultrasound hybrid techniques

Hybrid methods involve heating the tissue with microwaves, and detecting the pressure (sound) waves generated by the mechanical expansion of the tissue. The basis of tumor detection is differential heating of the tumor compared to normal breast tissue. Two

approaches are explored in the literature: thermoacoustic computed CT (TACT) and scanning TACT.

In TACT, signals recorded at ultrasound transducers are used to reconstruct images with a filtered back-projection algorithm, similar to those used in x-ray CT. In the proposed system for breast imaging [46], 64 transducers with peak frequency of 1 MHz were arranged in a spiral pattern in a hemispherical stainless steel bowl. A helical antenna was located at the bottom of the bowl, and transmitted 0.5 μs pulses of 434 MHz energy. The temporal width of the pulse determines the bandwidth of the acoustic waves, so a pulse of less than 1 μs was required to produce acoustic waves in the medical region. The resolution was determined by the ultrasound propagation in tissue, array geometry and reconstruction algorithms, and estimated at 1 to 5 mm. This system has been used to image women, and tumors of 1 to 2 cm diameters have been detected.

With scanning TACT, the image reconstruction algorithms are much simpler due to use of a focused ultrasound transducer [111,112,]. The time response recorded at the transducer was shown to represent the variations in the material along the transducer axis. By scanning the transducer along the sample and recording traces at each position, cross-sectional images of samples were formed. A short microwave pulse and wideband ultrasound transducer achieved axial resolution, while the lateral resolution was related to the transducer aperture and sample-transducer distance. Images of phantoms have been successfully obtained.

2.4.3 Confocal Microwave Imaging

The pulsed confocal microwave system for breast cancer detection was recently proposed by Hagness et al [41], [48]. In CMI, the breast is illuminated with an ultra-wideband pulse and returns are recorded at the same antenna. This is repeated for a number of different antenna positions. The resulting array of antennas is then synthetically focussed by computing time delays from each array element to the identified focal point, and adding the corresponding portions of each recorded signal. The focus is synthetically scanned through the breast, and computed returns at each focal point form the image.

This approach results in the coherent addition of returns from objects such as tumors, while clutter is suppressed.

Confocal microwave imaging has several advantages, but suffers from similar disadvantages as previously proposed methods. The image reconstruction algorithm is simple, and does not require great computational power or complex algorithms. These more complex algorithms are used in other approaches to microwave imaging, as well as ultrasound and optical tomography. The algorithms generally involve matching measured data with data computed using a model (forward problem). As the inverse scattering problem is inherently ill conditioned, errors in the measured data may be amplified. This is not an issue for CMI due to the simple reconstruction algorithms. With CMI, resolution is determined primarily by signal bandwidth and is not limited to about $\lambda/10$ as in classical microwave imaging techniques. The tumors used in initial system evaluations are therefore a few millimeters in diameter, while other systems examine tumors that are at least 1 cm in diameter. Confocal microwave imaging requires a large dynamic range in order to record returns from small tumors. However, this difficulty in performing measurements is common to all microwave imaging systems. A disadvantage of the images created with confocal microwave imaging is estimates of material properties are not directly provided, rather areas of increased returns are indicated.

2.5 Concluding Remarks

In this chapter, the limitations of current methods of breast imaging were discussed, and the potential for microwave breast imaging was introduced. Breast structure and disease were reviewed to provide insight into the difficulties in diagnosing these diseases. Mammography is commonly used to image the breast, however has limitations such as difficulty in discriminating benign and malignant tumors. Various medical imaging technologies have been applied to breast imaging, but have not succeeded in providing specific information on tumor type. One promising approach is microwave imaging, as the large contrast in electrical properties has provided motivation to explore this method of breast tumor detection. Several approaches to microwave breast imaging and

prototype systems were described. The next chapter provides a more comprehensive review of confocal microwave imaging, and introduces the cylindrical system of interest in this thesis.

3 Confocal Microwave Imaging

This chapter presents the basic principles of confocal microwave imaging, outlines research accomplished with the planar system, and introduces the cylindrical system. Confocal microwave imaging for breast cancer detection is similar to ground penetrating radar for mine detection. The basic principles of CMI and its suitability for breast tumor detection are discussed in this chapter, and more details on relevant work in ground penetrating radar are provided in an appendix. Research with the planar system has established the feasibility of CMI for breast tumor detection, and a summary of this work is provided. The cylindrical system configuration is introduced, and advantages and disadvantages compared to the planar system are discussed.

3.1 Basics of CMI for breast tumor detection

Confocal microwave imaging for breast tumor detection was recently introduced by Hagness et al [41,48]. This technology adapted ideas from an FM chirp radar operating at 94 GHz and used to detect concealed weapons [41]. This approach to breast tumor detection is analogous to the detection of unexploded plastic mines, as the objective is finding an object in a heterogeneous background. Therefore, many ideas and approaches from ultra-wideband ground penetrating radar for subsurface sensing are useful, and further explored in Appendix B.

The tumor detection with CMI is based on the coherent addition of returns from strongly scattering objects (i.e. tumors) and incoherent addition of clutter from e.g. the natural variations in electrical properties in the breast. The breast is well suited to CMI because of the large contrast between normal and malignant breast tissues, as well as the penetration of microwaves into normal breast tissue. Specifically, an attenuation of less than 4 dB/cm is expected for frequencies up to 10 GHz, so detection of tumors at depths of up to 5 cm is feasible.

The first step in CMI involves illuminating the breast with an ultra-wideband pulse. For this application, an ultra-wideband signal is specified due to the requirements of wide

bandwidth (for depth resolution) and minimum attenuation. That is, a pulse width of 0.2 ns is required for resolution of 1 cm, however the upper frequency in the signal of interest is limited to about 10 GHz. This results in an ultra-wideband signal. An appropriate antenna is required to radiate and receive the selected ultra-wideband signal. Antennas proposed for radiating ultra-wideband signals are discussed further in Appendix B. Once the signal and antenna are selected, the breast is illuminated and the scattered signal is recorded at the transmitting antenna. This is repeated for a number of antenna positions. As lateral resolution depends on the size of the synthetic aperture, a sufficient span and number of antenna locations is required to obtain the desired resolution.

After data acquisition, an image is formed by synthetically scanning the focus of an array of antennas through the breast [41]. A time-shift-and-add algorithm is applied to the set of recorded signals. This involves computing the time delay for the round-trip between each antenna to a point in the domain of interest, then adding the corresponding portions of the time signals recorded at each antenna. When the focus is located in normal breast tissue, returns add incoherently, thus reducing clutter. Returns add coherently when the focus is positioned on the tumor and the resulting signal, which is significantly larger than the clutter, indicates the presence of a tumor. To further enhance the tumor response and suppress clutter, additional signal processing techniques adapted from ground penetrating radar may be applied (Appendix B). Even with these additional techniques, the images obtained with CMI do not involve complex reconstruction algorithms. However, there is a trade-off between simplicity and information obtained, as material properties are not recovered as in classical microwave imaging.

3.2 Planar system feasibility studies

When this thesis research began, several feasibility studies of CMI for tumor detection had been completed with the planar system configuration. The feasibility of detecting small 2D tumors at reasonable depths was demonstrated. A bowtie antenna for biological sensing was developed, and used to interrogate 3D tumors. Recently, the planar system has been used to demonstrate detection of 2D tumors in a more realistic breast model. A modified antenna and simple breast model have also been used to investigate the

localization of a tumor response in 3D. All of these studies have used the finite difference time domain (FDTD) method to simulate data.

Initial 2D simulations with the planar system showed feasibility of detecting tumors in a heterogeneous background [41]. The first sensing element consisted of a monopole antenna placed at the focus of an elliptical reflector and positioned over a half-space of heterogeneous breast tissue. The antenna was excited with a 270 ps Gaussian pulse (full-width half-maximum frequency content from 4 to 8 GHz, which was in the optimum frequency window [84]). Tumors of at least 2 mm diameter and located at the focus (depth of 3.8 cm) were successfully detected with signal-to-clutter (S/C) ratios on the order of 10 dB. The elliptical reflector was then replaced with a 17-element array of monopole antennas which were spaced 0.5 cm apart and positioned on a skin layer (Figure 3-1) [41]. The array configuration allowed for electronic scanning of elements to provide faster data acquisition. A calibration procedure, which subtracted returns recorded with a homogeneous breast model, was introduced. With the array, the S/C ratio was similar to that observed with the elliptical reflector. This configuration was also found robust to:

- varying skin conductivity from 0.5 to 5 S/m;
- a gland (electrical properties 15% greater than normal breast tissue) positioned around the tumor;
- the presence of a 2 mm diameter vein between the tumor and antenna array; and
- breast tissue permittivity dispersion.

These initial feasibility studies indicated the potential for microwave confocal imaging to detect small tumors. A similar approach was later used with a more realistic breast model based on magnetic resonance breast images [115]. In this case, the +/-10% variations in material properties were mapped to the range of pixel values in the breast tissue. An array of monopoles was used to detect a 2D tumor embedded in the breast model. Results demonstrated successful detection with more realistic breast shape and material property variations.

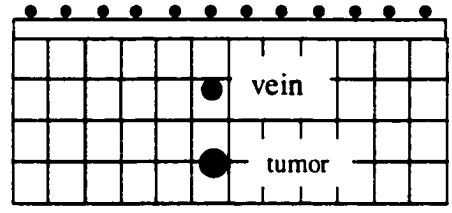

Figure 3-1 Array of monopole antennas placed on a 1 mm thick skin layer (ε_r=36, σ=4 S/m).

Hagness et al developed a very sensitive resistively loaded bowtie antenna [48] (Figure 3-2), and evaluated its tumor detection performance with 3D simulations [85]. The bowtie was initially designed in a lossy dielectric similar to breast tissue, and had a resistive profile of:

$$R(z) = R_o \frac{1+(R_{1/2}/R_o - 2)(z/h)}{1 - z/h} \tag{3.1}$$

where R_o depended on the type of metal at the feed point and $R_{1/2}$ was chosen to provide the specified attenuation of end reflections. When excited by a bandpass Gaussian function (FWHM spectral width of 4 GHz centered on 6 GHz and temporal width of 0.22 ns), end reflections were 106 dB below the excitation pulse [85]. The reflections were reduced to −125 dB when the bowtie was placed on a skin layer [48]. This antenna allowed for detection of spherical tumors on the order of 2 mm diameter at 5 cm depth, as the returns from these tumors were −110 dB below the excitation pulse. Two antennas placed in a Maltese cross configuration (Figure 3-2) permitted recording of cross-polarized returns [48]. This allowed for detection of tumors close to the chest wall. Spectral signatures related to tumor shape were also examined, and spherical tumors found to exhibit deep nulls in their spectra. These studies of the performance of the bowtie provided encouraging results, as small tumors with more realistic shapes were detected.

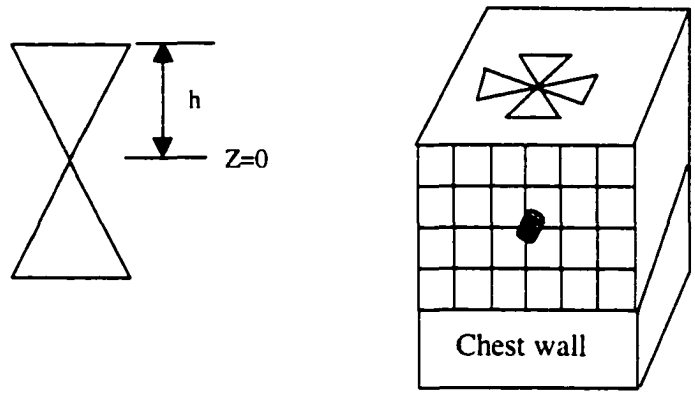

a) bowtie antenna

b) two bowties placed on skin overlaying heterogeneous breast tissue and chest wall

Figure 3-2 Bowtie antenna and Maltese cross configuration.

For the planar system to be used clinically, a woman lies in a supine position and the antenna array is positioned on the breast. The bowtie antennas described above were 8 cm in length, so reduction in size was required before practical application. Recent work with the planar system involved a bowtie of length 2 cm, and demonstrated successful localization in 3D of the tumor response [114].

3.3 Cylindrical system for CMI

Different CMI system configurations may be more practical or offer various advantages. The system investigated in this thesis has a different physical configuration, as the woman lies prone with the breasts extending through a hole in the examination table and surrounded by an array of antennas. The array of antennas is scanned to different heights, resulting in a cylindrical or conical array. Both the breast and the antennas are immersed in a low-loss material in order to improve impedance matching. The planar and cylindrical system configurations are compared in Figure 3-3 and Figure 3-4.

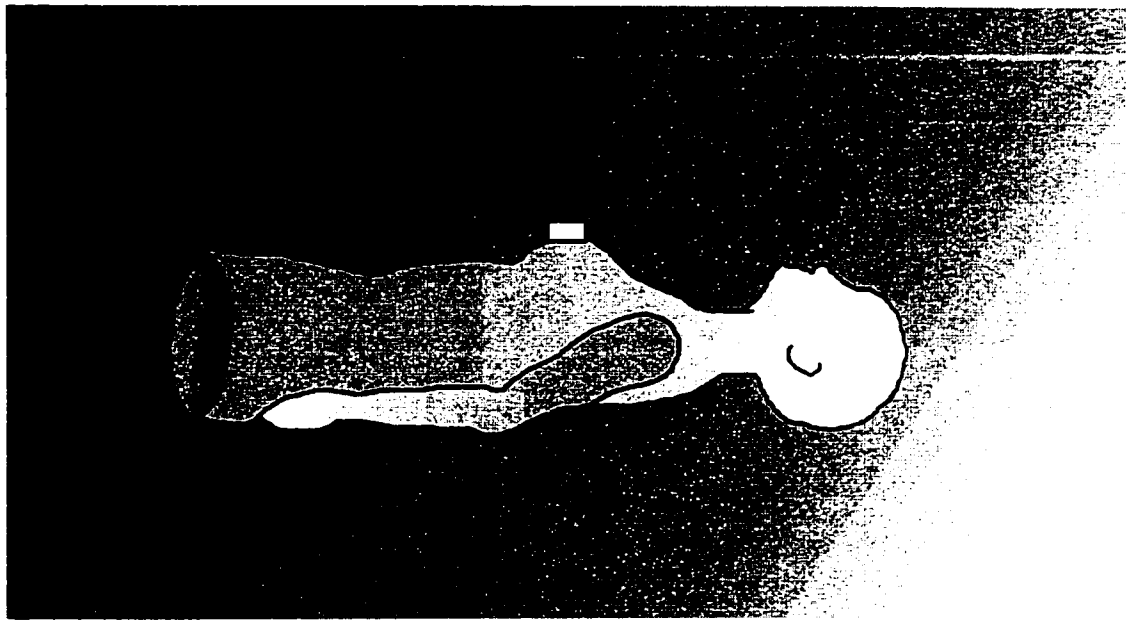

Figure 3-3 Planar CMI system configuration. The rectangle corresponds to a bowtie antenna embedded in a block of lossy dielectric.

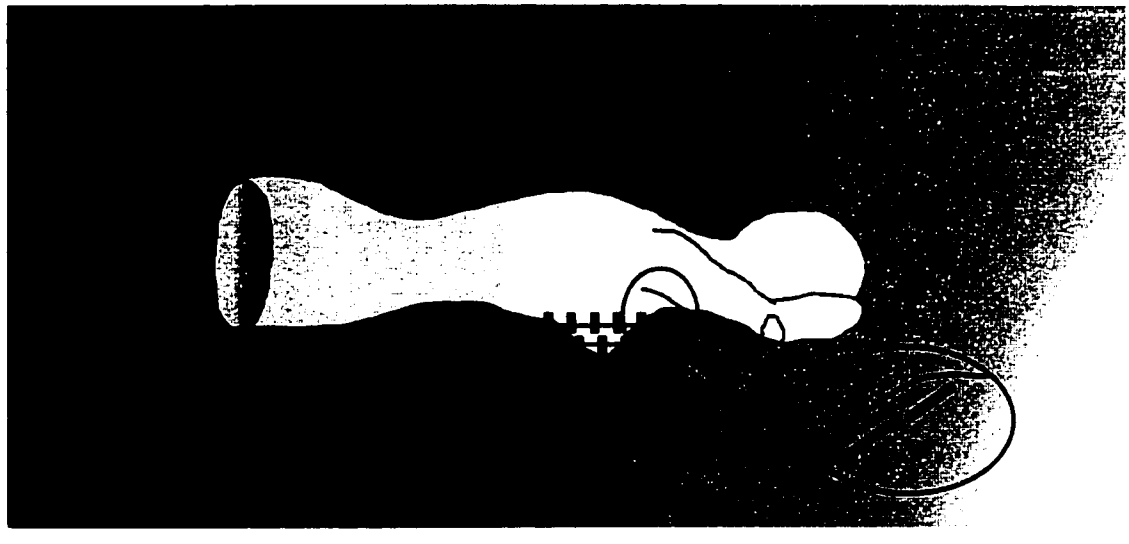

Figure 3-4 Cylindrical or conical CMI system configuration. Two rows of antennas are shown in a conical configuration. The antennas may require special positioning for imaging the upper outer quadrant of the breast, as illustrated.

One objective of the cylindrical configuration design is minimal contact with the patient. The antennas in Figure 3-4 encircle the breast, but are located at a distance from the skin. This meets the design goal of minimizing contact with the patient, and also allows for the locations of the antennas to be determined before the scan. However, the reflections from

the skin layer are present in the recorded signal. This provides information about the skin, and also poses new challenges in algorithm development, as returns from the skin dominate the returns from the tumor and must be reduced to allow for tumor detection.

A second design objective is the use of antennas smaller than the initially proposed 8 cm long bowties. The antennas proposed for use with the cylindrical system are less than 1.5 cm in length, thus providing the advantage of improved physical compatibility with the breast. However, the loss of sensitivity that results from use of the smaller antennas needs to be accounted for with signal processing in order to detect small tumors.

The main advantage of the cylindrical (or conical) system is the ability to determine the antenna locations before the scan, which provides a frame of reference for image reconstruction. With the planar system, the antenna must either be flexible to match the contours of the flattened breast, or a material is required to fill the gap between the antenna and skin. If a single flexible antenna is used, then the physical location of each interrogation location must be recorded. If a flat antenna with matching material is used, then the reflections from the skin and/or changes in the behaviour of the antenna must be considered.

The main disadvantage of the cylindrical system is the difficulty in imaging the upper outer quadrant of the breast. With the planar system, the upper outer quadrant of the breast is easily imaged by directly scanning this area. With the cylindrical system, modifications to antenna positioning are required, as illustrated in Figure 3-4. The skin reflection resulting from placing the antennas at a distance from the skin is not considered to be a disadvantage. First, this reflection can be reduced with signal processing techniques. Second, a reflection from the skin layer is also recorded with the planar system, however it is not separated (in time) from the incident pulse. This skin reflection is removed with a calibration signal that is obtained with a simulation of the antenna on a homogeneous breast model.

As CMI is a recently introduced technique, it is important and interesting to test this method with multiple system configurations. This stimulates the development of new image reconstruction algorithms, and provides additional evidence for the robustness of this approach for tumor detection.

3.4 Concluding Remarks

The ideas behind CMI have been outlined, and research performed with the planar CMI system has been reviewed. It appears that CMI is a feasible and robust approach to breast tumor detection, and is attractive due to the simplicity of the image reconstruction methods. The cylindrical CMI configuration was introduced, and was shown to meet the design objectives of minimal contact with the patient, knowledge of the antenna locations prior to the scan, and incorporation of small antennas. The next chapter covers design and selection of an appropriate antenna for use with cylindrical CMI, and the following chapter develops and demonstrates image reconstruction algorithms.

4 Antennas

Confocal microwave breast imaging involves illuminating the breast with an ultra-wideband signal, recording returns and processing these returns to form an image. For illumination of the breast with an ultra-wideband signal and receiving returns, an appropriate antenna is required. In this chapter, methods used to design, simulate and characterize four candidate antenna designs are outlined. Criteria used to determine the most appropriate antenna design are defined, and applied to results presented for each design. Once the most appropriate design is selected, the feasibility of placing multiple antennas in an array is investigated.

4.1 Methods

4.1.1 Antenna design

In Appendix B, several antennas appropriate for ultra-wideband applications are discussed, including resistively loaded dipoles, vee dipoles and bowties. Four candidate antenna designs are proposed for cylindrical CMI:

- Antenna 1 is a simple resistively loaded dipole designed in low-loss breast tissue. The resistive profile is based on the Wu-King design [103]. As outlined in Appendix C, the impedance along the length of the antenna is varied to give an outward travelling wave.
- Antenna 2 is also a resistively loaded dipole, however it is designed in low-loss skin.
- Antenna 3 is a vee dipole with the same resistive loading as antenna 1 and designed in low-loss breast tissue.
- Antenna 4 is a bowtie with the same resistive loading as antenna 1 (the loading varies along the bowtie axis) and designed in low-loss breast tissue.

Although resistively loaded antennas have poor efficiency and directivity, they are physically small and have reasonably wideband behaviour. The dipoles have low computational cost. Vee dipoles provide increased directivity, while the flare of the bowtie is better suited to wideband signals than a cylinder of constant diameter. It should be emphasized that antennas 3 and 4 are simply modifications of antenna 1, and not the

optimal vee dipole or bowtie for this application. For example, maximizing gain achieved with the vee dipole involves increasing the arm length and selecting the appropriate interior angle [92]. The point of this comparison is to determine whether the general characteristics of vee dipoles and bowties are suited for the CMI system configuration proposed in this thesis. Insight into these general characteristics can be obtained by comparing the performances of antennas 3 and 4 to that of antenna 1.

The dimensions of the candidate designs are shown Figure 4-1 to Figure 4-4. The length of one arm of each candidate design is $\lambda/4$. The resistive loading profiles for antennas 1 and 2 are shown in Figure 4-2. For computer simulations that are used to characterize the antenna behaviour, all antennas are placed over ground planes and modeled as monopoles. Each antenna is fed by a coaxial line with 50 Ω impedance through a hole in the ground plane that is located on the x-y plane. The computer models of antennas 1, 2 and 3 consist of rods made up of short sections. The properties of each section are determined by averaging the Wu-King resistive profile over the section. The discretized profiles resulting for antennas 1 and 2 are also shown in Figure 4-2. A similar approach is taken to modeling antenna 4, however the sections are thin rectangular prisms. These approaches to modeling antennas 3 and 4 result in stair-cased approximation to the actual geometry. The stair-cased representations of antennas 3 and 4 are also shown in Figure 4-3 and Figure 4-4.

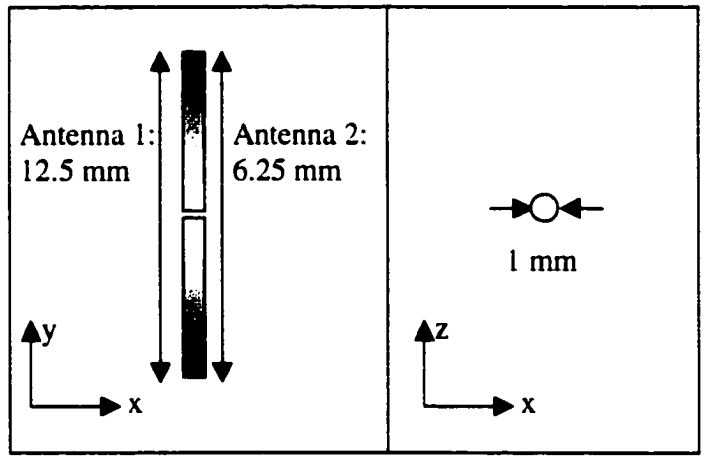

Figure 4-1 Dimensions of antennas 1 and 2.

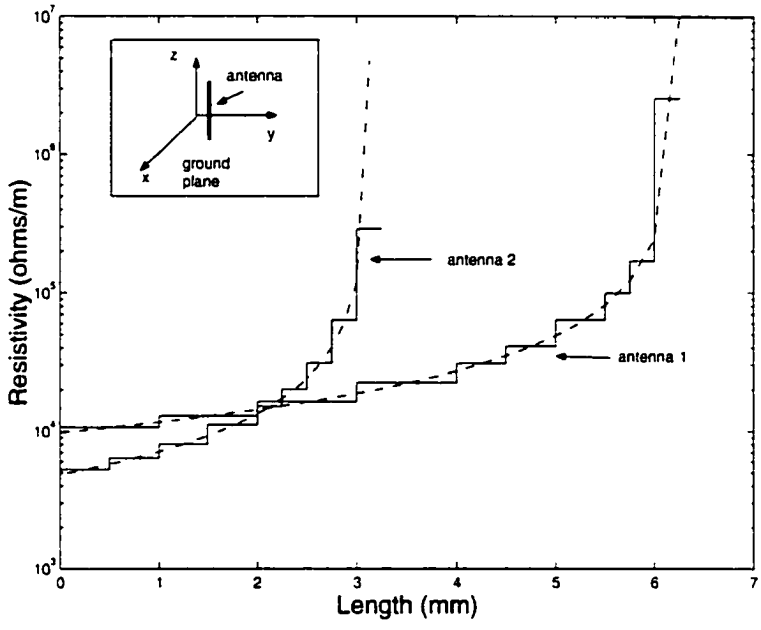

Figure 4-2 Resistive loading profiles of antennas 1 and 2.

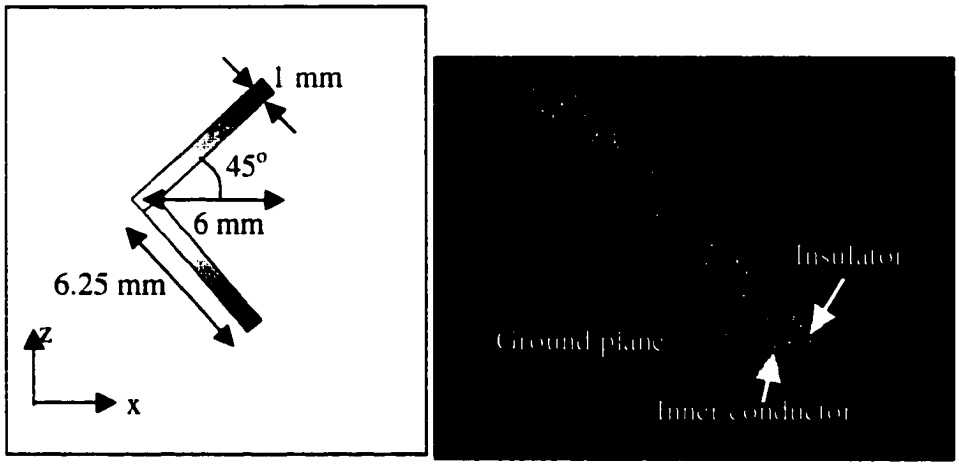

Figure 4-3 a) Dimensions of resistively loaded vee dipole antenna b) stair-cased computer model, showing ground plane with coax feed.

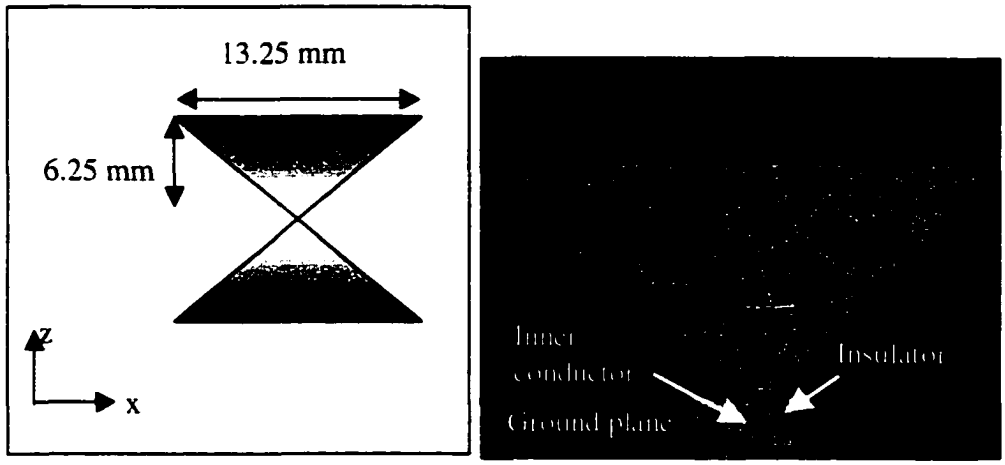

Figure 4-4 a) Dimensions of bowtie antenna b) stair-cased computer model.

4.1.2 FDTD Modeling

The FDTD method is used to simulate the behaviour of the antennas, and the LC computer code is used to characterize all candidate designs [107]. All FDTD simulations are performed in 3D, and problem spaces are terminated with perfectly matched layers (PML) [106]. Antennas are excited with an ultra-wideband differentiated Gaussian pulse. This pulse has content greater than 10% of the peak magnitude between 0.2 and 9.2 GHz in frequency, and over a 0.26 ns window in time. A grid size of 0.25 mm is used to discretize the problem space, and PMLs (4 or more layers, parabolic profile, 50 dB attenuation) are placed at least 2.25 cm from the antenna. A comparison between simulations with 4 and 6 layers showed reflections on the order of 2% of the maximum field value, and an average of 2% difference over the frequency range from 2 to 8 GHz. For initial antenna characterization, these increased reflections are tolerable in light of decreased computational cost. For 4 layers of PMLs and 4000 time steps, the CPU time for a simulation is approximately 3.4 hours on a 4 processor SGI Origin.

4.1.3 Antenna characterization

The antennas cannot be characterized with traditional frequency domain methods due to the wide bandwidth of the excitation signals. Many of classical measures involve fields

recorded in the far field of the antenna, however the far field distance varies with frequency. To define the far field in a way that is more appropriate for ultra-wideband (UWB) antennas, let's consider the antenna to be made up of small elements that each radiate a short pulse at the same instant in time [88]. Near the antenna, pulses arrive at a given point at different times, so the pulse shape varies with distance. As distance increases to the far field, pulses arrive at approximately the same time and the pulse shape is constant. One way of quantifying this is the transition of peak power variation from $1/R$ to $1/R^2$ [88]. This definition is tested for antenna 2, and the variation of maximum power density with distance is shown in Figure 4-5. The power appears to vary with $1/R^2$ even very close to the antenna. Alternatively one can consider that the pulse width of 0.26 ns is equivalent to a distance in low-loss breast tissue of 1.3 cm. If a breast model is placed 2 cm from the antenna, then the antenna does not "see" the breast until after the pulse is radiated. With this distance, limited coupling between the antenna and breast model is expected. Therefore, fields at distances of 1 and 2 cm from the feeds of antennas 1, 3 and 4 are investigated. These results are expected to scale (with wavelength) for immersion medium 2, so fields at 0.5 and 1 cm from antenna 2 are considered. While this is not a standard approach, it is extremely useful for comparison of antenna designs with respect to the CMI breast imaging application.

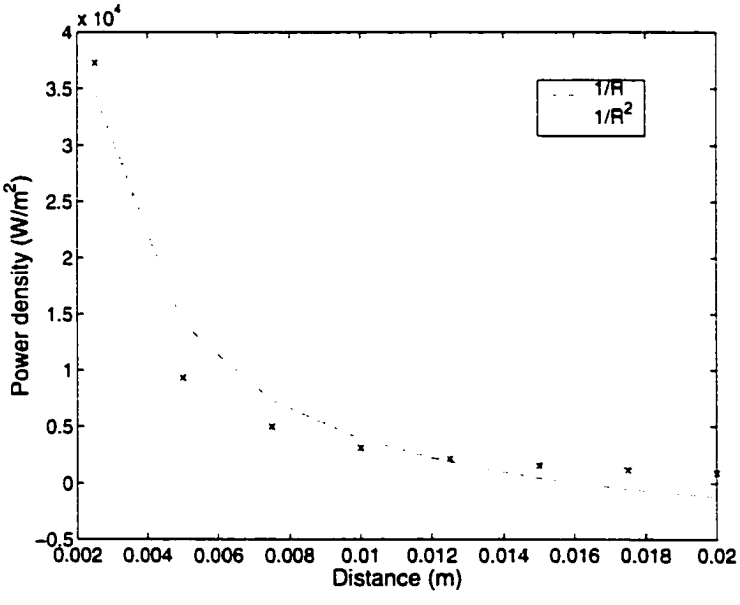

Figure 4-5 Maximum power density (ExH) computed 1.5 mm above the ground plane and at various distances from feed of antenna 2. The lines show data fits to $1/R$ and $1/R^2$.

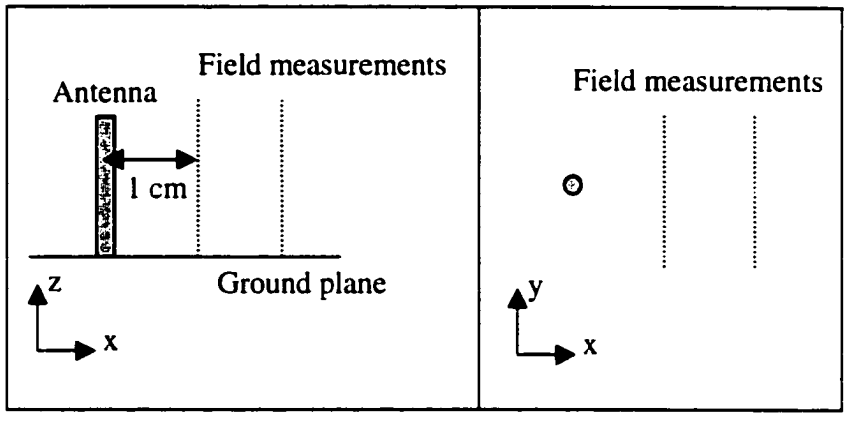

Figure 4-6 Field measurement points for monopole antenna a) parallel to antenna and b) perpendicular to antenna.

The performance measures for time domain characterization of the antennas used in this work include reflected voltage in the feed transmission line, transfer functions, fidelity, and time domain gain [88-91]. The measures of antenna performance change with the input signal, as this is inherent in the definition of quantities such as transfer function and fidelity.

1. The reflected voltage in the feed transmission line is computed by subtracting voltages measured in the feed coax, with and without the antenna present. The reflected voltages are also used to calculate the reflection coefficient (S11) and its variation with frequency.

2. To gain insight into the antenna pattern, the maximum electric field for each of the r, θ and ϕ components is examined. This is performed parallel and perpendicular to the z-axis (Figure 4-6).

3. In addition to the pattern, the time signature of the electric field is of interest. The similarity between two signals is measured with fidelity:

$$F = \max_{\tau} \left| \int_{-\infty}^{\infty} S(t)E(t+\tau)dt \right| \tag{4.1}$$

where S(t) is the normalized signal of interest and E is the normalized far-zone radiated electric field. In this case, fidelity is calculated with respect to the antenna excitation and the derivative of the antenna excitation. The maximum value is one.

4. Two definitions of time-domain gain are found in the literature [109,91]:

$$G(\theta,\gamma) = \frac{4\pi r^2}{\eta} \frac{\int_{-\infty}^{\infty} |E_{trans}(r,\theta,\gamma,t)|^2 dt}{\int_{-\infty}^{\infty} V_{in}(t) I_{in}(t) dt} \tag{4.2}$$

and

$$G(\theta,\gamma) = \frac{4\pi Z_c r^2}{\eta} \frac{\int_{-\infty}^{\infty} |E_{trans}(r,\theta,\gamma,t)|^2 dt}{\int_{-\infty}^{\infty} (|V_{in}(t)|^2 - |V_{ref}(t)|^2) dt} \tag{4.3}$$

where Z_c is the impedance of the coaxial feed line, η is the impedance of the immersion medium, E_{trans} is the transmitted field, V_{in} and I_{in} are the input voltage and current at the antenna terminals and V_{ref} is the reflected voltage. The first definition takes into account changing antenna input impedance with frequency, while the second is applicable to an unmatched antenna and assumes that the feed line impedance is constant with frequency. The second definition is used in this thesis, and roughly translates to the radiated power at a given angle normalized to the average power accepted onto the antenna.

5. Both transmit and receive transfer functions are considered [66]. The transmit transfer function is defined as the ratio of the electric field vector amplitude at a point in the far field to the complex amplitude of the signal at the antenna input. The receive transfer function is the ratio of the complex amplitude response at antenna output port to the source electric field amplitude at point in space.

The four candidate antenna designs are examined with the ultra-wideband measures described in this section. To select the most appropriate of the candidate designs, the results of this characterization are analyzed with the following selection criteria:

- The antenna should be well matched over the bandwidth of interest.
- The antenna should not couple to the object of interest, however should be placed as close as possible in order to minimize system dynamic range requirements. Ideally, the object should be in the far field of the antenna. A reasonable approximation to the far field is indicated by a "stable" field pattern (similar to the expected far field).
- The antenna should have as small a full-width half-maximum beamwidth as possible. This minimizes the volume of the object illuminated.
- The antenna should have relatively constant fidelity over the beamwidth in order to illuminate the object with similar signals.
- The antenna should have maximum time-domain gain to minimize energy waste.

4.2 Results: single antennas

As outlined in Section 4.1, four candidate antenna designs are simulated with FDTD and their performance characteristics are computed. The reflected energy from all designs is compared in 4.2.1. To gain insight into the behaviour of antennas near the anticipated location of the breast, fields are measured 1 and 2 cm from antennas designed in low-loss breast tissue and 0.5 and 1 cm from antennas designed in low-loss skin. The maximum amplitudes of the fields, fidelity and time domain gain are presented for antenna 1 in section 4.2.2 in order to demonstrate the use of the measures defined in this thesis. Results for designs 2, 3 and 4 can be found in Appendix D. A summary of the performance of all designs is provided in 4.2.3, where the most appropriate antennas for the breast imaging application are selected. Finally, multiple antennas are placed in an array, and their coupling evaluated by computing the transmit and receive transfer functions.

4.2.1 All antennas: reflected energy

Figure 4-7 compares S11 for all designs, demonstrating that none of the designs is matched well over the bandwidth. The total reflected energies are respectively 22% (1), 45% (2), 15% (3), and 12% (4). As the input impedance of all designs changes with frequency, Figure 4-7 underscores the difficulty of designing an ultra-wideband balun for this application.

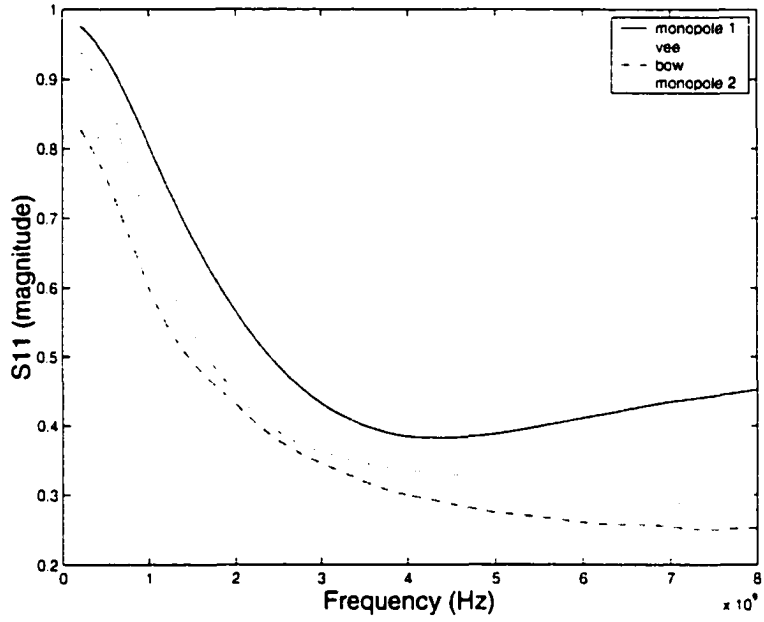

Figure 4-7 S11 for antenna designs 1 (monopole, breast tissue), 2 (monopole, skin), 3 (vee) and 4 (bowtie).

4.2.2 Antenna 1: resistively loaded monopole designed in breast tissue

Results for antenna 1 are summarized in Figure 4-8 to Figure 4-12, and the test locations are shown next to each figure. The maximum field amplitudes are presented in Figure 4-8 and Figure 4-10, indicating that the dominant field component is in the θ direction. The maximum field values for the r and θ components occur at different times (Figure 4-9), resulting in the similarity between the maximum total field and maximum θ component. Considering the results in Figure 4-8 and Figure 4-10, it can be noticed that the field amplitudes are similar to those of a regular dipole (donut pattern). The fidelity

of each component with respect to the excitation and derivative of the excitation is shown in Figure 4-11 for fields computed parallel to and 1 cm from the antenna. The dominant θ component at 1 cm is similar to the derivative, while the r component is similar to the excitation. At 2 cm from the antenna, similar patterns are observed. Time domain gain is shown in Figure 4-12, illustrating the influence of resistive loading. The fields measured perpendicular to the antenna show constant fidelity and gain patterns at 1 and 2 cm from the antenna.

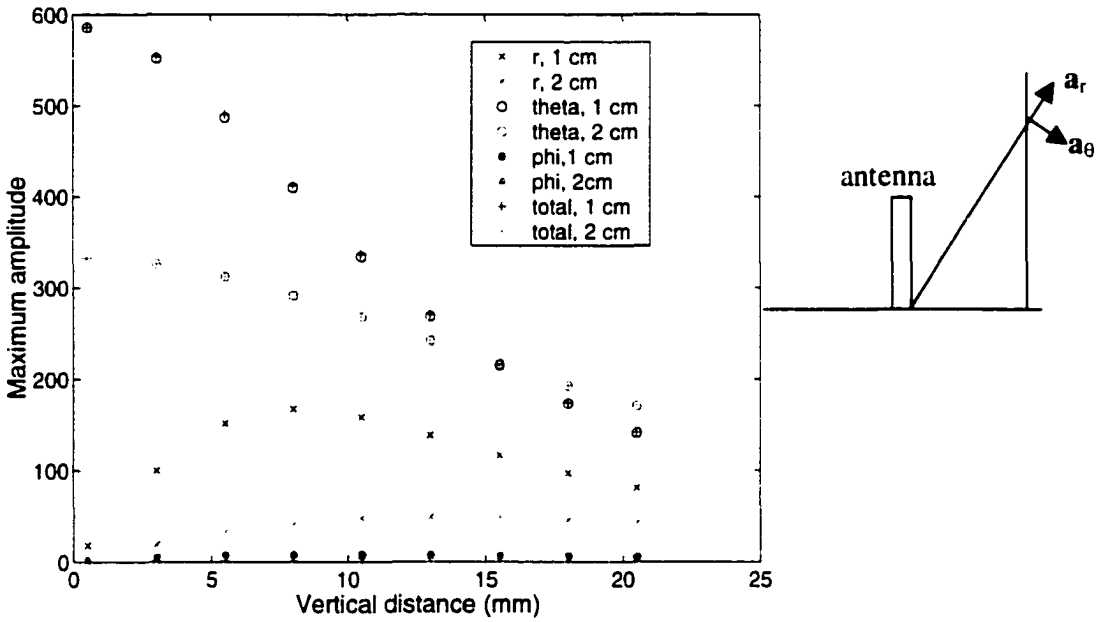

Figure 4-8 Maximum field amplitude variation with height above the ground plane. Fields are measured parallel to the antenna.

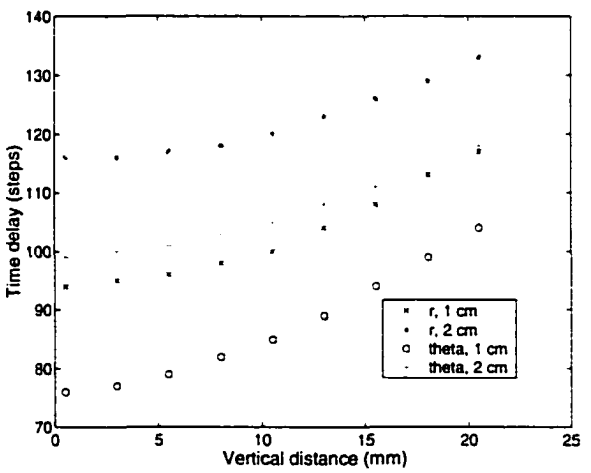

Figure 4-9 Time step at which maximum value occurs for r and θ field components.

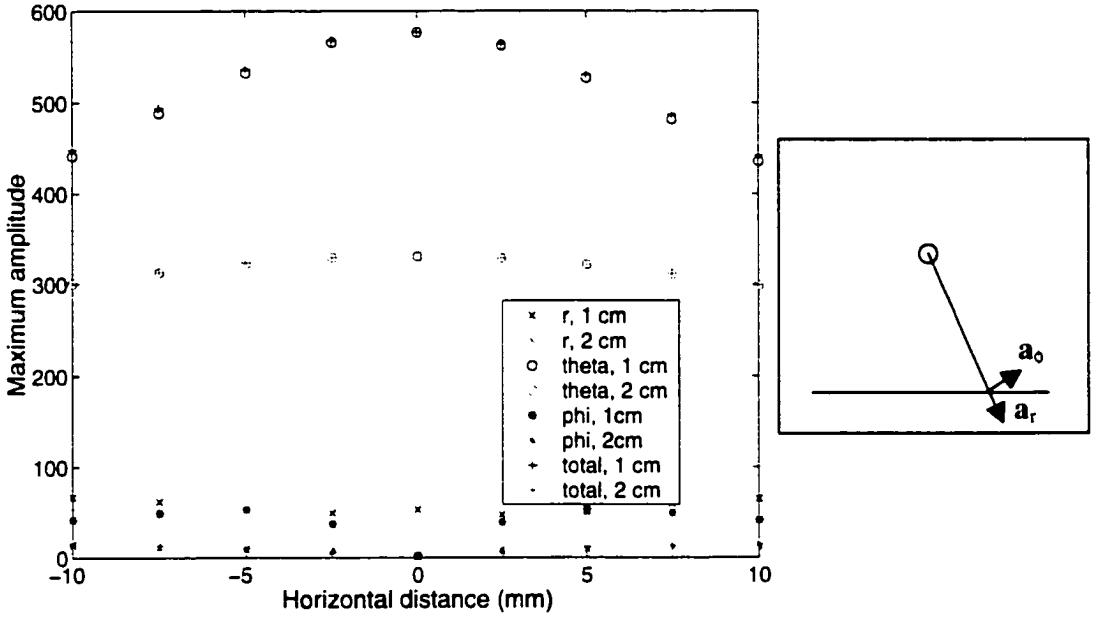

Figure 4-10 Maximum field variation with horizontal distance. Fields are measured perpendicular to the antenna at a height of 1.5 mm above the ground plane.

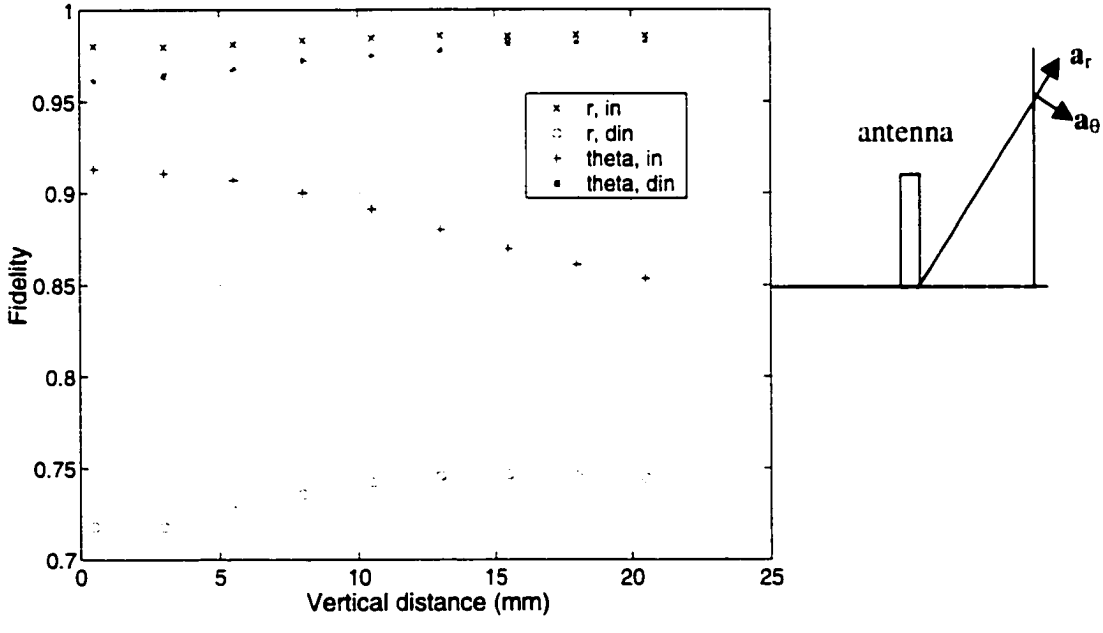

Figure 4-11 Variation in fidelity with height above the ground plane for fields measured 1 cm from and parallel to the antenna. "in" refers to fidelity to the input signal, while "din" is fidelity to the derivative of the input.

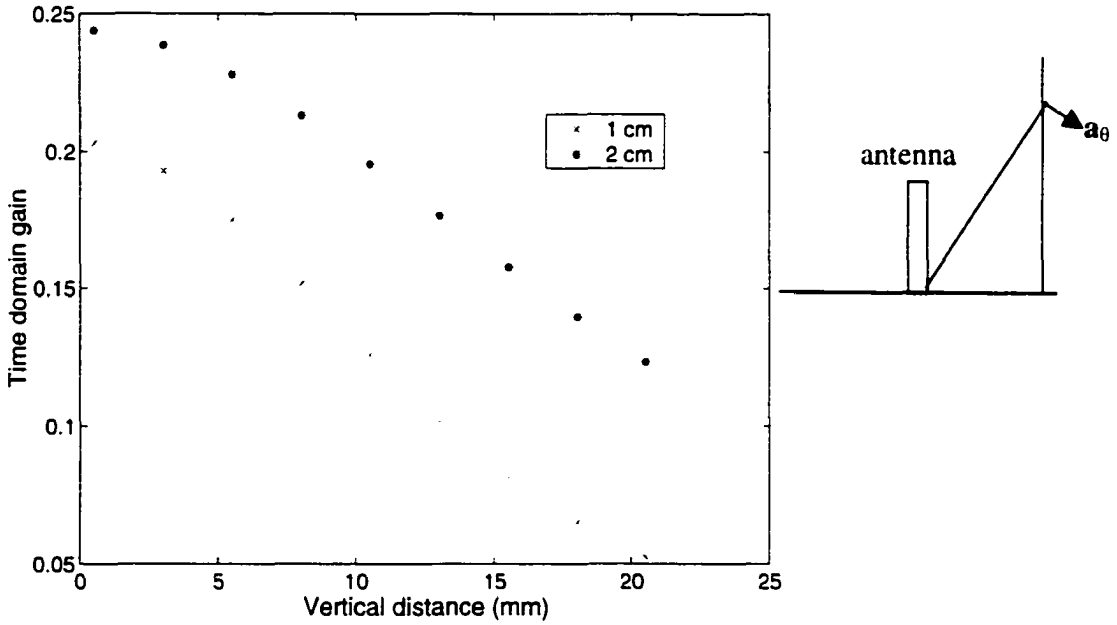

Figure 4-12 Time domain gain for dominant field components computed parallel to the antenna.

4.2.3 Summary and antenna selection

Performance characteristics of the 4 proposed antenna designs are presented in detail in 4.2.2 and Appendix D, and summarized in Table 4-1. Antennas 1 and 2 have similar performance, with well-developed field patterns evident at 1 and 0.5 cm from the antenna, respectively. Placement of the breast at these distances from the antennas is expected to have a small impact on antenna performance. The higher gain and narrower beamwidth of antenna 2 provide an advantage over antenna 1. Antennas 3 and 4 both exhibit cross-polarization (i.e. larger relative r components), partly due to use of stair-casing in the computational models. Antenna 3 has slightly greater gain than antenna 1 at 2 cm from the feed, but the increased size and computational cost of this antenna suggest that antenna 1 is preferable for this thesis work. Antenna 4 has the smallest gain, and field patterns and fidelity results suggest placement at 2 cm, thus increasing the dynamic range requirements of the system. The observed patterns and fidelity results are partly due to the width of the bowtie design. Therefore, antennas 1 and 2 are selected for further comparison in this thesis.

Table 4-1 Comparison of antenna performance. The measurement locations are indicated in brackets.

Quantity	Antenna 1	Antenna 2	Antenna 3	Antenna 4
FWHM beamwidth	21 mm (1 cm) 41 mm (2 cm)	14 mm (0.5 cm) 19 mm (1 cm)	26 mm (2 cm) 31 mm (2.5 cm)	21 mm (1 cm) 41 mm (2 cm)
Pattern comments	• similar to dipole • dominant θ component	• similar to dipole • dominant θ component	• pattern not developed at 1 cm; too close to antenna	• pattern not as well developed at 1 cm
Fidelity	• θ component has high fidelity to derivative of excitation	• θ component has high fidelity to derivative of excitation	• both components similar to derivative of excitation	• both components similar to derivative of excitation
Maximum time domain gain	0.21 (1 cm) 0.25 (2 cm)	0.3 (0.5 cm) 0.35 (1 cm)	0.28 (2 cm) 0.28 (2.5 cm)	0.1 (1 cm) 0.11 (2 cm)
Computational cost	least	Least	medium	greatest
Size	1.25 cm long	0.625 cm long	1.25 cm long 0.625 cm depth	1.25 cm long 1.3 cm wide

4.3 Results: Multiple antennas

For rapid data acquisition, the presence of more than one antenna is desirable. In this section, the performance changes with one, two and four antennas are examined. Figure 4-13 shows the arrangement of the 4 antennas of design 1 considered here. One antenna is pulsed, and the other antennas are present but not active. Results are simulated with TOTEM (please see 5.1.2). First, voltages and currents recorded at the excited antenna are compared for the cases of 1, 2 and 4 antennas, and presented in Figure 4-14 and Figure 4-15. The voltages and currents are very similar prior to approximately 3000 time steps, suggesting that limited coupling between the antennas occurs over this time window. This is further verified in the frequency domain by calculating the input impedance of the excited antenna over the time window from 0 to 2800 time steps. With four antennas present, the differences in both real and imaginary components are less than 1% when compared to the single antenna case. Second, the electric field at the center of the array is computed with various antennas present. Figure 4-16 and Figure 4-17 show the total and difference electric fields. Together, these results suggest that

time gating is an effective method of eliminating the influence of multiple antennas that are not placed in very close proximity to each other. This is further tested with a breast model present in the next chapter.

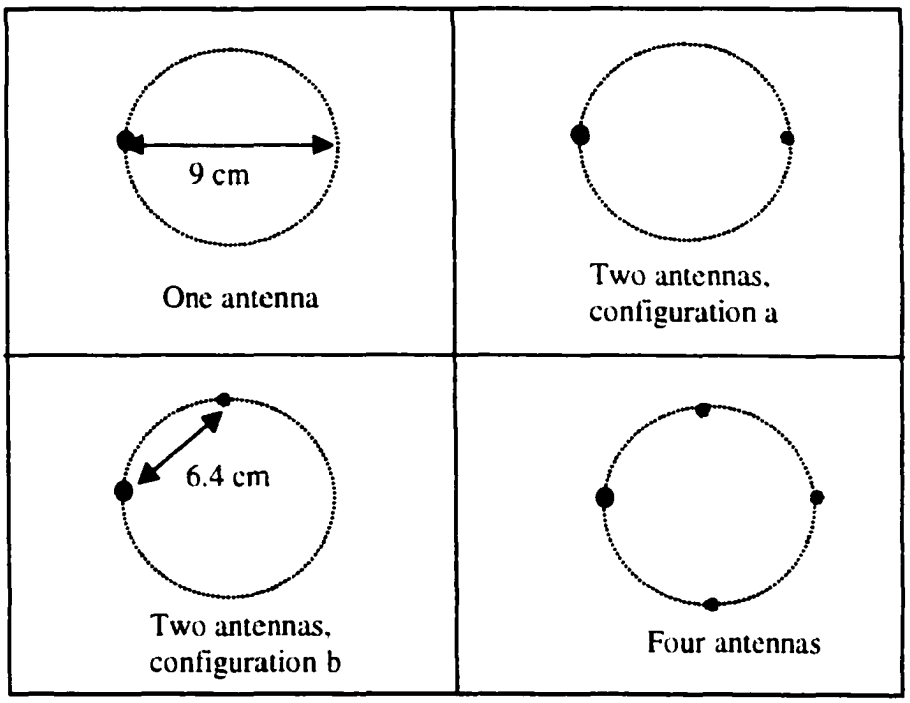

Figure 4-13 Antenna arrangements used for multiple antenna investigation.

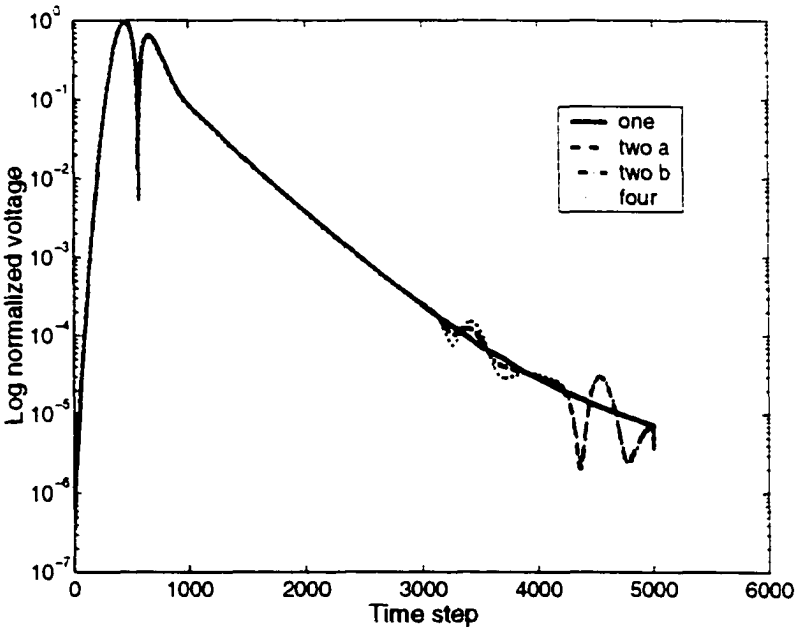

Figure 4-14 Voltage recorded at excited antenna feed with one, two and four antennas present.

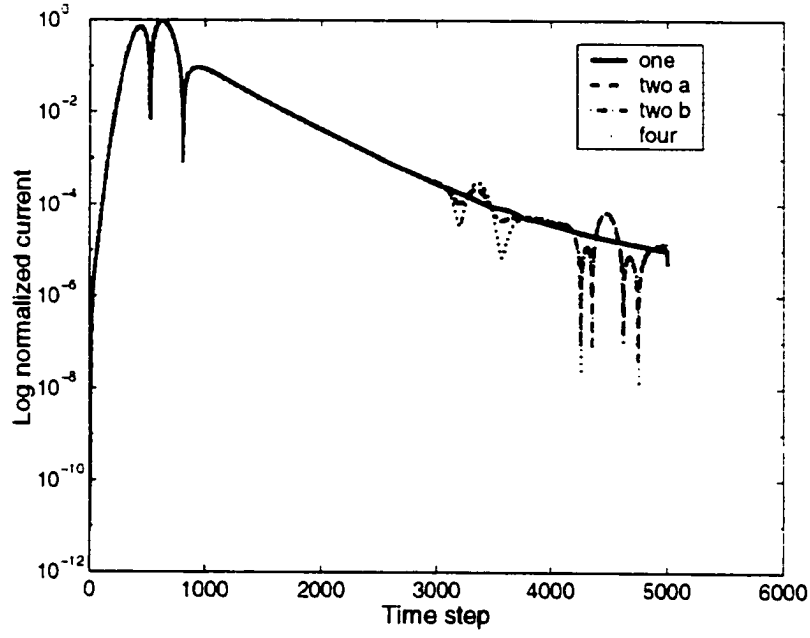

Figure 4-15 Currents recorded at excited antenna feed with one, two and four antennas present.

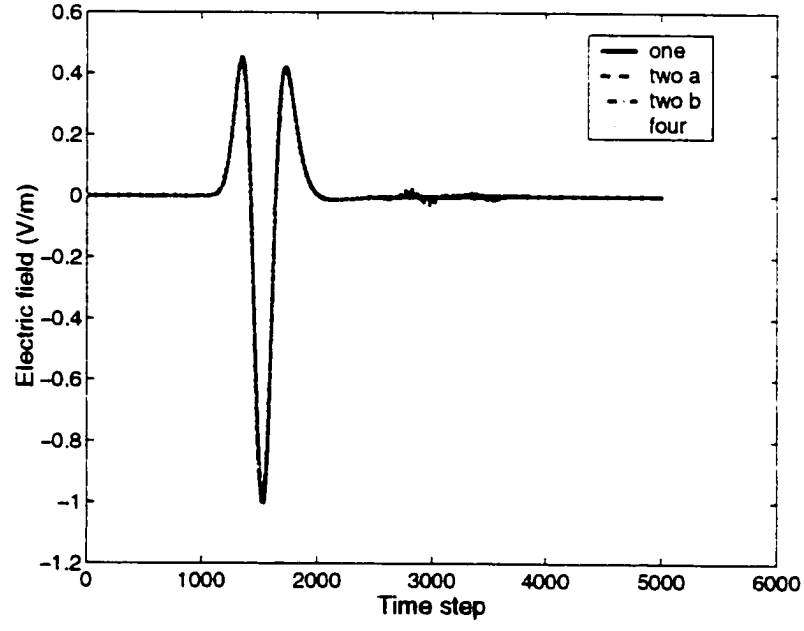

Figure 4-16 Electric fields recorded at center of array with one, two and four antennas.

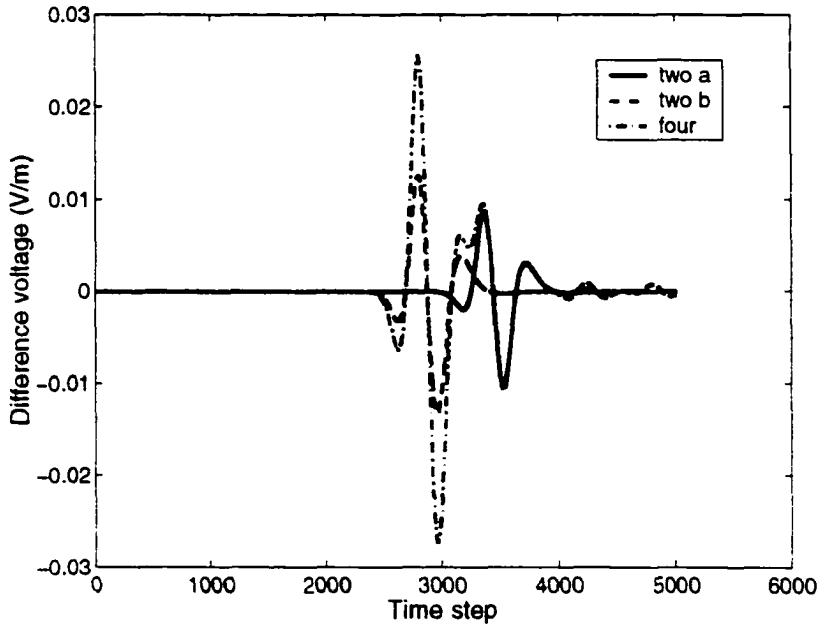

Figure 4-17 Differences in electric fields at center of array recorded with multiple and single antennas present (refer to Figure 4-16 for reference levels).

Results recorded with multiple antennas (configuration two a) are used to determine a final performance measure, the transfer function (Figure 4-18 and Figure 4-19). Fields at the center of the array are compared to the input signal and the received voltage. The transmit transfer function shows behaviour consistent with the derivative previously observed in evaluation of fidelity. The receive transfer function is within 3 dB of the maximum amplitude from 0.645 to 5.35 GHz. This implies that the antenna transmits the derivative and receives a signal similar to the incoming field.

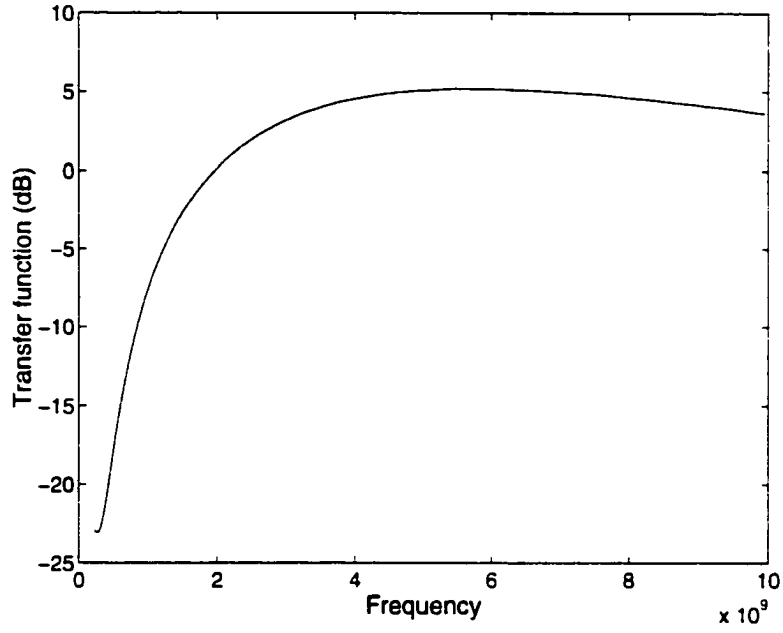

Figure 4-18 Transmit transfer function, comparing the radiated field to the input signal.

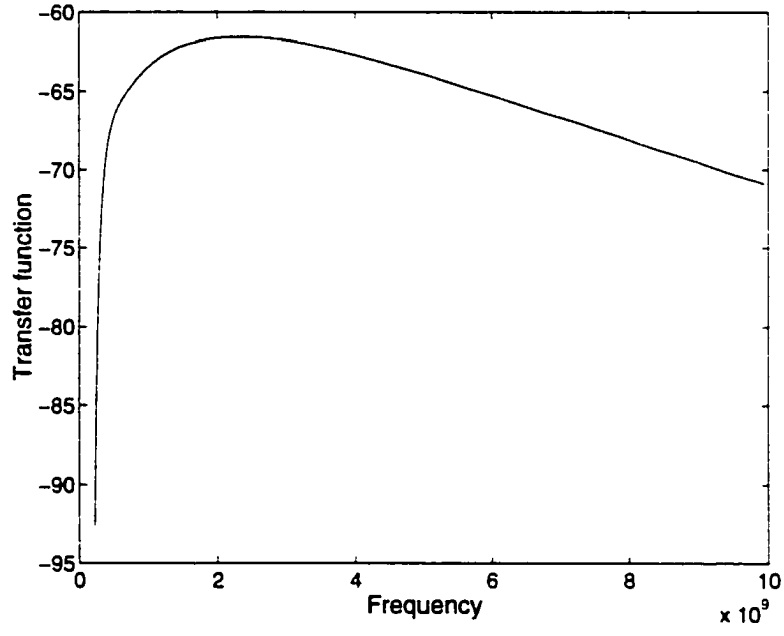

Figure 4-19 Receive transfer function, comparing the incoming field to the received signal (units are dB).

4.4 Concluding Remarks

In this chapter, four candidate antenna designs are evaluated with performance measures specific to the ultra-wideband excitation and the breast imaging application. This allows for selection of two designs for further investigation. Both of the selected antennas are resistively loaded dipoles, one designed in low-loss breast tissue and the other in low-loss skin. Performance measures indicate that the breast may be placed 1 cm (breast tissue) or 0.5 cm (skin) from the antennas. Additionally, the antennas radiate a derivative of the excitation signal and receive a reasonable replica of the incident field. These observations are incorporated into the signal processing methods introduced in the next chapter. Placing up to four antennas in a circular array tested the feasibility of using multiple antennas for data collection. Results indicated that sufficient spacing between antennas and application of time gating allow for use of multiple antennas. This is further tested with a breast model in the next chapter.

5 Breast imaging

Confocal microwave breast imaging involves illuminating the breast with an ultra-wideband signal, recording returns and processing these returns to form an image. The first part of this chapter describes the steps involved in illuminating simple breast models and forming images from the recorded returns. The second part presents results obtained for a variety of breast models, illustrating both the robustness of the image reconstruction algorithms and the feasibility of detecting sub-centimeter tumors at realistic depths.

5.1 Methods

For this thesis, computer simulations are used to model the illumination of a breast model with the antennas selected in the previous chapter. This section begins with descriptions of the simple and more complex breast models, as well as simulation methods. Once the returns from the breast are computed, image reconstruction algorithms are applied. Five steps comprise these algorithms: calibration, skin subtraction, return enhancement, compensation and synthetic focussing. Each step is discussed, with particular attention given to the skin subtraction algorithm. Measures are defined to quantify the improvement in tumor response after each signal processing step. In order to compare images reconstructed with different parameters, measures of tumor detection and image quality are defined.

5.1.1 Breast models

The arrangement of the confocal microwave imaging system proposed in this thesis is shown in Figure 5-1. The patient lies in a prone position with the breasts immersed in a low-loss liquid. An array of antennas is placed in the liquid, and positioned in a circle around and offset from the breast. For data acquisition, one antenna transmits an ultra-wideband pulse and the scattered returns are recorded at the same antenna. In most simulations, only a single antenna element is present. This antenna is moved to a number of physical locations and a simulation is performed at each location in order to form a synthetic array. Translating the array vertically allows for scans of different cross

sections through the breast. As demonstrated in Chapter 4, the use of multiple antennas appears feasible and data acquisition with multiple antennas is further explored in Section 5.2.5.

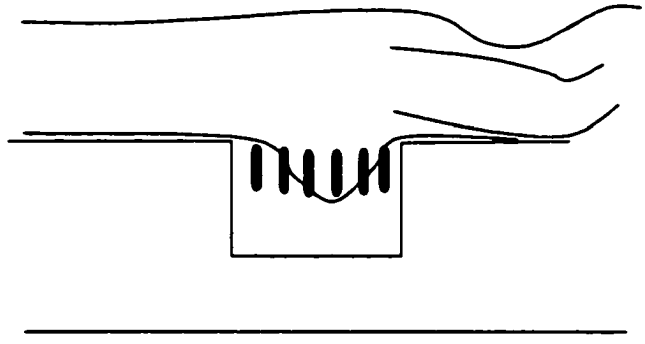

Figure 5-1 Arrangement of woman to be scanned, antennas and immersion medium (antennas are not to scale).

For evaluation of the cylindrical CMI configuration for tumor detection and localization, simple and more complex breast models are used. These models include:

- a finite cylinder containing a cylindrical tumor,
- a finite cylinder containing a spherical tumor,
- an infinite cylinder containing a spherical tumor, and
- a hemispherical model with a chest wall and inclusions mimicking ducts and containing a spherical tumor.

The cylindrical models are not realistically shaped, but reasonable approximations for initial feasibility studies of tumor detection in 2D cross-sections. The cylindrical models are also useful for developing algorithms to localize the tumor response in 3D. The selected diameters for all breast models are reasonable cross-sectional dimensions that also have relatively short computational times. Details on the models simulated in this thesis are presented in three parts. First, the shapes, dimensions and characteristics of the models are outlined. Next, material properties are specified. Finally, the antenna arrangements used to illuminate each model are described.

All breast models consist of a region of breast tissue and a thin layer of skin that encircles the breast tissue. Unless otherwise specified, the skin has thickness of 2 mm. While this

thickness may be excessive, it maximizes attenuation of the signals passing through it, providing a robust test of the tumor detection capabilities. The breast model and antennas are immersed in a low-loss liquid to reduce reflections (compared to the free space case). In this chapter, liquid 1 is a low-loss material with properties similar to breast tissue. The antenna used with liquid 1 is the resistively loaded dipole designed in the same material, as selected in the previous chapter. Similarly, liquid 2 is a low-loss material with properties similar to skin and the corresponding antenna is a resistively loaded dipole designed in liquid 2 (also selected in the previous chapter). The dimensions and shapes of the various breast models are summarized in Table 5-1. The tumor dimensions included in these models range from 2 to 6 mm in diameter. It is reasonable to consider these tumors to be small, as less than 20% of breast tumors are 5 mm or less in diameter when detected [8].

Table 5-1 Breast model dimensions and characteristics.

Model	Purpose	Immersion liquid	Breast model			Tumor		
			Shape	Diameter (cm)	Material variations	Shape	Diameter (mm)	Minimum depth (cm)
1	• detection in 2D cross-section	1	Finite cylinder	10	No	Finite cylinder	5 4	1.25 2
2	• detection in 2D cross-section • initial testing of localization in 3D	1 2	Finite cylinder (3-13 cm length, most are 7 cm)	6 6 6.2	No Yes (3D het.) No Yes	Sphere	2-6 4 6	3 (at center) 1.6 3 3.1
3	• initial localization of tumor response in 3D	1	Infinite cylinder	6.8	Yes (2D het.)	Sphere	6	2.8
4	• localize tumor response in 3D • comparison of immersion liquids	1 2	Infinite cylinder	6.8	Yes (3D het.)	Sphere Cylinder Spiculated	6 6 6 6	2.8 3
5	• more realistic breast than cylinder	1	Hemisphere	14	Yes (realistic het., Figure 5-5, Figure 5-6)	Sphere	6	~2.5

The electrical properties of the breast models are summarized in Table 5-2, and are similar to those selected by Hagness et al [41]. The estimated properties result from extrapolating measurements of normal breast tissue made at lower frequencies to higher frequencies using a Debye model. For breast tissue and skin, the values of the electrical properties are determined at approximately 5 GHz. Tumors are modeled with ε_r =50 and σ=4 S/m.. Material dispersion is not incorporated into these models. Hagness et al found dispersion of breast tissue to have a small impact on tumor detection [41]. In the frequency range of interest, skin has small dispersion [24]. In terms of dielectric dispersions discussed in Chapter 2, the frequency range of interest in CMI frequency falls between the beta and gamma dispersions. The data in Table 2.2 were determined at 100 kHz, which falls between the alpha and beta dispersions and hence results in much larger permittivity values. For both frequency ranges, the ratios between the permittivities of tumor and normal tissue are approximately 5:1

Table 5-2 Electrical properties of models

Material	Relative Permittivity	Conductivity (S/m)
Breast tissue	9	0.4
Skin	36	4
Tumor	50	4
Immersion medium • Liquid 1 • Liquid 2	 9 36	 0 0

In real breast tissue, natural variations in permittivity are suggested by the structure of the breast (e.g. glands are expected to have different properties than fatty tissue). This variation has not yet been well characterized with measurements, however it is represented in four different ways in our models.

- As indicated in Table 5-1, homogeneous breast tissue (no variation) is considered. While this is a simplification, it is useful for breast models with tumors located at the center. One simulation can be used to represent returns at an arbitrary number of antenna locations at the same distance from the breast model. This assumes no

coupling between the antennas, i.e. the antenna is mechanically scanned to each position.

- The second case considered is heterogeneous breast tissue. Variations of up to +/- 10% in the nominal electrical properties are randomly assigned to 4-mm cubes of breast tissue. This is illustrated in Figure 5-2 and Figure 5-3. In cases where the breast model is infinite, the layer of breast tissue nearest to the absorbing boundaries maintains random variations, however is lossless, as the boundary conditions at the time when the simulations were performed did not accommodate lossy dielectrics piercing through them.
- The third case is semi-heterogeneous, as shown in Figure 5-4. The 2D variations in properties are used synthesize a 3D data set for rapid development of 3D localization algorithms. This process is further described in Appendix G.

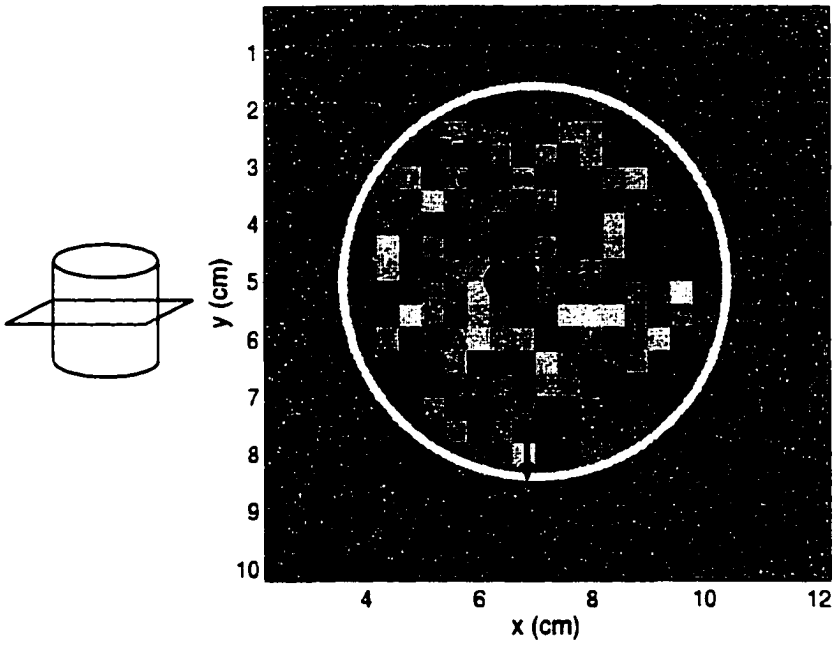

Figure 5-2 Breast model with 3D random heterogeneities: cut through x-y plane.

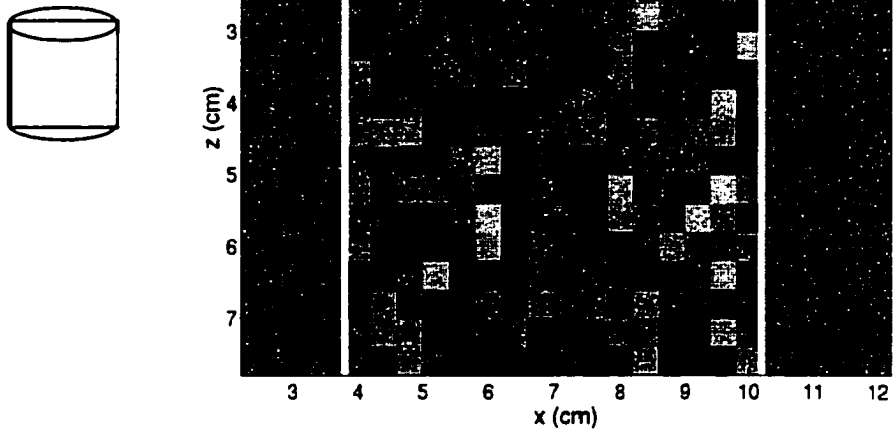

Figure 5-3 Breast model with 3D random heterogeneities: cut through x-z plane.

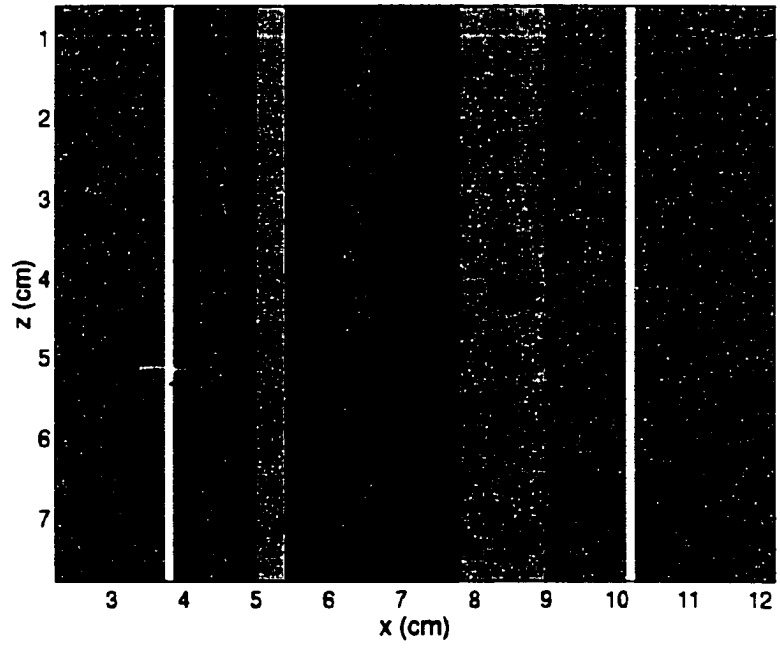

Figure 5-4 Semi-3D heterogeneities: cut through x-z plane. The x-y plane is identical to Figure 5-2.

- The fourth case is a more realistic breast model that is shown in Figure 5-5 and Figure 5-6. This model includes ducts, the chest wall and a nipple, and allows for insight into the performance of the image reconstruction algorithms with more realistic breast shapes and variations in material properties. This model incorporates additional materials with electrical properties as indicated in Table 5-3.

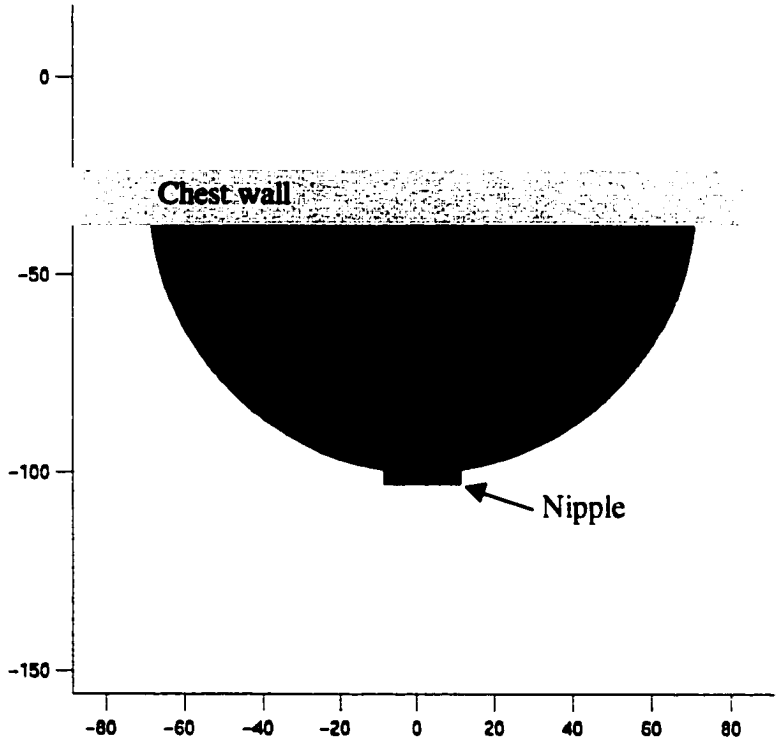

Figure 5-5 Realistic breast model: view of outer surface.

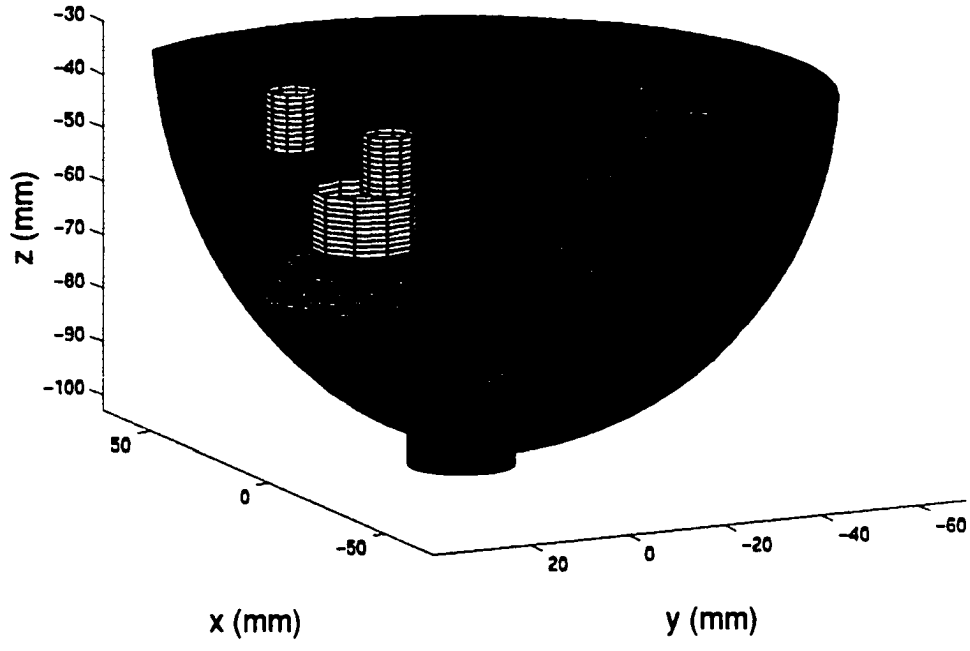

Figure 5-6 Realistic breast model: view of glands and tumor (small sphere).

Table 5-3 Electrical properties of additional materials used in realistic breast model.

Material	Relative Permittivity	Conductivity (S/m)
Chest wall	50	7
Nipple	45	5
Glands:		
1	15	0.5
2	12	0.4
3	15	0.5
4	11	0.4
5	12	0.4

Breast models are illuminated with the antenna corresponding to the immersion liquid. The antenna arrangements tested with the various breast models are listed in Table 5-4 and shown in Figure 5-7 and Figure 5-8. When the breast model is encircled by e.g. 30 antennas, fewer elements may be used to reconstruct images in order to examine the effect of varying the number of antennas. When multiple rows of antennas are used to

localize responses in 3D, adjacent rows have offset antennas. In order to provide diversity of information, the antennas spiral around the breast model.

Table 5-4 Antenna arrangements.

Model	Purpose	Figure	Distance to skin (cm)	Number of antennas	Spacing (cm)
1	Detection capability	Figure 5-7, Config. 1	3	8	1
	Influence of non-uniform distance to skin	Figure 5-7, Config. 2	2-3	15	1
	Test influence of more elements/less space between elements	Figure 5-7, Config. 2, D-J plus 6 additional antennas	2-3 2-3	7 13	1 0.5
2	Detection capability	Figure 5-8, Config. A	2	30	1
	Influence of immersion medium	Figure 5-8, Config. B	1	26	1
3	3D localization		1	30/row up to 16 rows	1 Row: 0.2
4	Immersion medium		1 0.6	30 16	1 1.5
	Detection capability and 3D localization		1 0.6	Up to 9 rows Up to 9 rows	Row: 0.5 Row: 0.25
	Multiple antennas		1	4	
5	Detection in more realistic breast model	See 5.2.4 for more details	Varying	20/row	2.25 (max) Row: 0.5

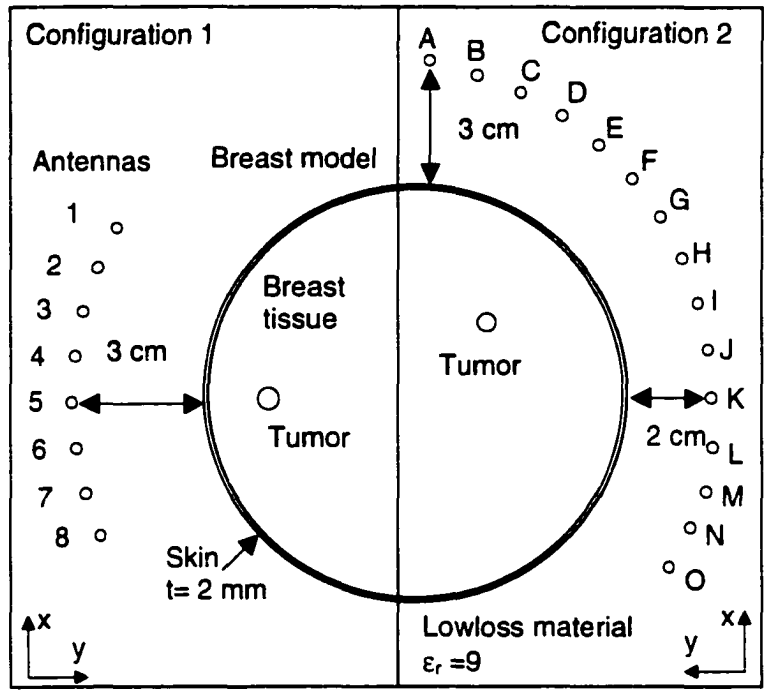

Figure 5-7 2D breast model. Configuration 1 (left) has antennas located 3 cm from the breast skin. Configuration 2 (right) features antennas located between 2 and 3 cm from the breast. All antennas are spaced by 1 cm.

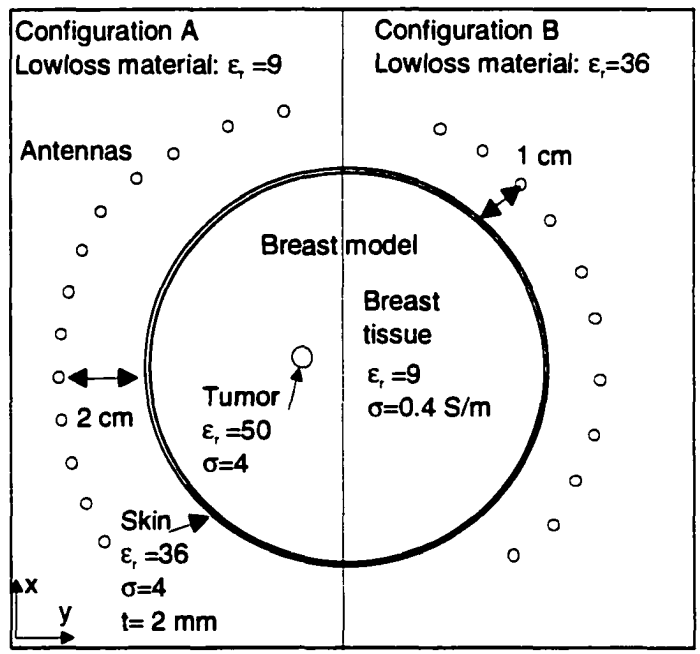

Figure 5-8 Breast model 2 with different immersion media. Configuration A is immersed in low-loss breast tissue and has antennas 2 cm from the object. Configuration B is immersed in low-loss skin and has antennas 1 cm from the object.

5.1.2 Finite difference time domain simulations

The FDTD method [108] is used to simulate the illumination of the breast model. All FDTD simulations are performed in 3D. A single, resistively loaded dipole antenna is located near the breast model, and excited with a differentiated Gaussian pulse of the form:

$$V(t) = V_o(t - t_o)e^{\frac{-(t-t_o)^2}{\tau^2}} \tag{5.1}$$

where τ=0.0625 ns and $t_o=4\tau$ for a signal with a full-width half-maximum (FWHM) bandwidth of 5.7 GHz. In most cases, a single antenna is present and individual simulations are used together to represent an antenna scanned around the model. An array with 4 elements present is also simulated. As in Chapter 4, only one element is excited and results are recorded at all elements. Graded meshes are used to increase the resolution close to the antenna (0.25 mm) and in regions of the breast model near the antenna. PMLs (parabolic profile, 8 layers, and 60 dB attenuation for models 1 and 2; 8 layers and 80 dB attenuation for all others) are placed at a minimum distance of 2 cm from the antennas or breast model. The CPU time for a simulation of the semi-3D breast model is 3.5 hours on a 4 processor SGI Origin. For the realistic breast model, the CPU time for a simulation (1.56 Gb) is 20 hours on 1 processor of an 8 node IBM RS/6000 operating at 375 MHz.

5.1.3 Signal processing

The selected antenna illuminates the breast with an ultra-wideband signal. Returns from the breast are recorded at the illuminating antenna during and after excitation. The returns consist of the incident pulse, antenna reverberations, and reflections from the PMLs, the skin layer, inhomogeneities in the breast tissue, and any tumors present. All components of the returns except for the tumor response may be considered clutter. The signal processing goals are:

- to reduce the clutter to facilitate tumor detection,

- to selectively enhance the tumor response, and
- to reliably detect any tumors present and localize the tumor response in 3D.

These goals are achieved with a combination of calibration, skin subtraction, correlation or integration, compensation for radial spreading, and synthetic focussing at a point in the domain of interest. Scanning the focal point to a set of locations in 2D or 3D forms an image. Each signal processing step is described in detail in this section.

5.1.3.1 Calibration

The calibration step involves subtracting returns recorded without a breast model present. This reduces the incident pulse, antenna reverberations, and reflections from the PMLs. From antenna characterization results, limited coupling between the antenna and breast model is expected with the breast placed 1 cm (liquid 1) or 0.5 cm (liquid 2) from the antenna. Figure 5-9 compares the voltages recorded at the antenna with and without the breast model present, demonstrating the similarity between the initial parts of these two signals. The difference between the voltages is also indicated in Figure 5-9, and corresponds to reflections from the breast model. This difference voltage is the calibrated signal. The difference voltage is much smaller than the recorded voltage, so it is important to ensure that the calibrated voltage corresponds to reflections from the breast model rather than numerical noise or error due to the subtraction of two similar quantities. First, FDTD has predictive dynamic range of up to –80 dB with PMLs [137]. The PMLs used in the simulations are specified to have 80 dB attenuation of incident pulses. To reduce any reflections from the PMLs closest to the antenna, the calibration is performed. Second, the grid sizes are selected in order to reduce the influence of numerical dispersion. Third, the reflections from a skin phantom, breast model with a tumor and breast model without a tumor are compared. Differences in the reflections are attributable to differences in the physical models (e.g. the tumor response is isolated, and the time delay of this response is found to correspond to the physical location of the tumor). Figure 5-10 and Figure 5-11 show the calibrated voltages for 4 cases: liquid 1 with the breast model located 1 and 2 cm from the antenna, and liquid 2 with the breast model located 0.5 and 1 cm from the antenna. The calibration is effective for all four

cases, and the dominant component of all calibrated signals is the reflection from the skin. This reflection must be reduced to allow for tumor detection.

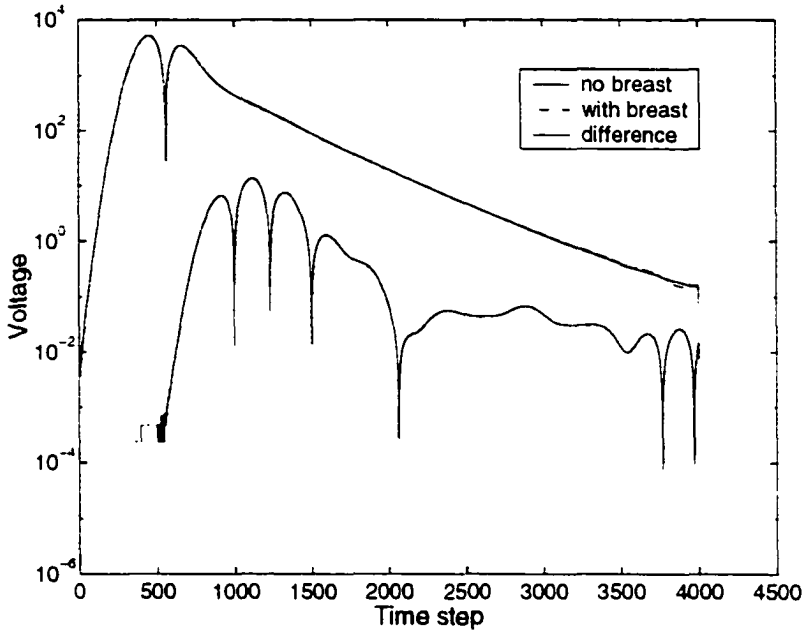

Figure 5-9 Voltages recorded at antenna feed with and without breast model present. Antenna 1 and breast model 4 are used.

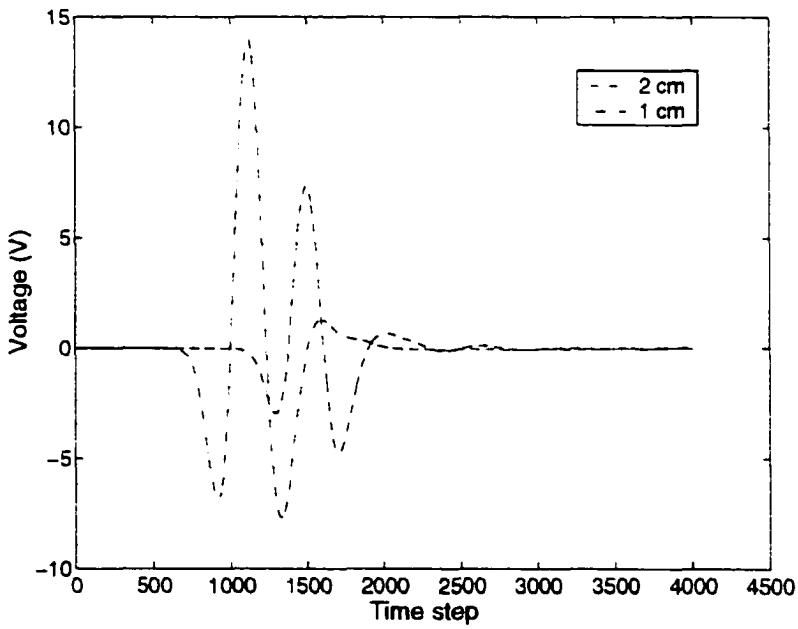

Figure 5-10 Breast model and antenna immersed in liquid 1: signals after calibration. Breast models 2 and 4 are used to obtain these results, both contain heterogeneities.

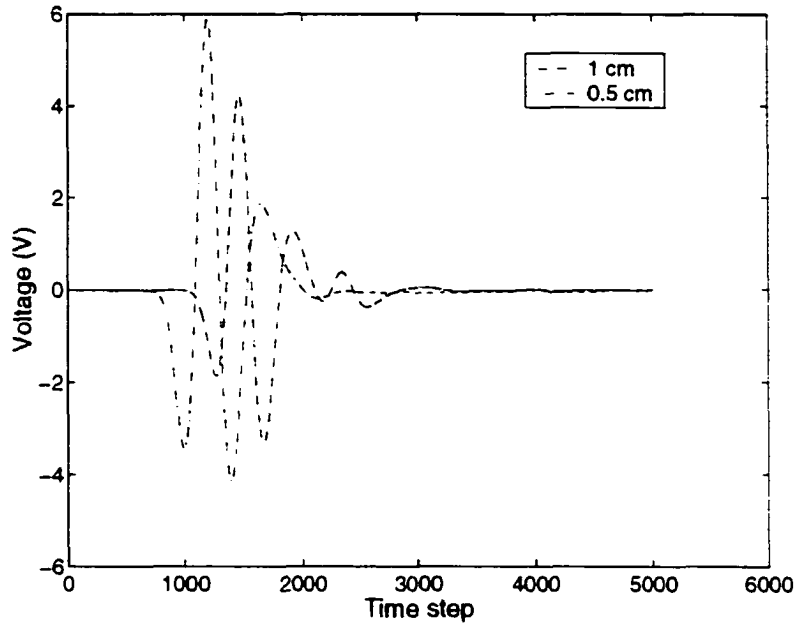

Figure 5-11 Breast model and antenna immersed in skin: signals after calibration. Breast models 2 and 4 are used to obtain these results, and both contain heterogeneities.

5.1.3.2 Skin subtraction

In the calibrated signal, the reflections from the breast skin are dominant. If an image is reconstructed without significantly reducing these reflections, then the skin reflection dominates returns from structures inside of the breast and the tumor is not detected. Two approaches to reducing the skin reflections have been developed: a phantom method, and an averaging method. The phantom method approximates reflections from the thin layer of skin using reflections from a skin phantom (i.e. a cylinder consisting only of skin). This assumes that the skin reflection is the superposition of two reflections: one from the low-loss medium-skin interface, and one from the skin-breast tissue interface. Further, the method assumes that the second reflection can be approximated by a time-shifted and scaled version of the first. The second method, averaging, assumes that each antenna "sees" similar initial reflections from the skin layer. The initial reflections may be shifted in time, however this time shift may be determined by comparing the phase of the Fourier transformed signals. After aligning the signals in time, the average of the ensemble is taken and subtracted from each signal. In this section, each method is described in more detail, and results are presented to demonstrate that both approaches are effective.

Phantom method

The phantom method approximates the reflection from the thin layer of skin with two reflections: one from a solid cylinder of skin (phantom), and the other from a cylinder of breast tissue. A conceptual model for this process is shown in Figure 5-12, and justification for this approach is presented in Table 5-5. Simulations of skin phantoms and breast models are performed with the indicated immersion media and the appropriate antennas. The recorded returns are calibrated, and the calibrated signal for the phantom is subtracted from that of the breast model. The peak-to-peak values are calculated for a) the skin phantom and b) the difference signal. These peak-to-peak values are summarized in Table 5-5 and compared to the reflection coefficients computed for planar interfaces of the same materials at 4 GHz. The ratios between the reflection coefficients and peak-to-peak values are similar for immersion in materials similar to breast tissue, indicating that the superposition of reflections from planar interfaces is a reasonable approximation to reflections from the breast model. For liquid 1, a reasonable approximation to reflection from the skin-breast tissue interface can be obtained by scaling and time-shifting the reflection from the phantom (i.e. breast tissue-skin interface). The results in Table 5-5 also suggest greater transmission of energy into the breast with immersion in liquid 2.

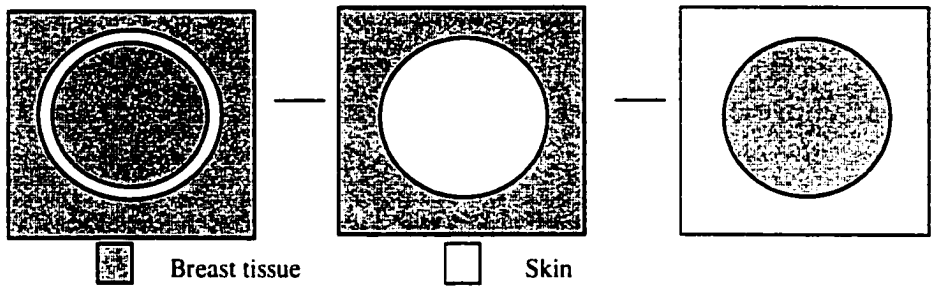

Figure 5-12 Model for phantom skin subtraction.

Table 5-5 Reflection coefficients computed for the interfaces between low-loss breast tissue and breast skin, and skin and breast tissue. The maximum reflected voltage from the skin cylinder and remainder (normalized to the energy accepted onto the antenna) are listed. Antennas 1 and 2 are used to obtain these results with breast model 4.

Immersion medium	Reflection Coefficient Magnitude		Peak-to-peak reflections	
	Interface 1	Interface 2	Interface 1	Interface 2
Low-loss breast	0.38	0.15	18.9	8.24
Lossy breast	0.18	0.075	8.87	4.2
Low-loss skin	0.12	0.34	5.05	6.8

The skin subtraction algorithm is illustrated using calibrated returns from breast model 2 and a 6 cm diameter skin phantom, both located 2 cm from the illuminating antenna. The first step is identifying the portion of the breast reflection that contains the skin returns. The derivative of the breast signal is taken, and examined near the peak of the original signal. The first local minimum to the left of the peak and the first local maximum to the right of the peak define the region of interest (Figure 5-13). The maximum value of the breast signal in the region of interest and the maximum amplitude of the skin phantom reflection are aligned. The phantom signal is scaled to the maximum breast signal value, then subtracted from the breast signal over the portion of interest. The resulting signal, or remainder, approximates the reflection from the inner skin surface. The phantom signal is then aligned with and scaled to fit the remainder. This process is shown in Figure 5-14. For a smoother transition between the original and resulting signals, the subtraction is performed over a window that slightly extends beyond the region of interest. The result of the skin subtraction algorithm is shown in Figure 5-15. In the resulting signal, the peak-to-peak voltage is 4% of the original, and the total energy is decreased to less than 1% of that in the original signal.

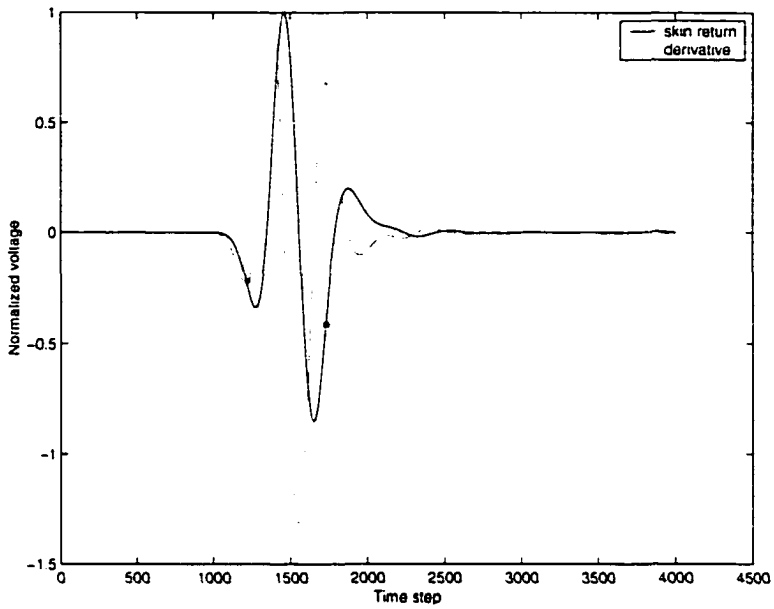

Figure 5-13 Normalized reflection from the skin and its derivative, with the extent of the signal considered in skin subtraction indicated by the stars.

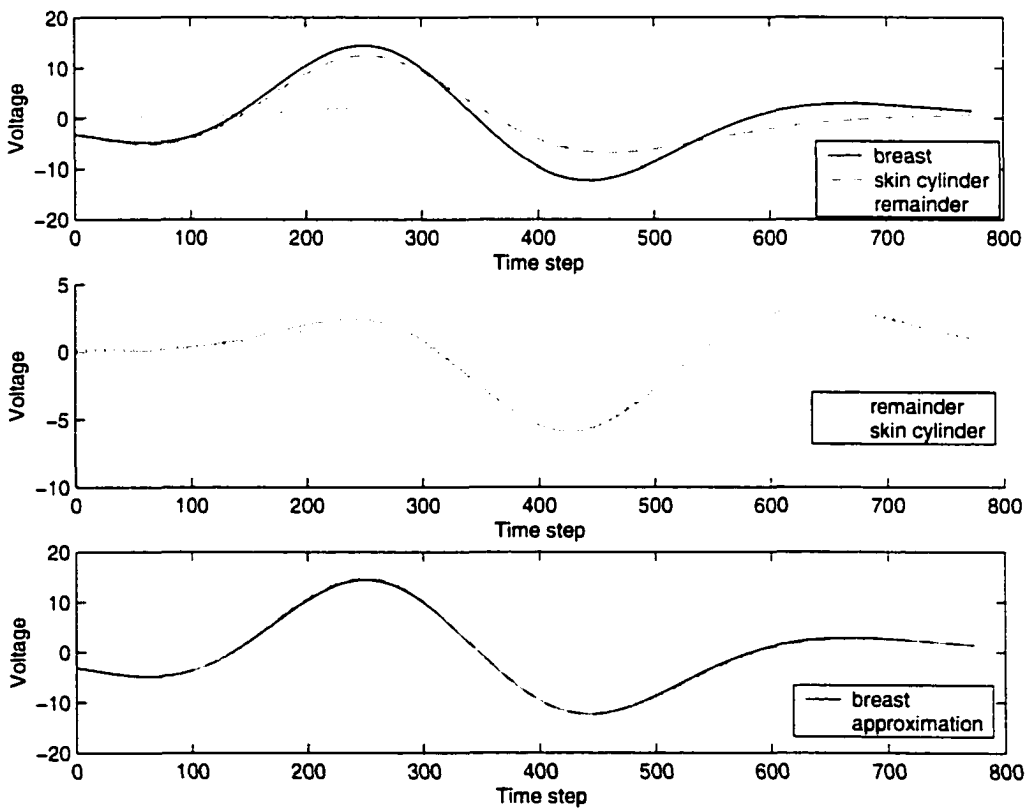

Figure 5-14 Skin subtraction process a) aligned breast and phantom returns; b) remainder and phantom; and c) breast and approximate returns.

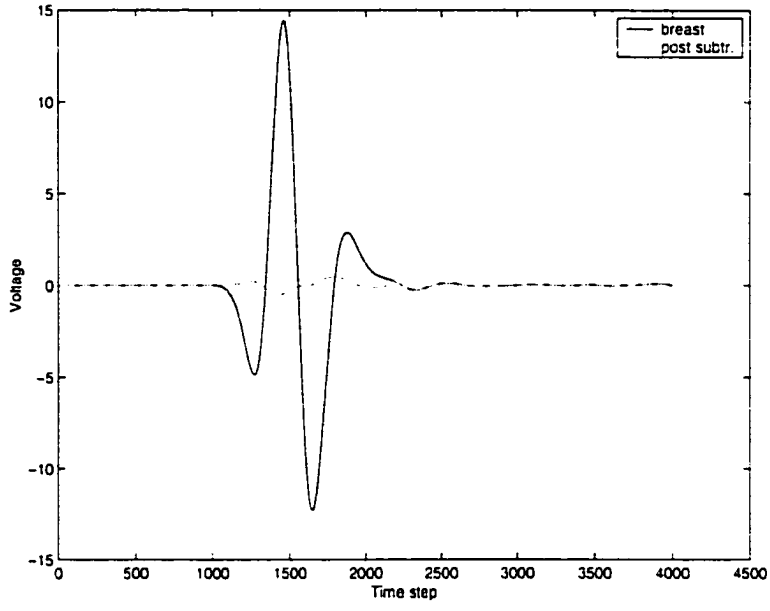

Figure 5-15 Results of phantom skin subtraction.

Additional information is obtained from the skin subtraction process, and incorporated into the image formation algorithm. The location of the first phantom reflection after alignment is used to determine skin location. Skin thickness is estimated from the difference in alignment between the phantom reflections used to approximate the signal (with an estimate of the electrical properties of skin). The robustness of the phantom skin subtraction method is assessed via the accuracy of the estimated skin location and thickness, as well as success in reducing the skin reflection. Specifically, Appendix G explores the effects of mismatches in breast model and phantom shape, size, location and electrical properties.

Averaging Method

The averaging approach is taken from ground penetrating radar [98]. This method assumes that each recorded signal includes a similar initial reflection (e.g. reflection at air-ground interface or reflection from breast skin). Assuming these signals differ by a time-shift, the peaks are aligned using phase differences in the Fourier transformed signal. The average of the resulting set of aligned signals is subtracted from each trace. The antenna locations are also adjusted to reflect shifts resulting from the signal alignment. This skin subtraction process is illustrated in Figure 5-16 to Figure 5-18.

Figure 5-16 shows the set of signals obtained from 30 antennas located 2 cm from breast model 2. The signals aligned to one of the returns (the "base signal") are presented in Figure 5-17. The result of subtracting the average response is provided in Figure 5-18. The resulting signals have 1% or less of the original energy, and the peak-to-peak voltages are an average of 6% of those in the original signals.

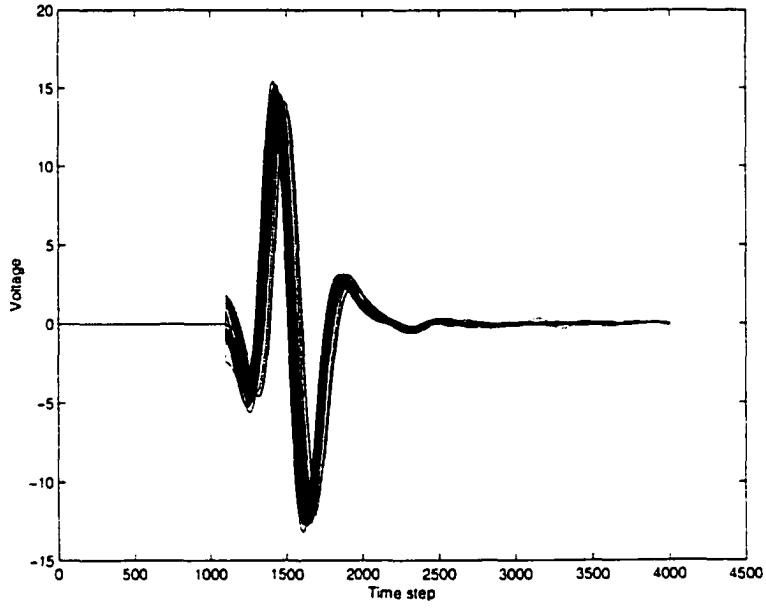

Figure 5-16 Original signals.

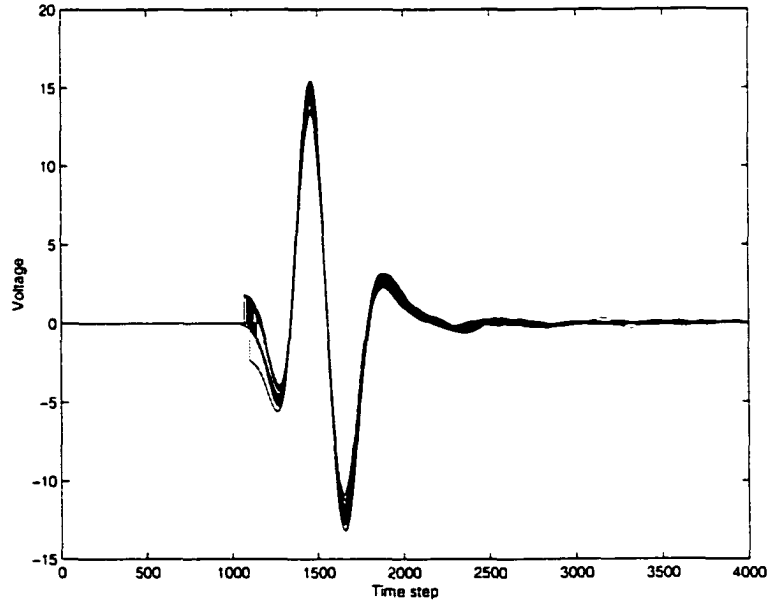

Figure 5-17 Aligned returns.

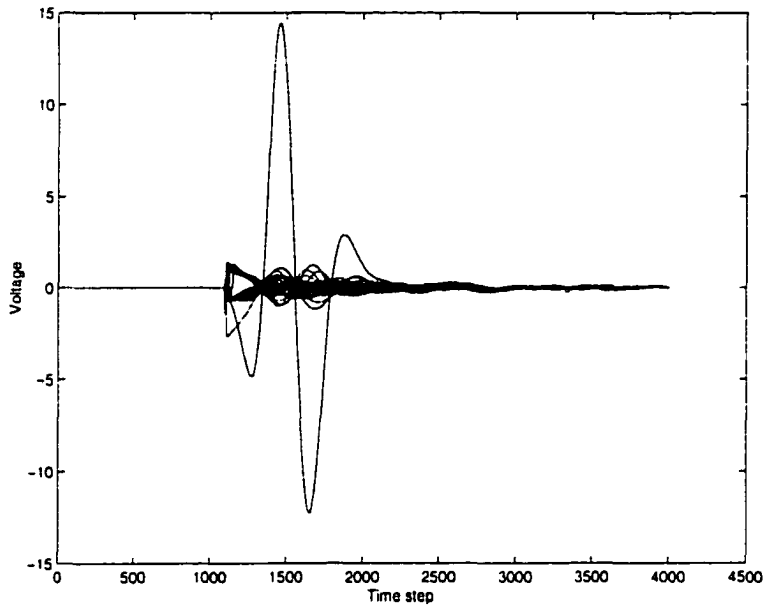

Figure 5-18 Result of averaging approach to skin subtraction.

Integrating the base signal before averaging allows for estimates of skin location and thickness (with an estimate of the electrical properties of skin), as shown in Figure 5-19. The location of the minimum provides the skin location, while the difference between the minimum and maximum is used to estimate skin thickness. The averaging approach to skin subtraction must be modified for breast models with tumors equidistant from all antennas. In this case, the subtraction is performed over a region of the signal that is identified using a threshold (i.e. window over which the signal is greater than a certain percentage of the maximum). As the case in which a tumor is equidistant from all antennas (and embedded in a cylindrical breast model) is not expected to be likely in reality, this is not considered a serious limitation of the algorithm.

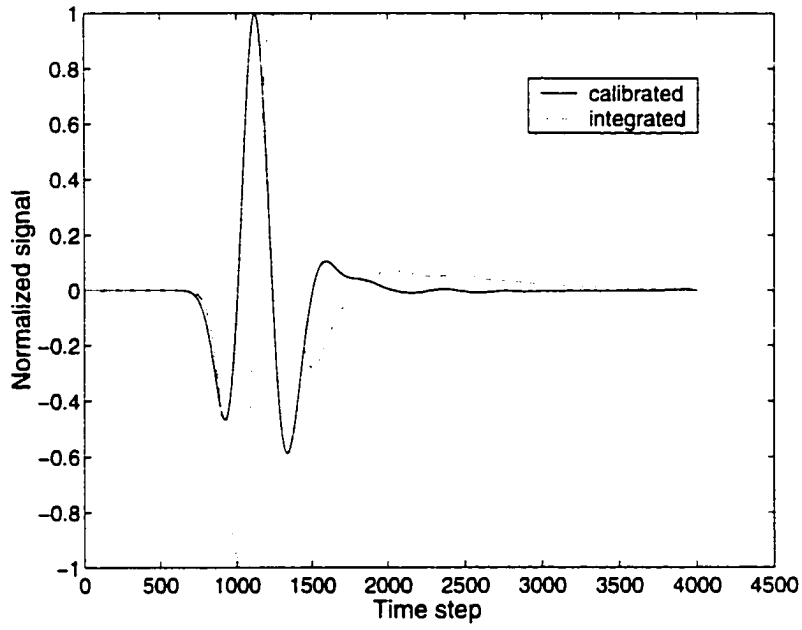

Figure 5-19 Integration of base signal provides estimates of skin location.

5.1.3.3 Return enhancement

The first two signal processing steps, calibration and skin subtraction, reduce clutter. The goal of return enhancement is selective enhancement of the tumor response. In the planar CMI system introduced by Hagness et al [66], integration is applied at this point in the signal processing sequence. The justification for this approach is related to the value of the differentiated Gaussian excitation signal. Let τ be the duration in time of the FWHM of the excitation signal. Then the excitation signal has a value of zero at time $\tau/2$, and the integrated signal has a maximum value at $\tau/2$. In the integrated signal, objects are identified by local maxima and their location is determined by time delay. For the cylindrical CMI system, antenna characterization indicates that the radiated signal at the location of the breast is a derivative of the excitation (Chapter 4). Further, the received signal is expected to be a reasonable replica of the incident field. Therefore, it is expected that the tumor is illuminated with the derivative of the excitation, and returns from the tumor are anticipated to be somewhat similar to the derivative. By correlating to the derivative of the excitation, returns with this signature are selectively enhanced (matched filter approach). In Appendix G, the results obtained with both integration and correlation are studied and compared.

5.1.3.4 Compensation

Compensation involves correcting the signal for known sources of attenuation. This includes path loss compensation, which accounts for attenuation due to propagation through a lossy material, and radial spreading, which compensates for the natural expansion of a spherical wave [98]. With an analytic approach, the path loss is estimated as:

$$PL(\vec{r}) = e^{-2\alpha|\vec{r}|} \tag{5.2}$$

where α is the attenuation constant, r is the distance from the antenna to the point of interest, and the factor 2 is included to account for the two-way journey. Similarly, radial spreading is estimated as:

$$RS(\vec{r}) = \frac{1}{|\vec{r}|^2} \tag{5.3}$$

To determine if this approach provides reasonable estimates of path loss and radial spreading, simulations are performed with antenna 1. The antenna is placed in (1) a lossless medium, (2) a lossy medium, and (3) a lossless medium at a distance of 1 cm from a slab of lossy medium. The peak-to-peak electric field values along a line perpendicular to the antenna and passing through the feed are recorded, and plotted in Figure 5-20. In this case, compensation factors are estimated for "one way" travel only. First, all results are compensated for radial spreading and the corrected results are shown in Figure 5-21. The peak-to-peak electric fields for the antenna in lossless medium are relatively constant with distance from the antenna after compensation. The attenuation factor is estimated by dividing the lossy results by the lossless results, and assuming that the model in (5.2) holds. The attenuation factor is estimated as 26. At 4 GHz, which corresponds to peak frequency content in the excitation signal, the attenuation factor is calculated as 25, which is in reasonable agreement with the simulation results. The calculated value is used to correct fields where appropriate for the second and third simulations, and the results are shown in Figure 5-22. All peak-to-peak fields are relatively constant with distance from the antenna, which is the desired result of compensation. Because the analytic approach is simple, effective and in reasonable agreement with simulation results, it is used in this thesis. The influences of path loss

and radial spreading compensation on selective tumor enhancement are further explored in Appendix G.

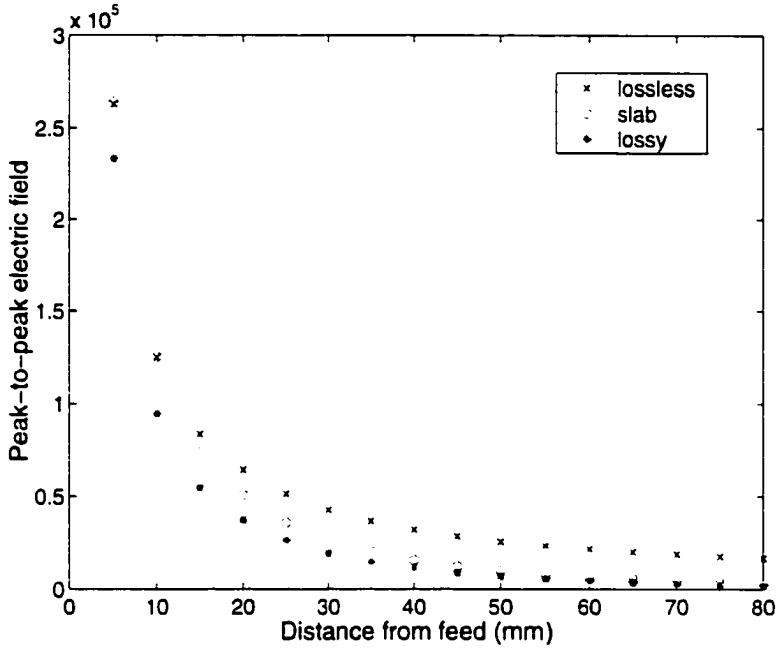

Figure 5-20 Peak-to-peak electric field variation with distance from antenna in lossless medium, lossy medium and lossless medium at a distance of 1 cm from a slab of lossy medium.

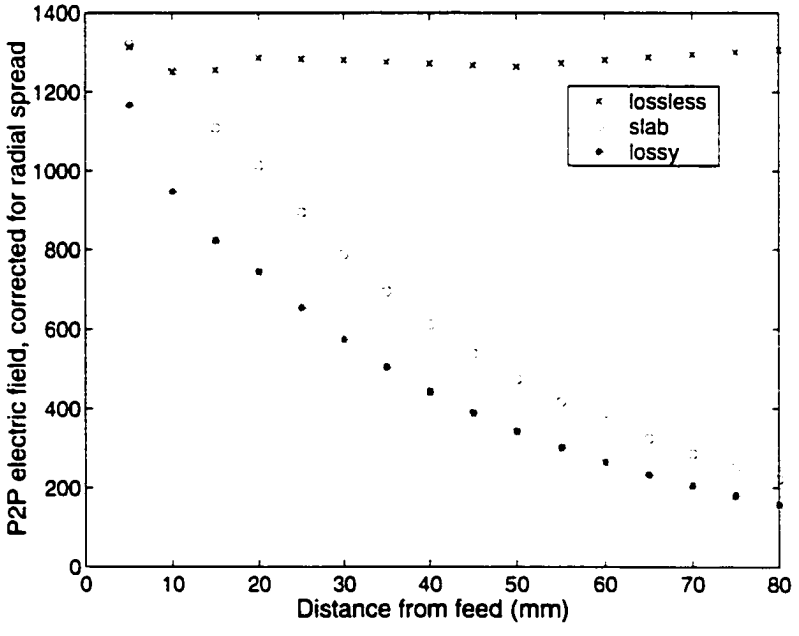

Figure 5-21 Peak-to-peak electric field after compensation for radial spreading.

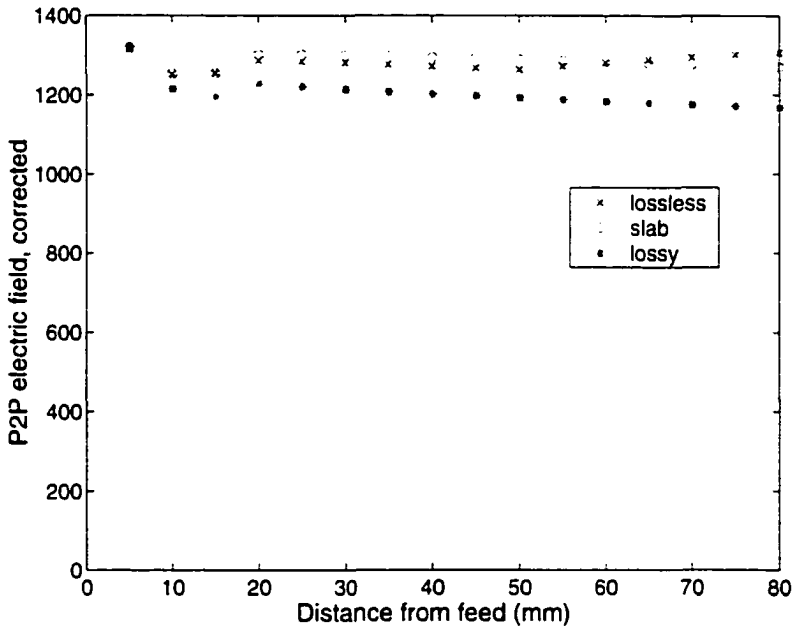

Figure 5-22 Peak-to-peak electric field after compensation for path loss and radial spreading.

5.1.3.5 Focussing algorithm (time-shift and add)

The physical basis for tumor detection with synthetic focussing is the coherent addition of returns from strongly scattering objects. That is, when the focal point is located at a tumor, the returns add coherently and a larger response is obtained. When the focal point is not located at a strongly scattering object, the returns add incoherently, thus helping to reduce clutter in the image. The basic steps in the focussing algorithm are outlined in Figure 5-23. First, the distance (d_i) from each antenna to the focal point is calculated:

$$d_i = \left| \vec{r} - \vec{a}_i \right| \tag{5.4}$$

where $\mathbf{r}$ is the focal point location and $\mathbf{a_i}$ is the antenna location. The distances are converted to time delays (t_i):

$$t_i = \frac{2\sqrt{\varepsilon_r} d_i}{c} \tag{5.5}$$

where c is the speed of light in a vacuum and ε_r is the relative permittivity of the medium. The time delays are used to identify the corresponding part of the processed signal at

each antenna ($s_i(t_i)$). The results are added together and assigned to a matrix entry corresponding to the focal point location:

$$I(\vec{r}) = \sum_i s_i(t_i) \tag{5.6}$$

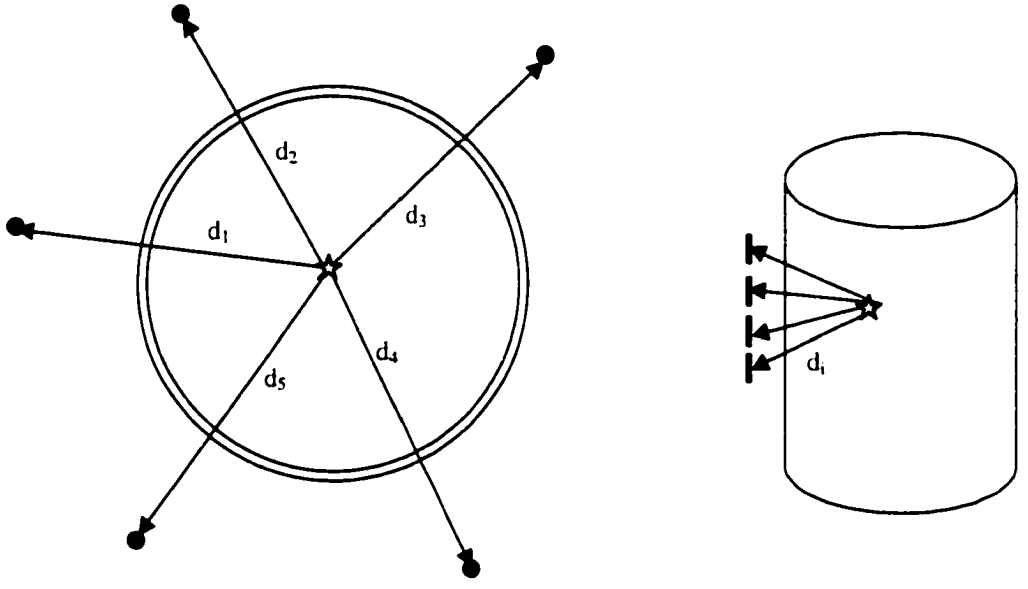

1. Calculate distance between each antenna and focal point.

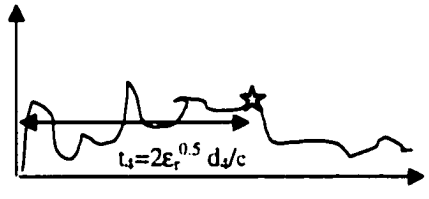

2. Convert to distance to time delay, and identify appropriate component of each processed signal.

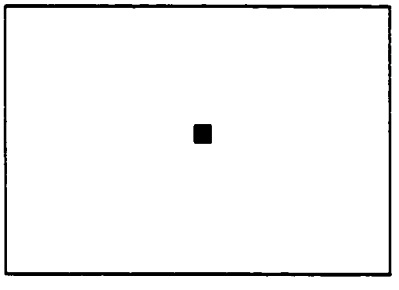

3. Sum together contributions from all antennas, and assign result to matrix entry.

Figure 5-23 Image formation process.

This simple focussing algorithm is used to create images for tumor detection and localization of the response in 2D and 3D. A few variations on the basic algorithm are explored:

- From the skin subtraction algorithm, estimates of the skin location and thickness are available. The skin location is used to identify focal points within the skin, and the thickness is used calculate an additional time delay (τ_s) to compensate for travel through the skin.
- In the equations above, the signal of interest is specified at a single time step. The physical extent of the time step then defines the minimum pixel size. In initial work, the signal of interest is averaged over a time window, W. This results in a larger pixel size, however the larger pixel size does permit localization and detection of tumors.
- For 3D reconstruction, scanning the focal point in increments corresponding to the time step results in prohibitively large matrices. For the FDTD simulations, the grid size is between $\lambda/10$ and $\lambda/20$ to minimize numerical dispersion at the highest frequency of interest. The signals are down-sampled by a factor of 10 and images are reconstructed in 2D. The resulting images have the same features as those created without down sampling. Additionally, results are very similar when the focal point is scanned in increments of 1 mm and the values at the corresponding time delays are summed. The physical features do not cause rapid changes in the signal, so this coarse sampling preserves the responses of interest.

It should be noted that this algorithm assumes that an estimate of the electrical properties of both breast tissue and skin are available. Images formed for various models are presented in Section 5.2.2.

5.1.3.6 Image display

After the focussing procedure, a matrix of values representing the response at each focal point location is available. Two approaches to image display are explored, namely taking the envelope of, or squaring the pixel values. Initially, the recorded returns are measured in volts. After calibration, skin subtraction, return enhancement, compensation and focussing, the values in the matrix are proportional to voltage. Therefore, the physical quantity displayed with the envelope approach is proportional to voltage, while squaring

the pixel values results in images proportional to energy intensity. The results of these two approaches to image display are compared in Section 5.2.2.

In addition to different methods of displaying pixel values, several approaches to clutter reduction that use information in the data are incorporated. Images may be reconstructed without skin subtraction, and the FWHM extent of the skin response into the breast identified. By displaying only the area inside of the skin response, false alarms due to incomplete skin subtraction are greatly reduced. Another method involves using the skin locations estimated with the skin subtraction algorithm to identify a set of points. These points are connected and the region inside displayed (5.2.2.2). The third method defines the volume of reconstruction and display using the location of the antennas and the estimated skin location (5.2.2.3 and following).

5.1.3.7 Image measures and comparisons

In order to quantify the success of each stage of the signal processing, as well as tumor detection and localization on images, measures are defined for single signals and images.

For the single signals, the quantity of interest is the relative tumor response and the variation in this response with each step in the signal processing sequence is studied. The tumor response is isolated by performing simulations of a breast model with a tumor and the same breast model without a tumor. By subtracting returns recorded at the same physical antenna location, the tumor response is obtained. An example of an isolated tumor response is shown in Figure 5-24. The peak-to-peak values are indicated in Figure 5-24, as the peak-to-peak response is useful for comparisons. For example, the ratio between the peak-to-peak tumor response and the peak-to-peak total signal is calculated after each signal processing step. Comparing these ratios provides insight into the enhancement of the tumor response achieved at each step. This method also allows detailed comparisons of e.g. the influence of different immersion media. In certain instances, a comparison is also made of the total energy in the signal before and after a particular step is applied.

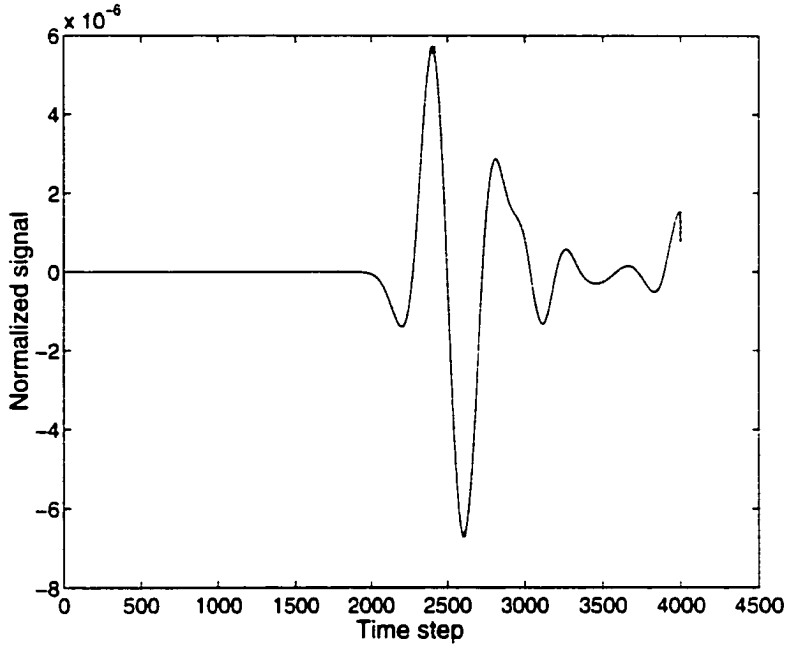

Figure 5-24 Isolated tumor response for breast model 4 with a 6-mm diameter tumor located 3 cm from the antenna.

Tumor detection and localization are of interest in the images. To measure detection, quantities representing the tumor response and the clutter are required. One approach involves isolating the full-width half-maximum tumor response, while the other compares regions of interest in the image.

FWHM tumor response

The full-width half-maximum tumor response is identified using pixel values. The size (volume and physical extent) and location of this response are calculated. A region corresponding to twice the FWHM tumor extent is then removed from the image and the maximum value of the remaining pixels is obtained. This is the maximum clutter value. Comparison of the maximum tumor response to the maximum clutter value provides the within-breast signal-to-clutter ratio. Another signal-to-clutter ratio may be computed if an image of a tumor-free breast is available. By comparing the maximum tumor response to the pixel value at the same location in the tumor-free image, the between-breast signal-to-clutter ratio is obtained. Clutter statistics are computed by taking the mean and standard deviation of pixels remaining after the tumor response is removed. This

approach provides measures of tumor response size and localization, as well as tumor detection. However, the signal-to-clutter ratios are very localized measures, and do not provide insight into e.g. how the clutter changes with number of antennas. While statistics for the clutter values remaining outside of the tumor response are useful, this approach is not the best match to medical imaging practices. Defining regions of interest allows for direct comparison of corresponding regions in similar images.

ROI approach

The region of interest (ROI) approach compares statistics for user-specified regions in the image. ROI are defined in the breast interior, surrounding the tumor and in the skin. Statistics such as sample mean and variance of the pixel values are computed for each ROI. With the assumption of normally distributed pixel values, ROI statistics are compared using standard statistical tests [110]. The assumption of normally distributed pixels is justified by the central limit theorem for large samples, and can be tested with a goodness of fit χ^2 test (Appendix E). Once this assumption is satisfied, the means of ROIs can be compared using a Student's t-distribution and the sample variances are compared using an F-distribution (Appendix E). This allows for assessment of e.g. the influence of the number of antennas on the image. When combined with measures of signal-to-clutter and tumor localization, the ROI statistics provide a comprehensive evaluation of the images.

5.1.4 Summary

The first part of this chapter described the techniques involved in forming images for breast tumor detection. First, the breast models were introduced and simulation methods outlined. Next, the steps involved in forming the images were detailed, including calibration, skin subtraction, return enhancement, compensation and focussing. Finally, measures of success were defined. The image formation process is summarized in Table 5-6.

Table 5-6 Summary of image formation process.

Step	Method	Anticipated result
Calibration	• subtract returns recorded without breast model present	• reduction of clutter due to incident pulse, antenna reverberations and PML reflections
Skin subtraction	• phantom method • averaging method	• reduce dominant reflection from thin layer of skin
Return enhancement	• correlation to reference • integration	• selectively enhance signals similar to reference • produce maximum at object location
Compensation	• radial spreading • path loss • both	• account for reduction in signal due to expansion of wave • account for reduction in signal due to travel through lossy media
Focussing	• time-shift and add signals	• coherent addition from strong scatterers (tumor) and incoherent addition of clutter
Measurement	• single signal (ratio between peak-to-peak tumor and total) • identify FWHM response of tumor • identify regions of interest	• quantify improvements at each signal processing step • quantify ability to detect tumors and changes in clutter

5.2 Results

This section examines the feasibility of tumor detection and localization, and identifies the most appropriate and effective signal processing procedures. A summary of results demonstrating the feasibility of tumor detection and localization is provided here, while details are contained in Appendix G. Single signal analysis is applied to returns recorded in both immersion media at antennas located equivalent distances from the tumor. This provides an overview of the influence of each signal processing step. Detailed analysis of the robustness of each procedure is provided in the appendices. Next, images are evaluated to determine the feasibility of detecting and localizing the tumor response. Both 2D cross-sections and 3D volumes are examined, and the results of applying different combinations of signal processing methods are compared.

5.2.1 Calibration, skin subtraction, return enhancement and compensation

To provide insight into the action of each signal processing step, the tumor response is compared to the total signal after application of each procedure. Results for both immersion media and tumors located equivalent distances from the respective antennas are summarized in Table 5-7. Case 1 is the breast model immersed in liquid similar to low-loss breast tissue, case 2 is the immersion liquid similar to low-loss skin. The tumor is located 3 cm below the skin, and the antennas are located 1 cm from the skin (1) and 0.5 cm from the skin (2). Comments based on these results and the extensive analysis of each step (Appendix G) are provided following the table.

Table 5-7 Peak-to-peak ratios between tumor and total signal. Return enhancement is calculated after averaging, and compensation is computed after integration.

Signal processing step	Ratio between peak-to-peak tumor and total signal (dB)	
	1	2
Initial	-99.6	-100.7
Calibration	-48	-44.4
Skin subtraction		
• Phantom	-26.2	
• Average	-20.1	-14
Return Enhancement		
• Correlation	-17.3	-11.5
• Integration	-23	-15.9
Compensation		
• Radial spread	-7	-9.1
• Path loss	-10.7	-10.5
• Both	-8.65	-11.8

Initial signals: The peak-to-peak ratios illustrate the dynamic range challenges of a practical system.

Calibration: The peak-to-peak ratio is improved by better than 55 dB in all cases examined, as shown in Appendix G. The most effective approach involves calibration

signals recorded at each physical antenna location. The antenna impedance and reflections from PMLs change slightly with distance from the absorbing boundaries. However, this is an extremely computationally intensive approach, and is used only with breast models 3 to 5.

Skin subtraction: Both methods of skin subtraction are effective for simple breast models.

- As demonstrated in Appendix G, the phantom method is robust to mismatches between the phantom and breast model.
- The averaging approach provides larger peak-to-peak ratios, is less computationally intensive, and can be easily extended to both immersion media (Appendix G).
- For an array of antennas that encircles the breast, both skin subtraction algorithms provide indication of the breast contour. This may be used to apply a time gate to the signal in order to remove reflections from the opposite skin interface, as well as to define limits for image display to remove clutter occurring outside of the breast.
- For initial feasibility studies of 2D and 3D tumor detection in images, phantom skin subtraction is used. Further investigations incorporate the averaging approach. The specific skin subtraction algorithm used in each case is indicated in Table 5-8.

Return enhancement: Although both methods have similar effects on tumor response, correlation results in larger peak-to-peak ratios than integration (Appendix G). This suggests that integration enhances clutter as well as the tumor response. The robustness of integration and correlation to changes in tumor shape is examined. The isolated responses from spherical, cylindrical and spiculated tumors are shown in Figure 5-25. Correlation and integration have similar impact on the returns from differently shaped tumors. For example, the peak-to-peak of the normalized returns from the spiculated tumor is 1.75 after correlation and 1.71 after integration. Therefore, it appears that the ability to selectively enhance tumors of different shape is not a significant issue when selecting the method of return enhancement. The impact of each method on the clutter, and consequently the reconstructed images, is likely the deciding factor. This is further examined in Section 5.2.2.

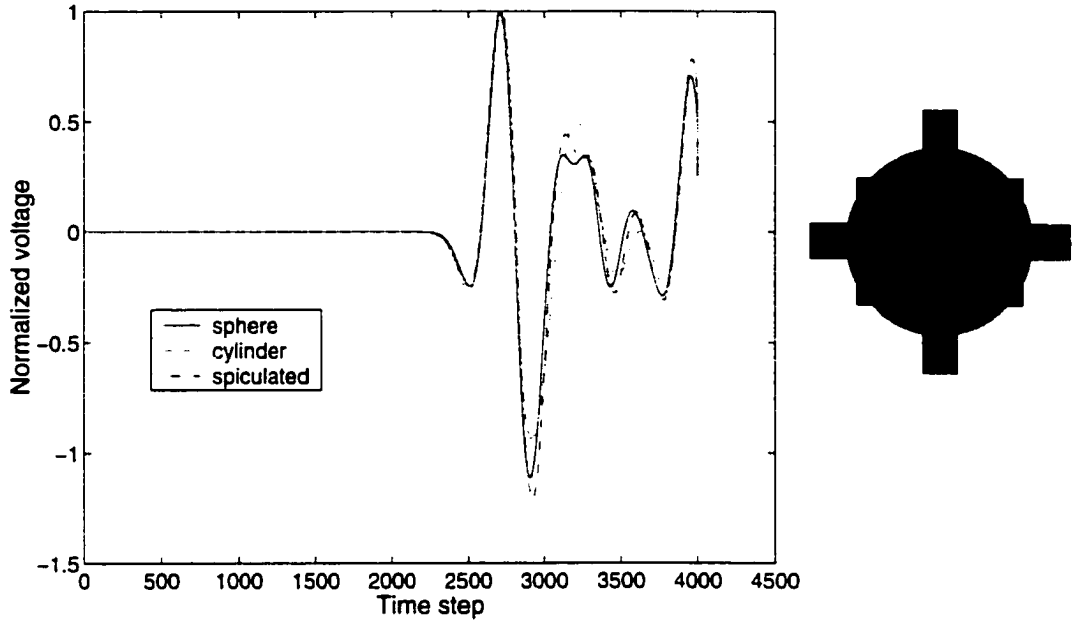

Figure 5-25 Isolated returns from a spherical tumor of 6-mm diameter, a cylindrical tumor of 6-mm diameter and length, and a spiculated tumor of 6-mm diameter. The spiculated tumor is shown in the sketch to the right of the figure. Tumors are embedded in breast model 4.

Compensation: Radial spreading compensation most effectively enhances tumor response. Appendix G compares the three compensation options in more detail.

Immersion media: Initially, the relative tumor response is larger for the system immersed in liquid 1 compared to that immersed in liquid 2. The incident pulse includes reflections due to the mismatch between the feed and antenna, so this is likely due to the greater mismatch evident with antenna 2. After calibration, the relative tumor response is greater for the system immersed in liquid 2. This larger response is maintained after return enhancement, but not after compensation, as clutter near the tumor response is enhanced.

Summary

In this section, the necessity of each step in the signal processing sequence is demonstrated by comparing the relative tumor response after application of each

procedure. The responses achieved in two immersion media are compared. Although a larger tumor response is observed with liquid 2 after calibration through to return enhancement, this is not maintained with compensation. Therefore, similar tumor responses on images are expected with both immersion media.

5.2.2 Image formation

The image reconstruction algorithms and display methods discussed in this thesis are developed to ultimately allow for detection and localization of small tumors in realistic breast models. However, not all steps are needed with all breast models. For example, detection of cylindrical tumors does not require compensation. To simplify the presentation of results, the steps used with each breast model are summarized in Table 5-8.

Table 5-8 Algorithm descriptions

Model	Calibration	Skin subtraction	Return Enhancement	Compen-sation	Focussing Window	Display
1	1 location	Phantom	Correlation	No	0.25 cm	Envelope
2	1 location	Phantom Averaging	Correlation	No	1 mm	Envelope
3	Separate locations	Averaging	Correlation	Radial spreading	No	Square
4	Separate locations	Averaging	Correlation Integration	Radial spreading Path loss	No	Envelope Square
5	Separate locations	Averaging	Integration	Modified radial spreading	No	Square

Cylindrical tumors (2D) are detected in cross-sections of cylindrical breast model with the proposed algorithms (Appendix G). The algorithms are robust to differing distances between the antennas and skin, and effectively incorporate different numbers of antennas. It appears that localized arrays are useful for evaluating suspicious areas, however the entire breast must be scanned for a screening application. In the next section, the feasibility of screening for small, spherical tumors in 2D cross-sections is investigated.

5.2.2.1 Detection of spherical tumors

Detection of spherical tumors in 2D cross-sections is explored in this section. First, images are reconstructed with and without skin subtraction to demonstrate the necessity of this procedure. The results obtained with both methods of skin subtraction are compared. In Appendix G, the use of homogeneous breast models and detection of smaller tumors are examined. The results of all investigations are summarized at the end of this section.

Images of the heterogeneous breast model are reconstructed with returns recorded at 30 antennas spaced by 1 cm and encircling the breast. Figure 5-26 and Figure 5-27 show images reconstructed with and without skin subtraction. Without skin subtraction (Figure 5-26), the skin response is the dominant component of the image. The FWHM response of the skin is about 1 cm, which agrees with the FWHM response observed in the signals before focussing. This response is larger than the physical extent of the skin, so the diameter of the breast tissue cylinder appears smaller than 5.6 cm. The FWHM response of the skin is identified using image thresholding, which zeros pixel values below the half of the maximum pixel value. The maximum extent of the FWHM response of the skin into the breast interior is indicated in Figure 5-26 with a black line. The image in Figure 5-27 is reconstructed with skin subtraction, illustrating that application of this algorithm allows for tumor detection on images. The extent of the skin response into the breast interior observed without skin subtraction is also indicated in Figure 5-27 for reference. This aids in tumor detection, as responses outside of this limit are likely due to imperfect skin subtraction and not tumors.

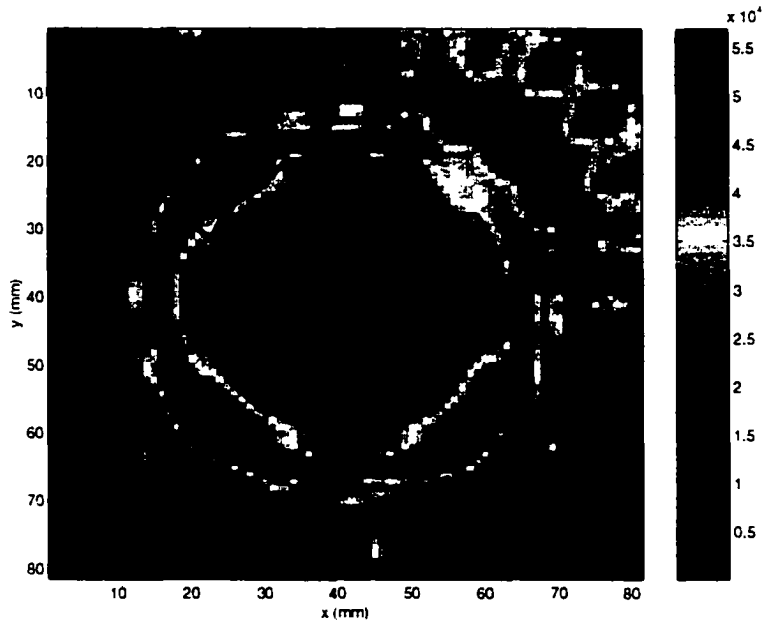

Figure 5-26 Image formed without skin subtraction. Breast model 2 is centered at (x=40 mm, y=40 mm), and is 6 cm in diameter. The red portion of the image corresponds to the skin. The line shows the inner skin surface.

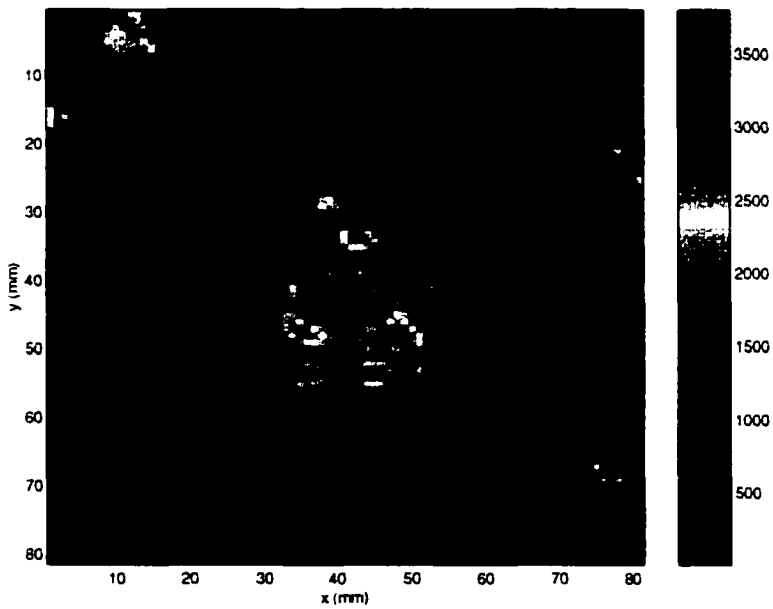

Figure 5-27 Image of breast model 2 formed after skin subtraction. The tumor is located at (x=40 mm, y=40 mm), and is 6 mm in diameter. The line shows the inner skin surface, and the boxes indicate the ROI for skin, breast interior and tumor.

The feasibility of spherical tumor detection and the necessity of skin subtraction have been demonstrated. Next, phantom and averaging skin subtraction algorithms are compared. Only the interior of the breast model, which is defined by the FWHM skin response, is displayed to facilitate this comparison. In Figure 5-28 and Figure 5-29, a 6 mm diameter tumor is located at the center of the breast model (x=70 mm, y=50 mm). Suspicious areas (i.e. pixels with larger than average returns) in the breast interior are identified, the FWHM extent of each suspicious area identified, and statistics computed for this particular ROI. Statistics for the entire breast interior are also calculated. To determine the statistical significance (please see Appendix E for details), the statistics of the suspicious areas and breast interior are used to compute the following parameter:

$$t_O = \sqrt{\frac{n_s n_i (n_s + n_i - 2)}{n_s + n_i}} \frac{m_s - m_i}{\sqrt{(n_s - 1)s_s^2 + (n_i - 1)s_i^2}}, \tag{5.7}$$

where the subscripts s and i refer to suspicious region and interior, respectively, m is a mean, s is a variance, n is the number of pixels in a given region. Table 5-9 summarizes results for the images in Figure 5-28 and Figure 5-29, as well as for tumor-free models.

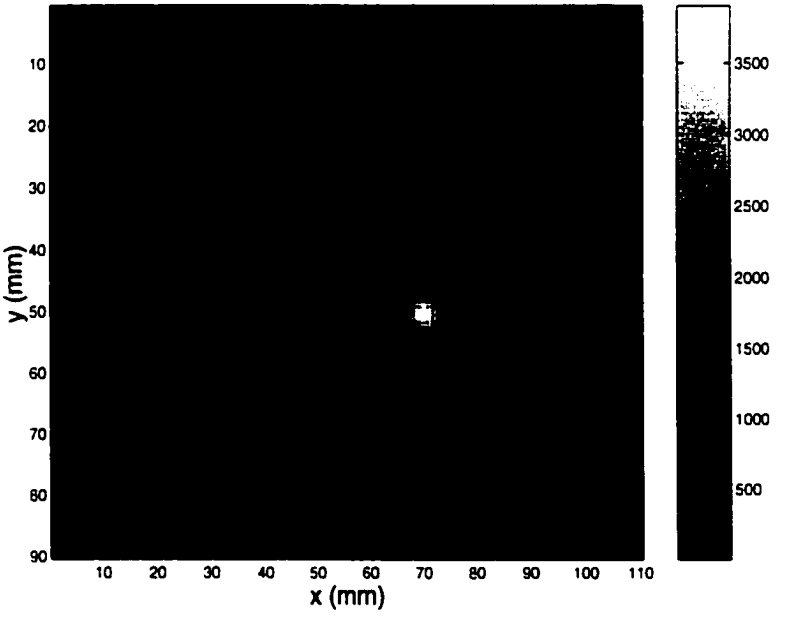

Figure 5-28 Interior of breast on image of a heterogeneous breast model 2 formed with 30 antennas and phantom skin subtraction. The image is reconstructed with 30 antenna returns and The maximum tumor response occurs at (x=71 mm, y=51 mm).

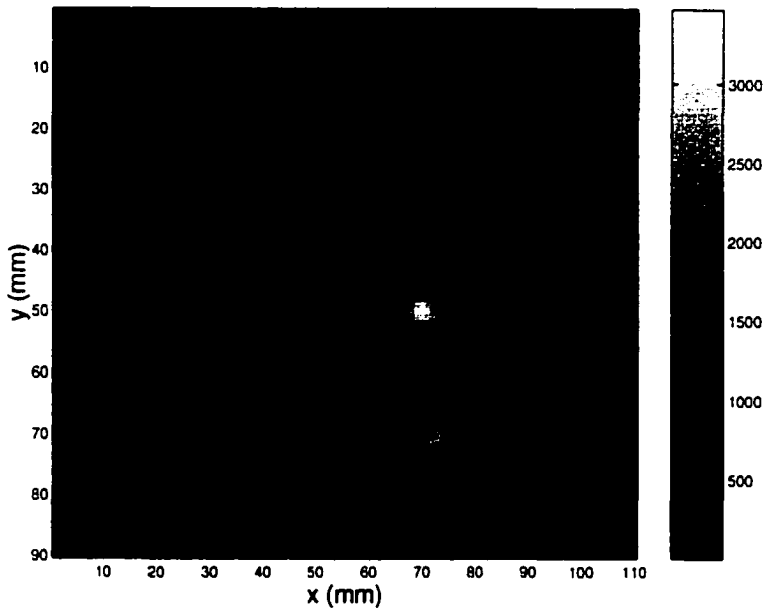

Figure 5-29 Interior of breast model 2 on image formed with 30 antennas, the averaging skin subtraction method and threshold of 3%.

Table 5-9 Statistics computed for the interior breast area. Pixels with greater than half of the maximum value (in the selected suspicious region) define the ROI. The suspicious area corresponding to the tumor is indicated with the *.

Tumor	Skin Subtraction Method	Antennas	FWHM Size (pixels)	FWHM Mean *1000	FWHM variance $*10^5$	Statistical significance
N	Phantom	30	36	1.82	1.47	7.5
			62	1.77	1.36	9.1
			60	1.89	1.1	10.7
		interior	1256	1.16	2.79	-
Y	Phantom	30	47	1.77	1.58	4.98
			42	2.81	3.41	15.01 *
			64	2.1	1.15	9.88
			59	1.99	1.24	8.24
		interior	1263	1.29	4.15	-
Y	Average	30	33	1.86	0.95	5.98
			42	2.46	2.58	14.03 *
			32	1.96	1.03	6.96
		Interior	1263	1.315	2.69	
N	Average	30	53	1.68	1.01	7.96
			79	1.55	0.83	7.27
			43	1.67	1.26	7.06
		Interior	1256	1.17	2.1	-

Table 5-9 indicates that the statistical significance is larger for tumors, while false alarms tend to have similar statistical significance. The false alarms tend to appear near the skin, so scaling the intensity of the suspicious region according to distance from skin may be helpful. This also suggests incorporation of compensation into signal processing. With the averaging method, further investigation demonstrated that increasing the threshold (i.e. value that defines window over which subtraction takes place) creates more suspicious areas and false alarms. By comparing images reconstructed with different thresholds, it may be possible to discriminate between tumors or false alarms. The averaging method results in fewer suspicious areas and smaller variances, when compared to the phantom skin subtraction method. These observations suggest that robust detection of tumors requires either improvement of image reconstruction algorithms, or a multi-variable measure. From Table 5-9, the multi-variable measure may include statistical significance, intensity of the suspicious region compared to the breast interior, variances, and distance from the skin. Improvements in image reconstruction are explored further in Section 5.2.2.2, namely compensation and alternative approaches to image display.

Summary

The results in this section demonstrate the necessity of skin subtraction and the ability to detect spherical tumors in a 2D cross-section. Advantages to the averaging skin subtraction method are demonstrated, as fewer suspicious regions are evident in the breast interior. Comparisons between images of homogeneous and heterogeneous breast models (Appendix G) indicate that, while homogeneous models are reasonable for initial feasibility testing, heterogeneous models are required for rigorous testing of algorithms and development of 3D imaging procedures.

5.2.2.2 Detection of spherical tumors: variations on image reconstruction algorithms

In this section, a breast model with an off-center tumor is used to determine the best combination of the proposed signal processing methods for robust tumor detection. That is, the influence of display methods, integration and correlation, and various methods of compensation are compared. First, images are formed with integration and correlation,

and displayed with the envelope method. The displayed region is determined by connecting the skin locations estimated at each antenna location. All images are normalized to the maximum value in the displayed region. The 6 mm diameter tumor is located at (x=0.064 m, y=0.05 m). In both images (Figure 5-30 and Figure 5-31), a response at the physical tumor location is evident. However, the maximum tumor response is approximately half of the maximum response in the image, as the clutter is the dominant feature. In both images, the clutter is especially problematic near the edges of the image. With correlation, the clutter exhibits more local maxima (increased variation). Displaying the squared pixel values instead of the envelope acts to suppress clutter, however this also suppresses the tumor response (Figure 5-32). As indicated in Appendix G, compensation is an effective method of selectively enhancing the tumor response. Figure 5-33 and Figure 5-34 show the results of applying radial spreading compensation, demonstrating the successful detection of the tumor and suppression of clutter. Larger clutter responses are evident in the image formed with correlation. In particular, responses are evident near the tumor, corresponding to the larger sidelobes observed in Appendix G. A response is also evident near the tumor in the image reconstructed with integration, however it is much smaller in magnitude. In order to examine more thoroughly the influence of the signal processing steps, the tumor response and clutter characteristics are compared in Table 5-10.

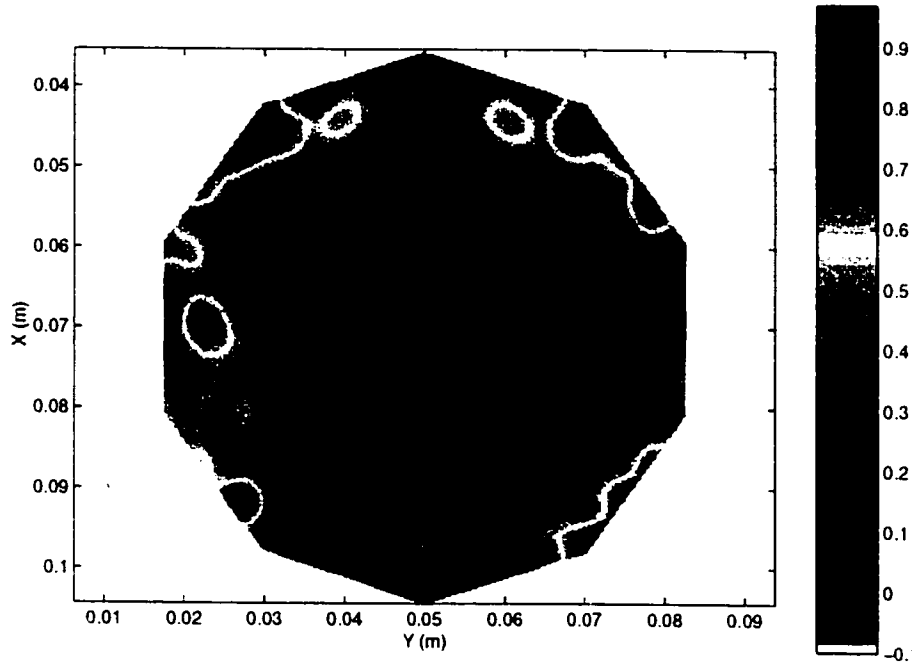

Figure 5-30 Image of breast model 4 formed with integration and displayed with envelope.

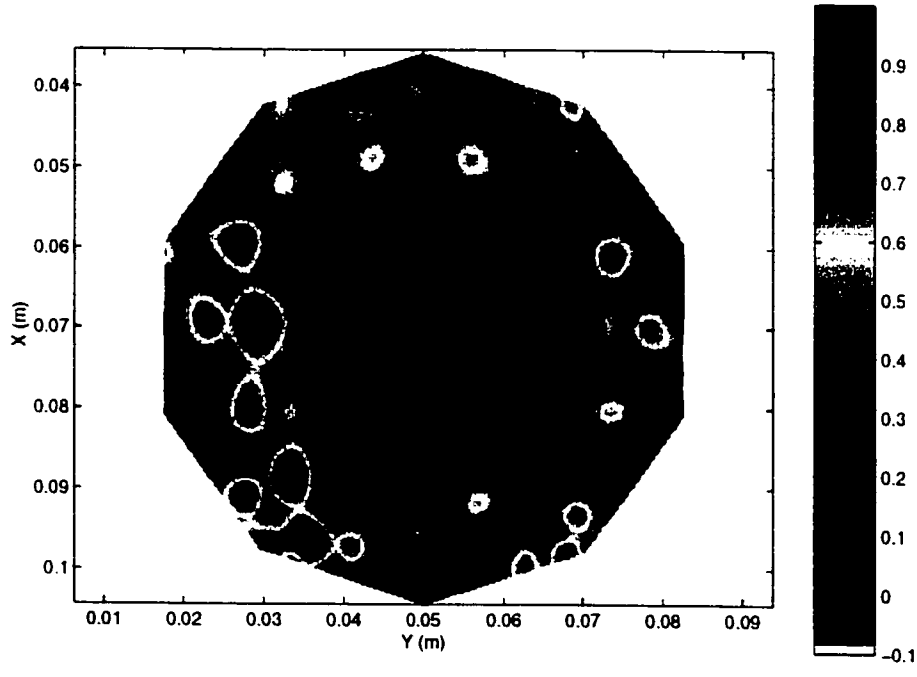

Figure 5-31 Image of breast model 4 formed with correlation and displayed with envelope.

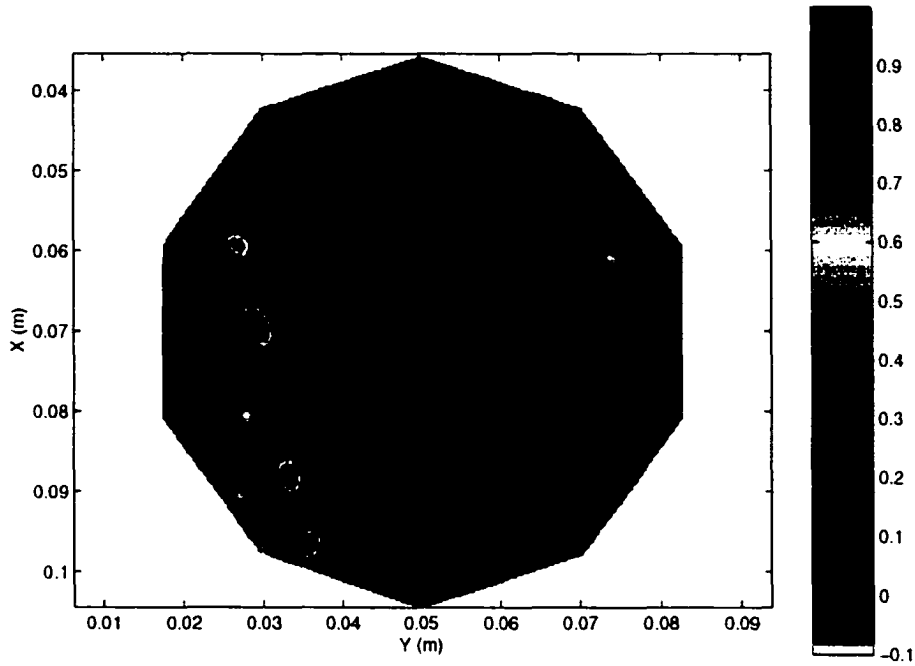

Figure 5-32 Image of breast model 4 formed with correlation and displayed by squaring pixel values.

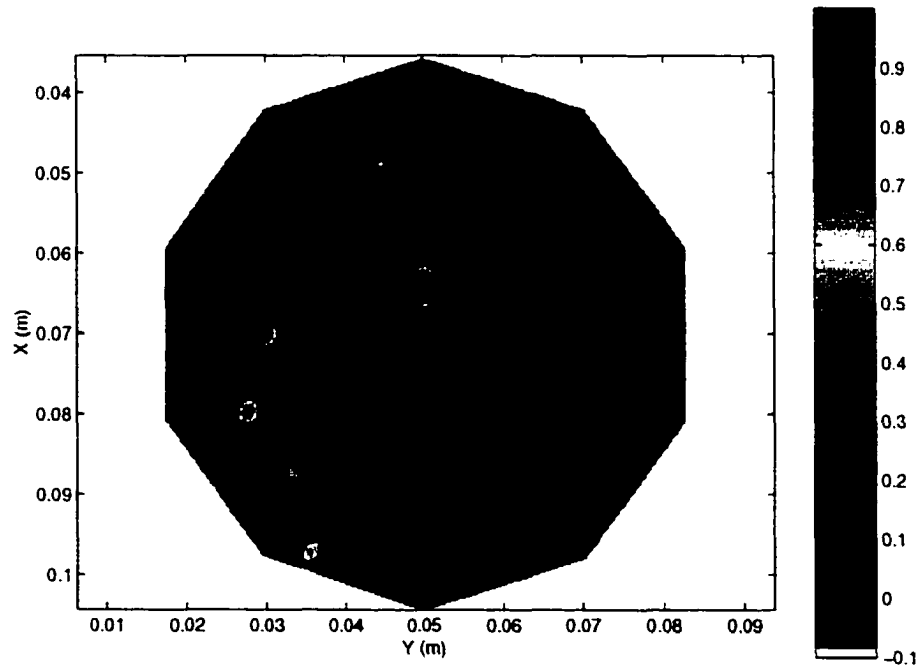

Figure 5-33 Image of breast model 4 formed with correlation and radial spreading compensation. The squared pixel values are displayed.

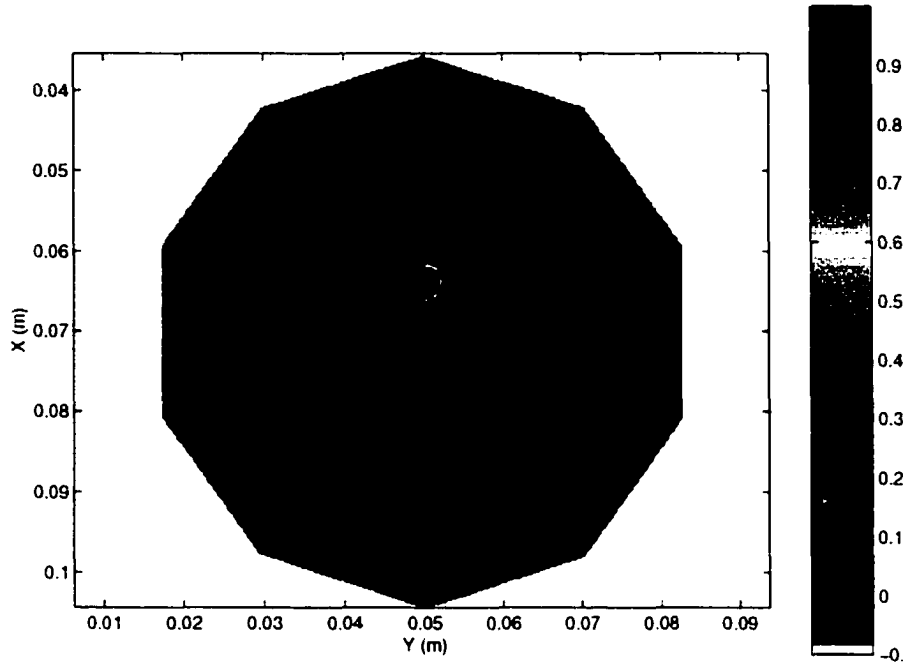

Figure 5-34 Image of breast model 4 formed with integration and radial spreading compensation. The squared pixel values are displayed.

Table 5-10 Statistics computed for images formed with various signal processing methods. Each pixel corresponds to 0.25 mm by 0.25 mm. The mean and standard deviation of the clutter are computed for a region extending from (x=47.8, y=54.5) to (x=85.3, y=67) in mm and containing 7701 pixels.

Methods			Tumor			Clutter	
			Maximum	Location x,y (mm)	FWHM Size (pixels)	Mean	Standard deviation
INT	RS	ENV	1	64,50.5	671	0.26	0.11
		SQ	1	64, 50.3	249	0.042	0.0565
XC	RS	ENV	1	64.5, 49.8	1022	0.3	0.147
		SQ	1	64.5, 49.8	240	0.064	0.096
INT	PL	ENV	0.678	64, 50.5	679	0.179	0.079
		SQ	0.923	64,50.3	247	0.04	0.055
XC	PL	ENV	0.919	64.5, 49.8	1058	0.293	0.1366
		SQ	0.845	64.5, 49.8	241	0.0588	0.0849
INT	PL+RS	ENV	No detection				
		SQ	0.66	64, 50.3	247	0.0446	0.062
XC	PL+RS	ENV	0.692	64.5, 49.8	1357	0.258	0.106
		SQ	1	64.5, 49.8	232	0.087	0.1157

In the methods column, 3 divisions refer to return enhancement (integration – INT; correlation – XC), compensation (radial spreading – RS; path loss – PL), and display method (envelope – ENV; squared – SQ).

The following observations are made from the data in Table 5-10, Appendix G and corresponding images:

- Displaying the squared pixel values provides better clutter suppression than displaying the envelope. In certain cases, displaying the squared values is required for detection.
- Dominant clutter tends to occur near the edges of the displayed region, and is especially problematic with path loss compensation incorporated. This reflects results observed in Appendix G for single signals.
- Greater clutter mean and variance result from correlation. Comparison of clutter means for correlation and integration indicates that the differences in means are not statistically significant. However, the differences in clutter variation are statistically significant.
- It appears the signal processing approach should be matched to the compensation method. For example, radial spreading compensation is most effective with integration and displaying squared pixels values. The combination of radial spreading and path loss compensation is most effective with correlation and squared pixel value display.

Summary

The averaging algorithm is effective for skin subtraction with tumors located at different distances from the antennas. Overall, radial spreading provides the most reliable detection, and the smallest variation in clutter is achieved with integration and display of the squared pixel value. To a certain extent, compensation determines the most appropriate approach to signal processing.

5.2.2.3 Tumor localization in 3D

An initial study of the feasibility of localizing the tumor response in 3D is performed with a breast model containing 2D heterogeneities. The details of the study are contained in Appendix G, show successful localization of the tumor response in 3D, and suggest appropriate numbers of antennas for further investigations. These findings are used to successfully localize the response of a tumor embedded in a breast model with 3D

heterogeneities. Images are reconstructed with correlation and integration (Appendix G), demonstrating the advantages of integration. Subsequent images are thus reconstructed using the integration approach to return enhancement. Localization in 3D is demonstrated, then the influence of number of antennas and immersion media are examined.

To rigorously test the image reconstruction algorithms, a full 3D volume is reconstructed with integration, radial spreading compensation and 9 rows of 5 antennas. Breast model 4 is examined, and is immersed in low-loss breast tissue with the antennas located 1 cm from the skin. A spherical tumor of diameter 6 mm is embedded in the breast tissue. Images of the 3 planes passing through the maximum response are reconstructed, and shown in Figure 5-35 and Figure 5-36. The third plane is similar to that shown in Figure 5-36. The maximum pixel value is located at x=64 mm, y=50 mm and z=39.3 mm, while the physical tumor location is x=64 mm, y=50 mm and z=40 mm. To ensure the validity of the results, a full 3D volume is reconstructed for a breast model without a tumor present. An image of the same plane as that shown in Figure 5-35 is present in Figure 5-37. These results demonstrate the successful detection and localization of tumors in 3D, only with a tumor present in the simple breast model.

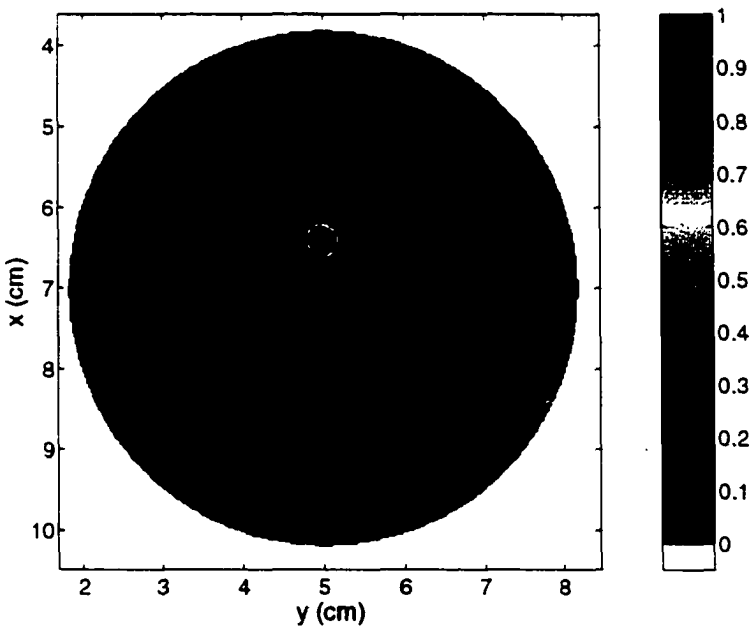

Figure 5-35 Image of xy plane at z=39.3 mm.

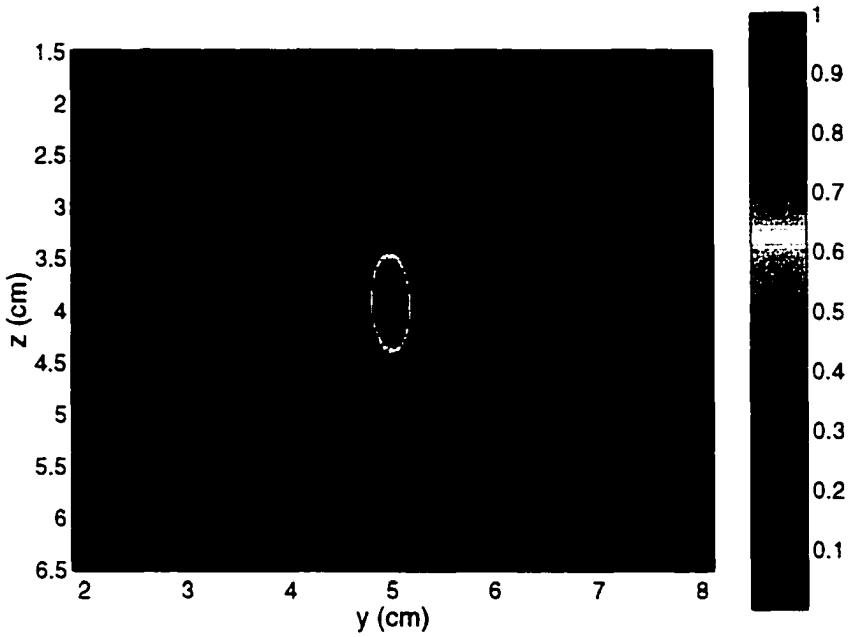

Figure 5-36 Image of yz plane at x=65.

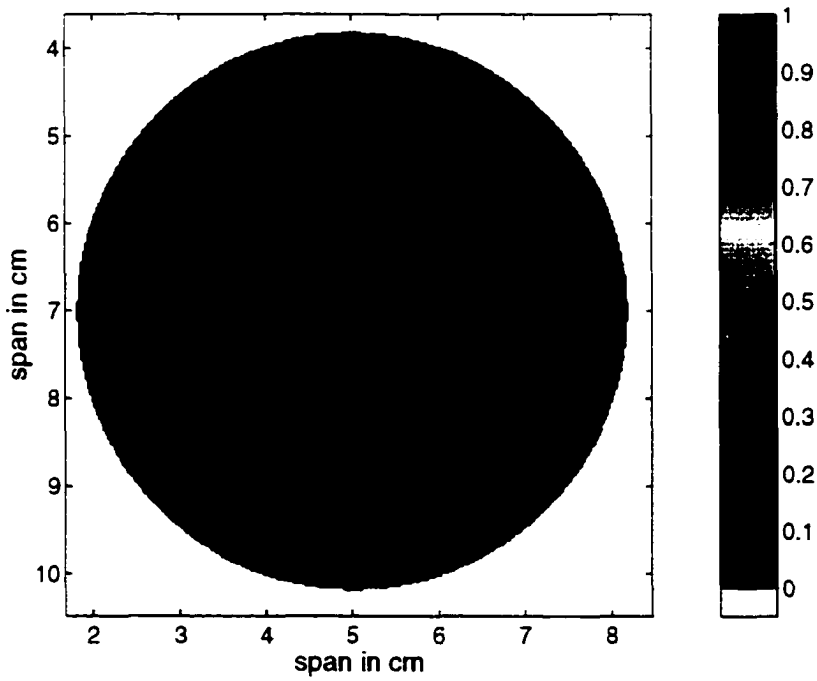

Figure 5-37 Image of xy plane at z=39.3 mm. The breast model does not contain a tumor.

The change in tumor response with change in array size is investigated by reconstructing images with various numbers of antennas. This investigation uses the same breast model

and immersion medium as the previous study. First, images are reconstructed with 5 to 9 rows of 5 antennas. The response of the tumor along the z-axis is plotted in Figure 5-38, demonstrating the improvements in both location of maximum pixel value (compared to the physical tumor location) and FWHM response. Therefore, improved localization is obtained with a larger array span. As the number of rows in the array is increased, the FWHM tumor response along the cylinder axis is expected to decrease. In other words, a tumor response more closely resembling the spherical shape of the tumor is expected with a greater array span. Images are reconstructed with two arrays having the same physical span and 9 rows of 5 antennas and 5 rows of 5 antennas, respectively. Statistics for images of breast models with and without tumors are summarized in Table 5-11. The results suggest that clutter is a more significant factor with fewer antennas, as the variance of the clutter increases and the within-breast signal-to-clutter ratio decreases. The between breast signal-to-clutter ratio appears to increase with fewer antennas, however this measure compares the response at a single pixel location and is not a good measure of overall image characteristics.

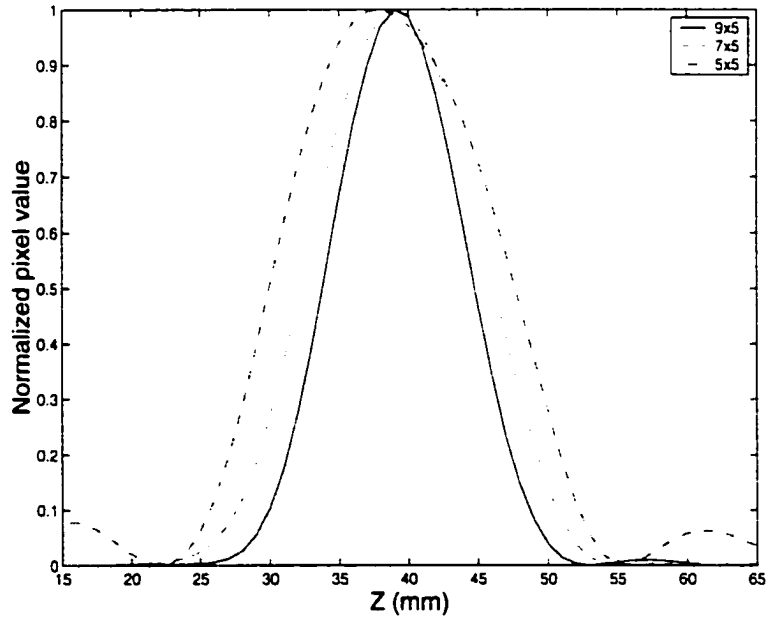

Figure 5-38 Variation in tumor response with number of rows of antennas used in image reconstruction. Breast model 4 is immersed in low-loss breast tissue and contains a 6-mm diameter spherical tumor. The 5-row configuration spans 2 cm, the 7-row array spans 3 cm and the 9-row array spans 4 cm.

Table 5-11 Statistics for images reconstructed with arrays of the same physical span but different numbers of antennas. The clutter statistics are computed with pixels outside of twice the FWHM extent of the tumor response.

Measure	N=45 (9 rows of 5)	N=25 (5 rows of 5)
FWHM tumor size:		
Volume (mm^3)	127	110
Extent (mm)	x=4.25, y=4.25, z=10	x=4.5, y=4.5, z=9.75
Signal-to-clutter ratio:		
Between breast (dB)	13	24
Within breast (dB)	4.1	2.02
Clutter statistics:		
Mean	0.029	0.04
Standard deviation	0.04	0.058
Number of pixels	10 063 168	10 057 940

The feasibility of tumor detection and localization with immersion medium 2 is explored in Appendix G. To compare results obtained with the two immersion liquids, images are reconstructed with 5 rows of 10 antennas. In liquid 1, the rows are separated by 0.5 cm, while the separation is 0.25 cm in liquid 2. Statistics for the images are summarized in Table 5-12. Similar signal-to-clutter ratios are obtained. A smaller FWHM response in the z direction is obtained with liquid 1 due to the greater physical extent of the array. This larger array provides a scan of more of the breast, which results in increased variance in the clutter, however this does not appear to degrade detection ability.

Table 5-12 Statistics for images of breast models immersed in liquids 1 and 2. Images are reconstructed over a volume bounded by the antenna and skin locations in the x-y plane, and extending 5 mm past the maximum and minimum antenna feed locations in the z direction.

Measure	Liquid 1	Liquid 2
FWHM tumor size:		
Extent (mm)	x=4, y=5, z=18	x=3, y=3, z=29
Signal-to-clutter ratio:		
Within breast (dB)	6.53	6.64
Clutter statistics:		
Mean	0.0244	0.0144
Standard deviation	0.03	0.0206

5.2.3 Comparison with planar system

A comparison study of the cylindrical and planar CMI systems has been performed in collaborative effort with researchers at University of Wisconsin-Madison [114]. For the cylindrical system, results are obtained with the breast model and 45 element cylindrical array used to reconstruct Figure 5-35 and Figure 5-36. With the planar system, the breast model consists of a half-space of heterogeneous breast tissue covered in a 2 mm thick layer of skin. A 2 cm long resistively loaded bowtie antenna is placed directly on the skin, and backed with a lossy dielectric similar to breast tissue. The antenna is scanned to 41 locations, creating an array that spans 7 cm by 9.2 cm. For both systems, image reconstruction is performed with a calibration step, integration and synthetic focussing. For the cylindrical system, the calibration step includes calibration and skin subtraction with the averaging approach. For the planar system, the calibration step consists of skin subtraction with the averaging approach. The peak-to-peak ratios between tumor response and total signal at each signal processing stage are compared in Table 5-13. Similar results are achieved with both systems; a larger response is obtained with the cylindrical system after compensation. The squared pixel values are displayed as images; statistics are computed and summarized in Table 5-14. A slightly larger within-breast signal to clutter ratio is obtained with the cylindrical system, following from the results observed after compensation. A larger between-breast signal to clutter ratio is observed with the planar system. This measure compares the pixel value at the location of the maximum tumor response with and without a tumor present. In the image of the tumor-less breast reconstructed with the cylindrical system, a larger clutter value is evident at this single pixel location. With the cylindrical system, the antennas encircle the breast in the x-y plane. The tumor is illuminated from all angles in this plane, so a more localized response is obtained in this plane compared with the planar system. The array spans 4 cm along the cylinder axis, resulting in a less localized response in the third dimension than that achieved with the planar system. Overall, results obtained with the cylindrical system are similar to those obtained with the planar system.

Table 5-13 Peak-to-peak ratios for cylindrical and planar systems. In both cases, the 6 mm diameter tumor is located 3 cm beneath the skin.

Stage	Peak-to-peak tumor/total signal (dB)	
	Cylindrical	Planar
Initial	-99.6	-94.1
Calibration	-20.1	-22.8
Integration	-23.0	-20.5
Compensation	-7.0	-11.4

Table 5-14 Comparison of images reconstructed with cylindrical and planar systems. The physical tumor location is indicated in (brackets). While the physical location of the tumor is different for the planar and cylindrical systems, an equivalent imaging task is performed (i.e. detection of a tumor at least 3 cm from the nearest antenna).

Measure	Cylindrical	Planar
Tumor location (mm)	64, 50, 39.3 (64, 50, 40)	75,75,59 (75,75,58)
FWHM tumor size:		
Volume (mm^3)	127	123
Extent (mm)	x=4.25, y=4.25, z=10	x=8.0, y=6.5, z=4.5
Signal-to-clutter ratio:		
Between breast (dB)	13	21.05
Within breast (dB)	4.1	3.53
Clutter statistics		
Mean	0.029	0.03
Standard deviation	0.04	0.04
Number of pixels	10 063 168	542 854

5.2.4 More realistic model

To further test the robustness of cylindrical CMI and the algorithms developed in this thesis, a realistic breast model is investigated. As shown in Figure 5-5, the model consists of a chest wall, hemispherical breast, glands, nipple and tumor. Images are reconstructed with slight modifications to compensation. Specifically, compensation for spherical wave expansion results in clutter enhancement when applied over longer distances. This was not an issue in previous breast models, due to the maximum diameter of 6.8 cm. With the realistic breast model, the maximum diameter is 14 cm and the following method of compensation is applied:

- compensate for spreading according to total path length, rather than multiplying the length of the paths to and from the focal point, and

- weight contributions for each antenna based on the relative distances to the focal point (i.e. contributions from distant antennas are diminished).

The resulting image is shown in Figure 5-39, and indicates the presence of a tumor near the physical location of x=130, y=95 mm. The averaging algorithm eliminates the reflection from the highly scattering nipple, as well as the curved breast skin. The clutter in the image corresponds to the locations of the glands included in the model. Clutter reduction is expected with the use of more antennas, and localization of the tumor response in 3D appears feasible with the use of a conical array.

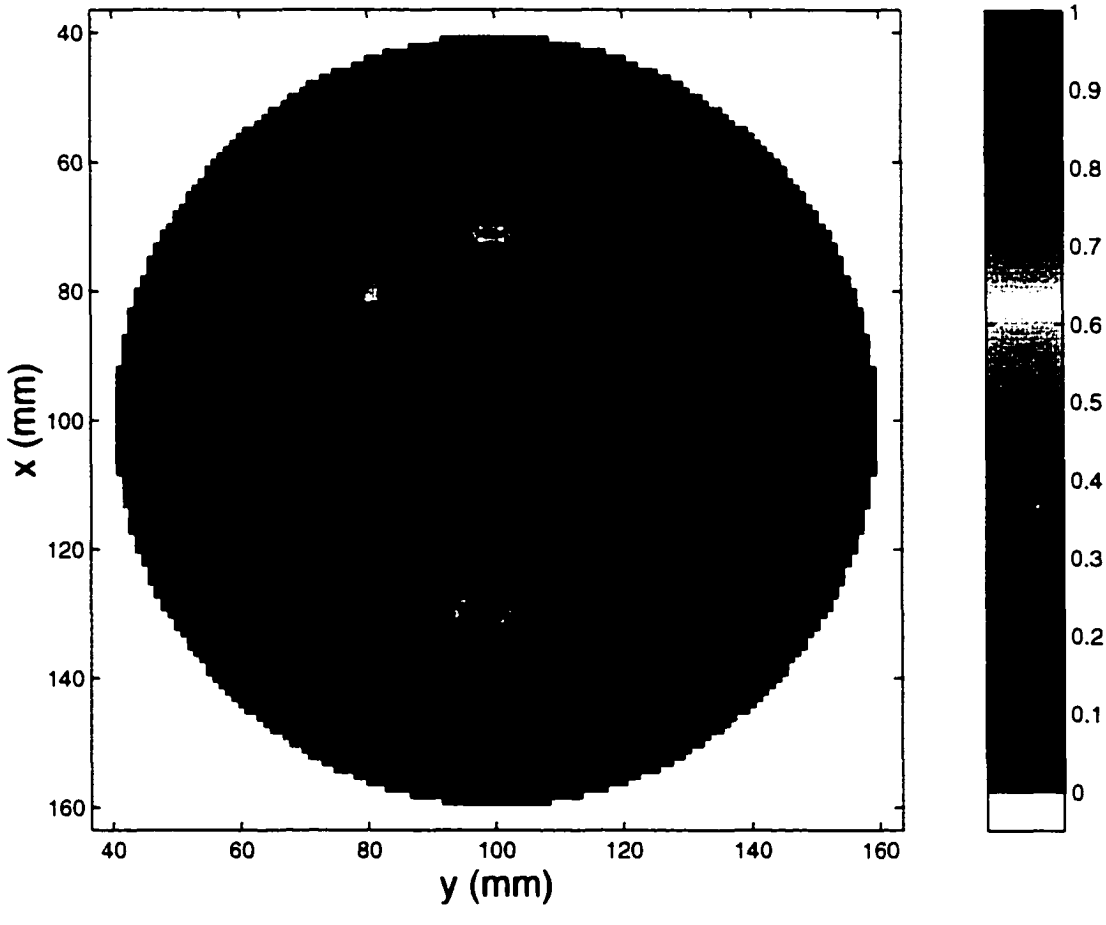

Figure 5-39 Image of 6-mm diameter tumor embedded in realistic breast model. Images are formed with 20 antennas located 1 cm from the breast and at the same "height" (z location) as the tumor. Image reconstruction involves calibration, averaging skin subtraction, correlation and modified compensation.

5.2.5 Multiple antennas

Results for the more realistic breast model demonstrate the need for multiple antennas for reduced data acquisition time. In Chapter 4, the feasibility of placing up to 4 antennas in an array was investigated. With multiple antennas present, one antenna transmits a pulse and the returns are recorded at the same antenna, as well as at the other non-active antenna elements. Data acquisition time is reduced because less physical translation of elements is required. Additionally, information recorded at the non-excited elements may be useful for image reconstruction.

For the antennas investigated without a breast model present, results indicated that, with sufficient spacing between elements, time gating should eliminate the influence of multiple antennas in data collection. In this section, the behaviour of multiple antennas with a breast model present is investigated. The first step is calibration: voltages recorded with one and four antennas present are compared to determine an appropriate time gate. The results from Chapter 4 indicate that a time gate of 2750 time steps is appropriate. That is, signals recorded after time step 2750 are neglected. Voltages recorded with the breast model present are compared with one and four antennas present. Figure 5-40 shows the difference voltage over the time window. For reference, the peak-to-peak response of a 6 mm diameter tumor at 3 cm depth is more than 5000 times the peak-to-peak voltage difference. Therefore, applying a time gate to the recorded voltage appears to reduce the influence of additional antennas. In this example, the maximum extent of the interrogated region is only 5 cm into the breast after time gating. This may have implications for increased spatial sampling in order to provide reliable tumor detection. For example, assume that data from half the number of antennas is available at each focal point. Twice as many antenna locations are then required to obtain comparable signal-to-clutter ratios. Time gating and sufficient spacing also have implications for the maximum number of antennas that may be present in an array. While up to 30 antennas spaced by 1 cm are used earlier in the chapter for image reconstruction, an array of only 4 elements is examined here. With 30 elements present, the radiated pulse would be re-radiated by the neighbouring antennas and propagate back to the excited antenna. While this initial re-radiated signal may be calibrated out, it is

much more difficult to deal with reflections from the breast due to the re-radiated signals in this manner. As the breast-antenna separation is 1 cm, no reliable data is recorded from the breast. With larger antenna spacing, more reliable data is recorded from the breast. Thus, without coding the transmitted signal, the antenna spacing must allow for reception of information at a sufficient penetration depth. Even with an array of four antennas, the data acquisition time is decreased by a factor of approximately four. Finally, information is also available from the voltages recorded at other antennas. This may be useful for skin location or forming complementary images with transmitted data.

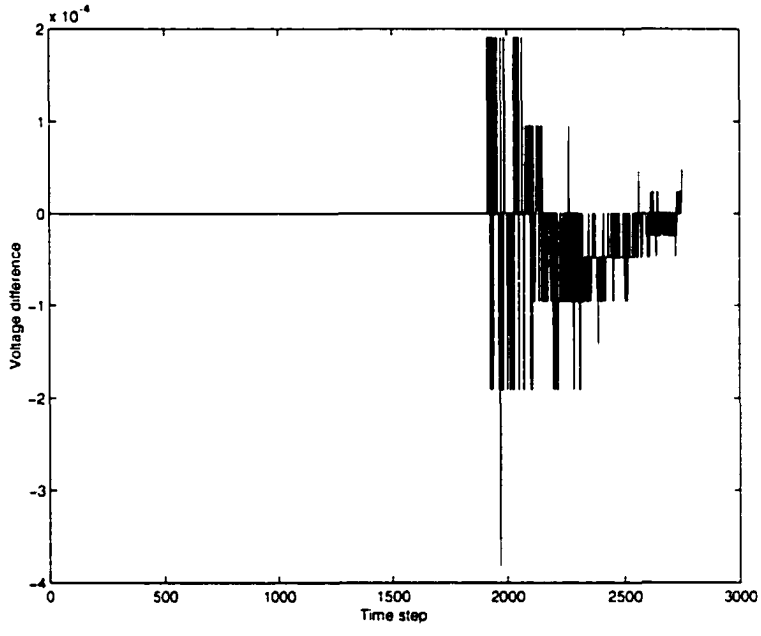

Figure 5-40 Difference in voltages recorded with 1 or 4 antennas and breast model present.

5.2.6 Preliminary safety assessment

One of the benefits of CMI for breast imaging is the anticipated minimal health impact. One method of assessing the safety of exposure to RF devices involves determining the specific absorption rate (SAR). According to IEEE Standard C95.1-1991, peak spatial SAR of less than 1.6 W/kg averaged over any 1 g of tissue is permitted in uncontrolled environments [135]. The SAR distribution for breast model 4 is computed with FDTD and routines developed for computing SAR [136]. The peak spatial value of SAR at 3.75 GHz (near the maximum frequency content of the signal) is 32 W/kg with 1 g tissue

averaging and normalized to 1 W total power. This peak value is located in the skin near the antenna. As a worst-case approximation, the maximum total SAR due to the wideband pulse is calculated by multiplying 32 W/kg by 5×10^9 (to represent contributions over the frequency range), then 0.3 ns (to represent the pulse duration), and divided by the 6-minute averaging time. The result is 0.13 W/kg, which is below the 1.6 W/kg set by the standard. It is emphasized that this is a worst-case approximation, as the maximum SAR at frequencies lower and higher than 3.75 GHz is expected to be much lower than 32 W/kg (due to reduced power at these frequencies in the excitation pulse). Additionally, the total power radiated is expected to be less than 1 W (here, the total power radiated at 3.75 GHz is 1 W). Thus, it is expected that CMI will be within safety limits, even with the use of multiple pulses required for data acquisition in a reasonable time frame.

5.3 Summary

In this chapter, the antennas selected in Chapter 4 are applied to the imaging task. Simulations of the antennas illuminating simple breast models are performed with the finite difference time domain method. The returns recorded from the breast models are used to reconstruct images by applying signal processing algorithms. Calibration involves subtraction of returns recorded without a breast model present. Skin subtraction reduces dominant reflections from the thin layer of skin. Return enhancement aims to selectively enhance tumor returns. Compensation corrects for decreases in returns due to wave expansion and propagation through lossy media. The processed signals are then synthetically focussed at points of interest in the domain to form an image. The results presented in this chapter indicate that each signal processing step plays an essential role in tumor detection and localization in 3D. The final algorithms are capable of detecting and localizing 6-mm diameter tumors at depths of 3 cm in cylindrical breast models immersed in liquid 1 or 2 and illuminated with the appropriate antenna. A comparison of results obtained with a planar CMI system indicates that similar signal-to-clutter ratios are achieved with both cylindrical and planar systems. Therefore, the cylindrical CMI system presented in this thesis is not only capable of detecting and localizing tumors, it also has similar performance to the previously introduced planar system. Results in this

chapter also demonstrate that the cylindrical system appears capable of tumor detection with more realistic breast models, as well as data acquisition with multiple antennas. Finally, a preliminary evaluation of the specific absorption rate suggests that the cylindrical CMI system will be well within safety limits.

6 Conclusions

The main contribution of this thesis is the development of a new configuration for confocal microwave imaging for breast tumor detection. The objectives of the research were to design a system:

- without physical contact of antennas and the patient,
- incorporating small antennas,
- with the location of antennas determined before the scan to provide a frame of reference for ease of image reconstruction, and
- having the capability to detect and localize small tumors at reasonable depths.

The cylindrical CMI system investigated in this thesis meets all of the design goals. Four antenna designs, each of length less than 1.5 cm, are evaluated with measures appropriate for the ultra-wideband signal and the imaging application. By placing the selected antenna at a distance from the skin, no direct contact is made with the patient. Further, the locations of the antennas can be determined prior to the scan, as no contact with the patient is required except through the immersion liquid. Although the antenna-skin separation results in significant reflections from the skin, these reflections are successfully dealt with using the signal processing techniques developed in this research. The signal processing and image reconstruction methods also allow for the detection and 3D localization of tumor responses, as demonstrated in a simple cylindrical breast model. The algorithms are further tested with a more realistic hemispherical breast model that includes glands, a chest wall, and nipple, resulting in successful detection and localization of the tumor in a 2D cross-section. As a larger and more realistic breast model demands data acquisition at an increasing number of points, the feasibility of collecting data with sufficiently spaced multiple antennas is demonstrated.

In addition to successfully meeting the objectives stated above, the cylindrical CMI configuration is shown to have tumor detection capabilities similar to those achieved with the planar CMI configuration. Additionally, the cylindrical system appears to be better

suited for clinical implementation, as suggested by respected researchers in microwave breast imaging [113].

Future research involves further feasibility studies with simulated data, as well as experimental work. First, it is expected that collecting data with a conical 3D array will allow for the detection and localization in 3D of tumors in the realistic breast model. Simulations are being performed to test this hypothesis. Additional computational studies may be performed with increasingly realistic breast models. Of particular interest is a realistic breast model constructed with magnetic resonance imaging scans and incorporating results from measurements of excised tissue at the University of Calgary and the University of Wisconsin-Madison. However, the most crucial work is experimental verification of CMI. The first step is expected to be a project involving equipment currently available in the BioElec laboratory at the University of Victoria, and focusing on the development of a system for positioning the antennas. Following this, fabrication of sensors and development of appropriate phantoms for testing image reconstruction algorithms is anticipated.

With further rapid development and success, clinical trials of CMI for breast tumor detection are possible within 5 years. Ultimately, it is hoped that the research presented here will contribute to providing women with a non-invasive and comfortable imaging technology that quickly gives definitive answers about the status of abnormal mammograms.

Bibliography

1. National Cancer Institute of Canada, *Canadian Cancer Statistics 1999*, Toronto, Canada, 1999.

2. C.H. Jones, "Methods of breast imaging", *Phys. Med. Biol.*, vol. 27, 1982, pp. 463-499.

3. Margaret C. Neville and Marianne R. Neifert, eds. *Lactation: Physiology, Nutrition and Breast-Feeding*, Plenum Press, New York, 1983.

4. P.S. Rudland, D.G. Fernig, S. Leinster and G.G. Lunt, *Mammary Development and Cancer*, Portland Press, London, 1998.

5. Cancer Information Database, BC Cancer Agency, www.bccancer.bc.ca.

6. M. Sabel and H. Aidringer, "Recent developments in breast imaging", *Phys. Med. Biol.*, vol. 41, 1996, pp. 315-368.

7. E.D. Pisana, E.B. Cole, B.M. Hemminger, M.J, Yaffe, S.R. Aylward, A.D.A. Maidment, R.E. Johnston, M.B. Williams, L.T. Niklason, E.F. Conant, L.L. Fajardo, D.B. Kopans, M.E. Brown, S.M. Pizer, "Image processing algorithms for digital mammography: a pictoral essay", *RadioGraphics*, vol. 20, 2000, pp. 1479-1491.

8. D. Paquette, J. Snider, F. Bouchard, I. Olivotto, H. Bryant, K. Decker, G. Doyle, "Performance of screening mammography in organized programs in Canada in 1996," *CMAJ*, vol. 163 (9), 2000, pp. 1133-8.

9. I. Olivotto, L. Kan, S. King, "Waiting for a diagnosis after an abnormal screening mammogram," *Canadian Journal of Public Health*, vol. 91 (2), 2000 , pp. 113-117,

10. R.M. Rangayyan, N.M. El-Faramawy, J.E. Desautels and O.A. Alim, "Measures of acutance and shape for classification of breast tumors", *IEEE Transac. Med. Imaging*, vol. 16, Dec. 1997, pp. 799-810.

11. H. Azhari and D. Sazbon, "Volumetric imaging with ultrasonic spiral CT", *Radiology*, vol. 212 (1), July 1999, pp. 270-275.

12. C.W. Manry, Jr. and S.L. Broschat, "Inverse imaging of the breast with a material classification technique", *J. Acoustic Soc. Am.* vol. 103 (3), March 1998, pp. 1538-1546.

13. B.F. Jones, "A reappraisal of the use of infrared thermal image analysis in medicine," *IEEE Transac. Med. Imaging*, vol. 17 (6), December 1998, pp. 1019-1027.

14. B.W. Pogue, M. Testorf, T. McBride, U. Osterberg, K. Paulsen, "Instrumentation and design of a frequency-domain diffuse optical tomography images for breast cancer

detection", *Optics Express*, vol. 1 (13), Dec. 1997, pp. 391-403.

15. B.D. Sollish, E.H. Frei, E. Hammerman, S.B. Lang and M. Moshitzky, "Microprocessor-assisted screening techniques," *Israel J. Med. Sci.*, vol. 17, Sept-Oct. 1981, pp. 859-864.

16. M. Melloul, A. Paz, G. Ohana, O. Laver, D. Michalevich, R. Koren, Y. Wolloch, and R. Gal, "Double-phase ^{99m}Tc-Sestamibi scintimammography and Trans-Scan in diagnosing breast cancer," *J. Nuclear Medicine*, vol. 40 (3), March 1999, pp. 376-380.

17. E.D. Pisano and C.A. Parham, "Digital mammography, sestamibi breast scintigraphy, and positron emission tomography breast imaging," *Radiologic Clinics of North America*, vol. 38 (4), July 2000, pp. 861-869.

18. D.C. Barber, "Electrical Impedance Tomography," *Handbook of Biomedical Engineering*, CRC Press, Boca Raton, 1995, pp. 1151-1164.

19. J.L. Mueller, D. Isaacson and J.C. Newell, "A reconstruction algorithm for electrical impedance tomography data collected on rectangular electrode arrays," *IEEE Transac. Biomed. Eng.*, vol. 46, Nov. 1999, pp. 1379-1386.

20. A. Hartov et al, "A multichannel continuously selectable multifrequency electrical impedance spectroscopy measurement system," *IEEE Trans. Biomed. Eng.*, vol. 47, Jan. 2000, pp. 49-58.

21. K.S. Osterman, T.E. Kerner, D.B. Williams, A. Hartov, S.P. Poplack and K.D. Paulsen, "Multifrequency electrical impedance imaging: preliminary in vivo experience in breast", *Physiol. Meas.*, vol. 21, 2000, pp. 99-109.

22. K.R. Foster and H.P. Schwan, "Dielectric properties of tissues", *Handbook of Biological Effects of Electromagnetic Fields*, eds. C. Polk and E. Postow, CRC Press, Boca Raton, 1996, pp. 25-102.

23. S. Gabriel et al, "The dielectric properties of biological tissues: II. Measurements in the frequency range 10 Hz to 20 GHz", *Phys. Med. Biol.*, vol. 41, 1996, pp. 2251-2269.

24. S. Gabriel et al, "The dielectric properties of biological tissues: III. Parametric models for dielectric spectra of tissues", *Phys. Med. Biol.*, vol. 41, 1996, pp. 2271-2293.

25. K.R. Foster and J.L. Schepps, "Dielectric properties of tumor and normal tissues at radio through microwave frequencies", *J. Microwave Power*, vol. 16, 1981, p.107.

26. R. Pelso et al, "Dielectric properties of solid tumors during normothermia and hyperthermia", *IEEE Transac. Biomed. Eng.*, vol. 31, pp. 725-728.

27. J.A. Rogers et al, "The dielectric properties of normal and tumor mouse tissue between 50 MHz and 10 GHz", *British J. Radiology*, vol. 56, 1983, pp. 335-338.

28. W.T. Joines et al, "The measured electrical properties of normal and malignant human tissues from 50 to 900 MHz", *Med. Phys.*, vol. 21, 1994, pp. 547-550.

29. H. Fricke and S. Morse, "The electrical capacity of tumors of the breast," *J. Cancer Research*, vol. 16, 1926, pp. 310-376.

30. J. Nuutinen, T. Lahtinen, M. Turunen, E. Alanen, M. Tenhunen, T. Usenius and R. Kolle, "A dielectric method for measuring early and late reactions in irradiated human skin", *Radiotherapy and Oncology*, vol. 47, 1998, pp. 249-254.

31. T.S. England and N. A. Sharples, "Dielectric properties of the human body in the microwave region of the spectrum", *Nature*, vol. 163, 1949, pp. 487-488.

32. T.S. England, "Dielectric properties of the human body for wave lengths in the 1-10 cm range", *Nature*, vol. 166, 1950, pp. 480-481.

33. J.R. Mallard and D.G. Lawn, "Dielectric absorption of microwaves in human tissues," *Nature*, vol. 213, 1967, pp. 28-30.

34. T. Morimoto et al, "Measurement of the electrical bio-impedance of breast tumors", *Eur. Surg. Res.*, vol. 22, 1990, pp. 86-92.

35. A. A. Mario et al, "Electrical potential measurements in human breast cancer and benign lesions," *Tumor Biology*, 15, 1194, pp. 147-152.

36. N. Chauveau, "Ex vivo discrimination between normal and pathological tissues in human breast surgical biopsies using bioimpedance spectroscopy," *Annals of the New York Academy of Sciences*, 1999, pp. 42-50.

37. J. Jossinet, "The impedivity of freshly excised human breast tissue", *Physiol. Meas.* vol. 19, 1998, pp. 61-75.

38. A. J. Surowiec, S.S. Stuchly, J.B. Barr, and A. Swarup , "Dielectric properties of breast carcinoma and the surrounding tissues", *IEEE Transac. Biomed. Eng.*, vol. 31 (4), 1988, pp. 257-263.

39. S.S. Chaudhary, R.K. Mishra, A. Swarup and J.M. Thomas, "Dielectric properties of normal and malignant human breast tissues at radiowave and microwave frequencies", *Indian J. Biochem. and Biophys.*, vol. 21, Feb. 1984, pp. 76-79.

40. A. M. Campbell and D.V. Land, "Dielectric properties of female human breast tissues measured in vitro at 3.2 GHz", *Phys, Med. Biol.*, vol. 37 (1), 1992, pp. 193-210.

41. S.C. Hagness, A. Taflove and J.E. Bridges, "Two-dimensional FDTD analysis of a pulsed microwave confocal system for breast cancer detection: fixed-focus and

antenna-array sensors", *IEEE Transac. Biomed. Eng.*, vol. 45, Dec 1998, pp. 1470-1479.

42. K. Leininger, X. Li, S.C. Hagness, "Microwave discrimination between malignant and benign breast tumors: a computational and experimental feasibility study," *USNC/URSI National Radio Science Meeting 2000 Digest*, 2000, p. 154.

43. M. Miyakawa, "Tomographic measurement of temperature change in phantoms of the human body by chirp radar-type microwave computed tomography", *Med. Biol. Eng. Comput.*, vol. 31, 1993, S31-S36.

44. K.D. Paulsen and P.M. Meaney, "Nonactive antenna compensation for fixed-array microwave imaging: Part I—Model development", *IEEE Transac. Med. Imaging*, vol. 18, June 1999, pp. 496-507.

45. P.M. Meaney, K.D. Paulsen, M.W. Fanning, A. Hartov, "Nonactive antenna compensation for fixed-array microwave imaging: Part II--Imaging results", *IEEE Transac. Med. Imaging*, vol. 18, June 1999, pp. 508-18.

46. R.A. Kruger, K.K. Kopecky, A.M Aisen, D.R. Reinecke, G.A. Kruger and W.L. Kiser, Jr., "Thermoacoustic CT with radio waves: a medical imaging paradigm," *Radiology*, April 1999, pp. 275-278.

47. R. A. Kruger, W.L. Kiser, Jr., D.R. Reinecke, G.A Kruger, R.L. Eisenhart, "Thermoacoustic computed tomography of the breast at 434 MHz", *IEEE MTT-S International Microwave Symposium Digest*, 1999, pp. 591-594.

48. S.C. Hagness, A. Taflove and J.E. Bridges, "Three-dimensional FDTD analysis of pulsed microwave confocal system for breast cancer detection: design of an antenna-array element", *Transac. Antennas Propag.*, vol. 47, May 1999, pp. 783-791.

49. M. Slaney, M. Azimi, A.C. Kak, and L.E. Larsen, "Microwave imaging with first order diffraction tomography," in *Medical Applications of Microwave Imaging*, L.E. Larsen and J.H. Jacobi, eds., IEEE Press, New York, 1986.

50. W.C. Chew, "Imaging and inverse problems in electromagnetics," *in Advances in Computational Electrodynamics*, A. Taflove, ed. Artech House, Boston, 1998.

51. L.E. Larsen and J.H. Jacobi, "Methods of active microwave imagery for dosimetric applications" in *Medical Applications of Microwave Imaging*, L.E. Larsen and J.H. Jacobi, eds., IEEE Press, New York, 1986.

52. T.C. Guo, W.W. Guo and L.E. Larsen, "Recent developments in microwave medical imagery: phase and amplitude conjugations and the inverse scattering theorem" in *Medical Applications of Microwave Imaging*, L.E. Larsen and J.H. Jacobi, eds., IEEE Press, New York, 1986.

53. T.C. Guo, W.W. Guo and H.N. Oguz, "A technique for three-dimensional dosimetry

and scattering computation of vector electromagnetic fields" *IEEE Trans. Magnetics,* vol. 29 (2), March 1993, pp. 1636-1641.

54. T.C. Guo and W.W. Guo, "High resolution microwave imaging simulation of a human neck", *IEEE Instrumentation and Measurement Technology Conference*, vol. 3, 1999, pp.1586-1590.

55. *Medical Applications of Microwave Imaging,* L.E. Larsen and J.H. Jacobi, eds., IEEE Press, New York, 1986.

56. C. Pichot, L. Jofre, G. Peronnet and J.-C. Bolomey, "Active Microwave imaging of inhomogeneous bodies", *IEEE Transac. Antenna Propag.*, vol. AP-33 (4), April 1985, pp. 416-425.

57. L. Jofre, M.S. Hawley, A. Broquetas, E. de los Reyes, M. Ferrando, and A.R. Elias-Fuste, "Medical imaging with a microwave tomographic scanner", *IEEE Transac. Biomed. Eng.*, vol. 37 (3), March 1990, pp. 303-312.

58. A. Broquestas, J. Romeau, J.M Rius, A.R. Elias-Fuste, A. Cardama, and L. Jofre, "Cylindrical geometry: a further step in active microwave tomography", *IEEE Microwave Theory Tech.*, vol. 39 (5), May 1991, pp. 836-844.

59. J.M. Rius, C. Pichot, L. Jofre, J.C. Bolomey, N. Joachimowicz, A. Broquestas, and M. Ferrando, "Planar and Cylindrical active microwave temperature imaging: numerical simulations", *IEEE Transac. Med. Imaging,* vol. 11 (4), Dec. 1992, pp. 457-469.

60. A. Franchois, A. Joisel, C. Pichot, and J.-C. Bolomey, "Quantitative microwave imaging with a 2.45-GHz planar microwave camera", *IEEE Transac. Med. Imaging*, vol. 17, (4), Aug. 1998, pp. 550-561.

61. N. Joachimowicz, J.J. Mallorqui, J.-C. Bolomey, and A. Broquestas, "convergence and stability assessment of Newton-Kantorovich reconstruction algorithms for microwave tomography", *IEEE Transac. Med. Imaging*, vol. 17, (4), Aug. 1998, pp. 562-570.

62. S. Caorsi, A. Frattoni, G.L. Gragnani, E. Nortino, M. Pastorino, "Numerical algorithm for dielectric-permittivity microwave imaging of inhomogeneous biological bodies", *Med. Biol. Eng. and Comput.*, vol. 29, 1991, NS37-NS44.

63. S. Caorsi, G.L. Gragnani, M. Pastorino, "A multiview microwave imaging system for two-dimensional penetrable objects", *IEEE Transac. Microw. Theory Tech.*, vol. 39 (5), May 1991, pp. 845-850.

64. S. Caorsi, G.L. Gragnani, M. Pastorino, "Reconstruction of dielectric permittivity distributions in arbitrary 2-D inhomogeneous biological bodies by a multiview microwave numerical method", *IEEE Transac. Med. Imaging*, vol. 12 (2), 1993, pp. 232-239.

65. S. Caorsi, G.L. Gragnani, and M. Pastorino, "Redundant electromagnetic data for microwave imaging of three-dimensional dielectric objects", *IEEE Transac. Antenna Propag.*, vol. 42 (5), May 1994, pp. 581-589.

66. S. Caorsi, G. L. Gragnani, M. Pastorino, "An electromagnetic imaging approach using a multi-illumination technique", *IEEE Transac. Biomed. Eng.*, vol. 41 (4), April 1994, pp. 406-409.

67. S. Caorsi, G.L. Gragnani, M. Pastorino and M. Rebaliati, "A model-driven approach to microwave diagnostics in biomedical applications", *IEEE Transac. Microw. Theory Tech.*, v. 44, (10), Oct. 1996, pp. 1910-1920.

68. S. Caorsi, A. Ferrando, G.L . Gragnani, and M. Pastorino, "A moment-method-based approach to electromagnetic scattering computation by a perturbation technique", *IEEE Transac. Antenna Propag.*, vol. 24, (10), Oct. 1997, pp. 1561-1563.

69. S. Caorsi, G.L. Gragnani, S. Medicina, M. Pastorino, and G.A. Pinto, "A Gibbs random field-based electromagnetic method for noninvasive diagnostics in biomedical applications", *Radio Science*, vol. 30 (1), Jan.-Feb 1995, pp. 291-301.

70. M. Pastorino and S. Caorsi, "A microwave inverse scattering technique for image reconstruction based on a genetic algorithm" *1999 IEEE Instrumentation and Measurement Conference*, 1999, pp. 118-123

71. P.M. Meaney, K.D. Paulsen and T.P. Ryan, "Two-dimensional hybrid element image reconstruction for TM illumination", *IEEE Transac. Antenna Propag.*, March 1995, vol. 43 (3), pp. 239-247.

72. P.M. Meaney, K.D. Paulsen, A. Hartov, and R.K. Crane, "An active microwave imaging system for reconstruction of 2-D electrical property distributions", *IEEE Transac. Biomed. Eng.*, vol. 42 (10), Oct 1995, pp. 1017-1026.

73. P.M. Meaney, K.D. Paulsen, J.T. Chang, "Near-field microwave imaging of biologically-based materials using a monopole transceiver system", *IEEE Transac. Microw. Theory Tech.*, vol. 46 (1), Jan. 1998, pp. 31-45.

74. K. D. Paulsen, P.M. Meaney, M.J. Moskowitz, and J.M. Sullivan, Jr., "A dual mesh scheme for finite element based reconstruction algorithms", *IEEE Transac. Med. Imaging*, vol. 14 (3), Sept. 1995, pp. 504-514.

75. S.Y. Semenov, R.H. Svenson, A.E Boulyshev, A.E. Souvorov, V.Y. Borisov, Y. Sizov, A.N. Starostin, K.R Dezern, G.P. Tatsis, and V.Y. Baranov, "Microwave tomography: two-dimensional system for biological imaging", *IEEE Transac. Biomed. Eng.*, vol. 43, #9, Sept. 1996, pp. 869-877.

76. A.E. Souvorov, A.E Bulyshev, S.Y. Semenov, R.H. Svenson, A.G. Nazarov, Y. Sizov and G.P. Tatsis, "Microwave tomography: a two-dimensional Newton iterative scheme", *IEEE Transac. Microw. Theory Tech.*, vol. 46, #11, Nov. 1998, pp. 1654-

1658.

77. S.Y. Semenov, A.E Bulyshev, A.E. Souvorov, R.H. Svenson, Y. Sizov, V.Y. Borisov, V.G. Posukh, I.M. Kozlov, A.G. Nazarov and G.P. Tatsis "Microwave tomography: theoretical and experimental investigation of the iteration reconstruction algorithm", *IEEE Transac. Microw. Theory Tech.*, vol. 46, #2, Feb. 1998, pp. 133-141.

78. S.Y. Semenov, R.H. Svenson, A.E Bulyshev, A.E. Souvorov, A.G. Nazarov, Y. Sizov, A. Pavlovsky, V.Y. Borisov, B.A. Voinov, G.I. Simonova, A.N. Starostin V.G. Posukh, G.P. Tatsis, and V.Y. Baranov, "Three-dimensional microwave tomography: experimental prototype of the system and vector Born reconstruction method", *IEEE Transac. Biomed. Eng.*, vol. 46, #8, Aug. 1999, pp. 937-946.

79. A.E. Souvorov, A.E Bulyshev, S.Y. Semenov, R.H. Svenson and G.P. Tatsis, "Two-dimensional analysis of a microwave flat antenna array for breast cancer tomography," *IEEE Transac. Microw. Theory Tech.*, vol. 48, Aug. 2000, pp. 1413-1415.

80. F.-C. Chen and W.C. Chew, "Time-domain ultra-wideband microwave imaging radar system", *IEEE Instrumentation and measurement technology conference*, 1998, pp. 648-650.

81. G.P. Otto and W.C. Chew, "Microwave inverse scattering – local shape function imaging for improved resolution of strong scatterers", *IEEE Transac. Microw. Theory Tech.*, vol. 42, #1, Jan. 1994, pp. 137-141.

82. J.D. Young and L. Peters Jr., "Examination of video pulse radar systems as potential biological exploratory tools" in *Medical Applications of Microwave Imaging*, L.E. Larsen and J.H. Jacobi, eds., IEEE Press, New York, 1986.

83. J.H. Jacobi and L.E. Larsen, "Linear FM pulse compression radar techniques applied to biological imaging" in *Medical Applications of Microwave Imaging*, L.E. Larsen and J.H. Jacobi, eds., IEEE Press, New York, 1986

84. M. Popovic, S.C. Hagness, A. Taflove and J.E. Bridges, "2-D FDTD study of fixed-focus elliptical reflector system for breast cancer detection: Frequency window for optimum operation", *IEEE Antennas and Propagation Symposium Digest*, v.4, Jun 21-26 1998, p 1992-1995.

85. S.C. Hagness, A. Taflove and J.E. Bridges, "Wideband ultralow reverberation antenna for biological sensing", *Elec. Lett.*, v. 33, Sept. 11 1997, pp. 1594-1595.

86. S.C. Hagness, X. Li, E.C. Fear, and M.A. Stuchly, "Numerical Investigation of Two Confocal Microwave Imaging Systems for Breast Tumor Detection", *16th anuual review of progress in applied computational eletromagnetics: conference proceedings*, March 2000, p. 310-316.

87. H.F. Engler, Jr., "Technical issues in ultra-wideband radar systems," in *Introduction*

to Ultra-wideband Radar Systems, ed. J.D. Taylor, CRC Press, Boca Raton, 1995, pp. 11-50.

88. P.R. Foster, "Antennas and UWB Signals", in *Introduction to Ultra-wideband Radar Systems*, ed. J.D. Taylor, CRC Press, Boca Raton, 1995, pp. 147-216.

89. D. Lamensdorf and L. Susman, "Baseband-Pulse-Antenna Techniques", *IEEE Antennas Propag. Magazine,* vol. 36, Feb. 1994, pp. 20-30.

90. J.G. Maloney and G. S. Smith, "A study of transient radiation from the Wu-King resistive monopole – FDTD analysis and experimental measurements," *IEEE Transac. Antennas Propag.*, vol. 41, May 1993, pp. 668-678.

91. T. Montoya and G.S. Smith, "A study of pulse radiation from several broad-band loaded monopoles", *IEEE Transac. Antennas Propag.*, vol. 41, Aug. 1996, pp. 1172-1182.

92. T. Montoya and G.S. Smith, "Vee dipoles with resistive loading for short-pulse ground-penetrating radar", *Microw. Optical Tech. Lett.*, vol. 13, Oct. 20 1996, pp. 132-137.

93. T. Montoya and G.S. Smith, "Land mine detection using a ground-penetrating radar based on resistively loaded vee dipoles", *IEEE Transac. Antennas Propag.*, vol. 47, Dec. 1999, pp. 1795-1806.

94. J.G. Maloney and G.S. Smith, "Optimization of a conical antenna for pulse radiation: an efficient design using resistive loading", *IEEE Transac. Antennas Propag.*, vol. 41, July 1993, pp. 940-947.

95. K.L Shlager, G.S. Smith, J.G. Maloney, "Optimization of bow-tie antennas for pulse radiation", *IEEE Transac. Antennas Propag.*, v. 42, July 1994, pp. 975-982.

96. J.M. Bourgeois and G.S. Smith, "A fully three-dimensional simulation of a ground penetrating radar: FDTD theory compared with experiment", *IEEE Transac. Geoscience and Remote Sensing,* vol. 34, Jan.1996, pp. 36-44.

97. J.D. Taylor and E.C. Kisenwether, "Ultra-wideband Radar Receivers" in *Introduction to Ultra-wideband Radar Systems*, ed. J.D. Taylor, CRC Press, Boca Raton, 1995, pp. 491-577.

98. E.M. Johansson and J.E. Mast, "Three-dimensional ground penetrating radar imaging using synthetic aperture time-domain focusing", *Proceedings of SPIE,* vol. 2275, 1994, pp. 205-214.

99. J.I. Halman, K.A. Shubert and G.T. Ruck, "SAR processing of ground-penetrating radar data for buried UXO detection: results from surface-based system", *IEEE Transac. Antenna Propag.*, vol. 46, July 1998, pp. 1023-1027.

100. L.C. Carin, N. Geng, M. McClure, J. Sichina, and L. Nguyen, "Ultra-wide-band synthetic-aperture radar for mine-field detection", *IEEE Antennas and Propag. Magazine*, vol. 41, Feb. 1999, pp. 18-33.

101. A.L. Warrick, S.G. Azevedo and J.E. Mast, "Prediction of buried mine-like target radar signatures using wideband electromagnetic modeling", *Proceedings of SPIE*, vol. 3392, 1998, pp. 776-783.

102. C.-C. Chen, "Electromagnetic resonances of immersed dielectric spheres", *IEEE Transac. Antennas Propag.*, vol. 46, July 1998, pp. 1074-1083.

103. T.T. Wu and R.W.P. King, "The cylindrical antenna with nonreflective resistive loading," *IEEE Transac. Antennas Propag.* vol. 13, May 1965, pp. 369-373 and correction by L.C. Shen and R.W.P. King in same vol., Nov. 1965, p. 998.

104. M. Kanda, "Time domain sensors for radiated impulsive measurements", *IEEE Transac. Antennas Propag.* vol. 31, May 1983, pp. 438-444.

105. K. Esselle and S.S. Stuchly, "Pulse receiving characteristics of resistively loaded dipole antennas", *IEEE Transac. Antennas and Propag.*, vol. 38, Oct. 1990, pp. 1677-1683.

106. J. Berenger, "A perfectly matched layer for the absorption of electromagnetic waves", *Journal of Computational Physics*, vol. 114, 1994, pp. 185-200.

107. K. Thomas, *LC User's Guide, version 2.7*, 10 Feb. 1999, http://lc.cray.com.

108. M. Okoniewski and M.A. Stuchly, "Study of the handset antenna and human body interaction", *IEEE Transac. Microw. Theory Tech.*, v. 44, Oct. 1996, p. 1855-1864.

109. O.E. Allen, D.A. Hill and A.R. Ondrejka, "Time-domain antenna characterizations", *IEEE Transac. Electromag. Compat.*, vol. 35, Aug. 1993, pp. 339-345.

110. E. Kreyszig, *Advanced engineering mathematics*, New York:Wiley, 1988.

111. L.V. Wang, X. Zhao, H. Sun and G. Ku, "Microwave-induced acoustic imaging of biological tissues," *Review of Scientific Instruments*, vol. 70 (9), Sept. 1999, pp. 3744-3748.

112. G. Ku and L.V. Wang, "Scanning thermoacoustic tomography in biological tissue," *Med. Phys.*, vol. 27(5) May 2000, pp. 1195-1202.

113. P.M. Meaney, M.W. Fanning, D. Li, S. P. Poplack, and K.D Paulsen, "A clinical prototype for active microwave imaging of the breast," *IEEE Transac. Microw. Theory Tech.*, vol. Nov 2000, pp. 1841-1853.

114. E.C. Fear, X. Li, S.C. Hagness, and M.A. Stuchly, "Confocal microwave imaging for breast cancer detection: localization of tumors in three dimensions", submitted *to*

IEEE Trans. Medical Imaging, March 2001.

115. X. Li and S.C. Hagness, "A confocal microwave imaging algorithm for breast cancer detection," *IEEE Microwave and Wireless Components Letters*, March 2001 (in press).

116. S. Caorsi, A. Massa, and M. Pastorino, "Numerical assessment concerning a focused microwave diagnostic method for medical applications," *IEEE Transac. Microw. Theory Tech.*, vol. 48 (11), Nov. 2000, pp. 1815-1830.

117. T.A Maniatis, K.S. Nikita, and N.K. Uzunoglu, "Two-dimensional dielectric profile reconstruction based on spectral-domain moment method and nonlinear optimization", *IEEE Transac. Microw. Theory Tech.*, 48 (11), Nov. 2000, pp. 1831-1840.

118. A. Joisel and J.C. Bolomey, "Rapid microwave imaging of living tissues", *Proceedings of SPIE*, vol. 3977, 2000, pp. 320-329.

119. P.M. Meaney, K.D. Paulsen and M.W. Fanning, "Microwave imaging for breast cancer detection: preliminary experience," *Proceedings of SPIE*, vol. 3977, 2000, pp. 308-319.

120. J.T. Chang, M.W. Fanning, P.M. Meaney and K.D. Paulsen, "A conductive plastic for simulating biological tissue at microwave frequencies", *IEEE Trans. Electromag. Compatibility, vol.* 42 (1), Feb. 2000, pp. 76-81.

121. S.Y. Semenov, A.E. Bulyshev, A.E. Souvorov, A.G. Nazarov, Y.E. Sizov, R.H. Svenson, V.G. Posukh, A. Pavlovsky, P.N. Repin, and G.P. Tatsis, "Three-dimensional microwave tomography: experimental imaging of phantoms and biological objects," *IEEE Transac. Microw. Theory Tech.*, vol. 48 (6), June 2000, pp. 1071-1074.

122. S.Y. Semenov, R.H. Svenson, A.E. Bulyshev, A.E. Souvorov, A.G. Nazarov, Y.E. Sizov, V.G. Posukh, A. V. Pavlovsky, P.N. Repin and G.P. Tatsis, "Spatial resolution of microwave tomography for detection of myocardial ischemia and infarction – experimental study on two-dimensional models", *IEEE Transac. Microw. Theory Tech.*, vol. 48 (4), April 2000, pp. 538-544.

123. A. E. Souvorov, A.E. Bulyshev, S.Y. Semenov, R.H. Svenson and G. P. Tatsis, "Two-dimensional computer analysis of a microwave flat antenna array for breast cancer tomography", *IEEE Transac. Microw. Theory Tech.*, vol. 48 (8), Aug. 2000, pp. 1413-1415.

124. M. Bertero, M. Miyakawa, P. Boccacci, F. Conte, K. Orikasa and M. Furutani, "Image restoration in chirp-pulse microwave CT (CP-MCT)", *IEEE Transac. Biomedical Engineering,* vol. 47 (5), May 2000, p. 690-699.

125. E.S. Eide, "Ultra-wideband transmit/receive antenna pair for ground penetrating

radar", *IEE Proceedings – Microw., Antennas Propag.*, vol. 147 (3), June 2000, pp. 231-235.

126. A. van der Merwe and I.J. Gupta, "A novel signal processing technique for clutter reduction in GPR measurements of small, shallow land mines", *IEEE Transac. Geoscience and Remote Sensing*, vol. 38 (6), 200, pp. 2627-2637.

127. K. O'Neill, "Radar sensing of thin surface layers and near-surface buried objects", *IEEE Transac. Geoscience and Remote Sensing*, vol. 38 (1), 2000, pp. 480-495.

128. N. Geng and L. Carin, "Short-pulse electromagnetic scattering from arbitrarily oriented subsurface ordnance," *IEEE Transac. Geoscience and Remote Sensing*, vol. 37 (4), 1999, pp. 2111-2113.

129. T. Dogaru and L. Carin, "Time-domain sensing of targets buried under a rough air-ground interface," *IEEE Transac. Antenna Propag.*, vol. 46 (3), 1998, pp. 360-372.

130. L. Gurel and U. Oguz, "Three-dimensional FDTD modeling of a ground-penetrating radar," *IEEE Transac. Geoscience and Remote Sensing*, vol. 38 (4), 2000, pp. 1513-1521.

131. F.L. Teixeira, W. C. Chew, M. Straka, M.L. Oristaglio, T. Wang, "Finite-difference time-domain simulation of ground penetrating radar on dispersive, inhomogeneous, and conductive soils," *IEEE Transac. Geoscience and Remote Sensing*, vol. 36 (6) Nov. 1998, pp. 1928-1937.

132. A. Sullivan, R. Damarla, N. Geng, Y. Dong and L. Carin, "Ultrawide-band synthetic aperture radar for detection of unexploded ordnance: modeling and measurements," *IEEE Transac. Antenna Propag.*, vol. 48 (9), 2000, pp. 1306-1315.

133. C.-C. Chen, S. Nag, W.D. Burnside, J.I. Halman, K.A. Shubert, and L. Peters Jr., "A standoff, focused-beam land mine radar," *IEEE Transac. Geoscience and Remote Sensing*, vol. 38 (1) 2000, pp. 507-514.

134. A. Ishimaru, T.-K. Chan, Y. Kuga, "An imaging technique using confocal circular synthetic aperture radar," *IEEE Transac. Geoscience and Remote Sensing*, vol. 36 (5), 1998, pp. 1524-1530.

135. IEEE Standard C95.1-1991, *IEEE standard for safety levels with respect to human exposure to radio frequency electromagnetic fields, 3 kHz to 300 GHz*, Institute of Electrical and Electronics Engineers, Inc., New York, 1992.

136. K. Caputa, M. Okoniewski and M.A. Stuchly, "An algorithm for computations of the power deposition in human tissue," *IEEE Antennas and Propagation Magazine*, 41, 4, Aug. 1999, pp. 102-107.

137. A. Taflove and S.C. Hagness, *Computational Electrodynamics: the finite difference time domain method (2nd ed.)*, Artech House, Boston, 2000.

Appendix A: Microwave imaging

Microwave imaging involves determining the profile of an object from measurements made at a distance from the object. In this case, profile refers to the physical distribution of electrical properties. An incident field illuminates the object, and a scattered field is produced. Microwave imaging attempts to relate the scattered field to the electrical property distribution in the object. This is a difficult problem, due to multiple scattering and evanescent waves. Multiple scattering results in a nonlinear relation between the scattered field and objects. The object acts as a lowpass filter, so scattered fields produced by higher spatial frequency variations are attenuated and the inverse problem does not have a unique solution. Initial approaches demonstrated the feasibility of microwave imaging, however improvements in image quality were necessary. Progress in microwave imaging has been realized with recent advances in computational methods and image reconstruction algorithms. These algorithms and prototype systems are reviewed in this appendix.

A. 1 Microwave imaging theory: linear inverse scattering

Linear inverse scattering algorithms used in microwave imaging are similar to those used in X-ray computed tomography (CT). In this method, X-rays travel through the body and are attenuated by various tissues. The emergent X-rays are recorded along a line perpendicular to the direction of propagation. The Fourier transform of this distribution corresponds to a part of the object Fourier transform (Fig. A.1) [49]. Varying the angle of illumination fills out the frequency space information. The inverse Fourier transform of this information provides the image.

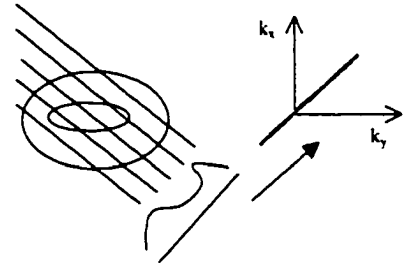

Fig. A.1 X-ray computed tomography.

With microwaves, the problem is more complex: microwaves do not travel directly (in a straight line) through the body, but experience diffraction and multiple scattering. With approximations, a theorem relating the measured scattered field to the Fourier transform of the object can be derived [50,49]. This is referred to as diffraction tomography, and the Born or Rytov approximation linearizes the relationship between the object and the scattered field. This discussion is taken from [50]. The first step in examining diffraction tomography is deriving a volume integral equation to describe the scattering problem. In inhomogeneous media, the scalar wave equation can be expressed as:

$$(\nabla^2 + k^2(\vec{r}))\psi(\vec{r}) = q(\vec{r}) \tag{A-1}$$

where Ψ is the total field, k(r) is the wave number over the object. If the Green's function for the homogeneous background is defined as:

$$(\nabla^2 + k_b^2)g(\vec{r},\vec{r}') = -\delta(\vec{r}-\vec{r}') \tag{A-2}$$

where k_b is the wave number in the background (i.e. homogeneous space), then the wave equation can be written as:

$$(\nabla^2 + k_b^2)\psi(\vec{r}) = q(\vec{r}) - [k^2(\vec{r}) - k_b^2]\psi(\vec{r}) \tag{A-3}$$

and the total field expressed as:

$$\psi(\vec{r}) = -\int_v d^3\vec{r}'\, g(\vec{r},\vec{r}')q(\vec{r}') + \int d^3\vec{r}' g(\vec{r},\vec{r}')[k^2(\vec{r}') - k_b^2]\psi(\vec{r}') \tag{A-4}$$

The first term on the right hand side of the above equation is the incident field. To linearize the second term in the expression, the Born or Rytov approximation is applied. The first order Born approximation substitutes the incident field for the total field on the right hand side of the above equation. For this to hold, the scattered field must be small and the change in phase between the incident field and wave propagating through the object less than π [49]. The Rytov approximation is less restrictive, and is applied to the phase of the field. It expresses the total field in terms of a complex exponential:

$$\psi(\vec{r}) = e^{j\phi(\vec{r})} \tag{A-5}$$

so the (source-free) wave equation becomes:

$$(\nabla\phi)^2 - k^2(\vec{r}) = j\nabla^2\phi \tag{A-6}$$

Expressing the phase as sum of incident and scattered phases and using the wave equation for the incident field, the following equation is obtained:

$$\nabla^2(\psi_o\phi_s)+k_b{}^2\psi_O\phi_s=-j\psi_O(\nabla\phi_S)^2+j\psi_oO(\vec{r}) \tag{A-7}$$

By assuming that the scatter phase is small, then the following term can be neglected:

$$-j\psi_O(\nabla\phi_S)^2 \tag{A-8}$$

With the Rytov approximation, the scattered phase can be expressed as:

$$\phi_S(\vec{r})=\frac{-j}{\psi_O(\vec{r})}\int G(\vec{r},\vec{r}')\psi_O(\vec{r})O(\vec{r})d\vec{r}' \tag{A-9}$$

The Rytov approximation is more accurate for larger objects than the Born approximation, however the change in scattered phase over a wavelength must be small.

In diffraction tomography, the object is illuminated with a plane wave and scattered fields are recorded in the far field of the object (Fig. A.2). To illustrate diffraction tomography, consider a 2D system with an incident field generated by a uniform line source [50]. This is reasonable, as most systems are assumed to be 2D and operate with TM illumination. The location of the receiver is given by ρ_R (with direction vector $\hat{\rho}_R$), the transmitter by ρ_T and the observation point by ρ' (Fig. A.2). The Green's function for the receiver is:

$$G(\vec{\rho}_R,\vec{\rho}')=\frac{j}{4}H_o{}^{(1)}(k_o|\vec{\rho}_R-\vec{\rho}'|) \tag{A-10}$$

This simplifies in the far field to:

$$G(\vec{\rho}_R,\vec{\rho}')=\frac{j}{4}\sqrt{\frac{2}{j\pi k_o\rho_R}}e^{jk_o\rho_R-jk_o\hat{\rho}_R\cdot\vec{\rho}'} \tag{A-11}$$

In the far field, the incident field generated by a uniform line source is:

$$\psi_o(\vec{\rho}_R,\vec{\rho}')=\frac{j}{4}\sqrt{\frac{2}{j\pi k_o\rho_T}}e^{jk_o\rho_T-jk_o\hat{\rho}_T\cdot\vec{\rho}'} \tag{A-12}$$

By defining $\bar{k}_R = k_o \hat{\rho}_R$ and $\bar{k}_T = k_o \hat{\rho}_T$, and substituting the above expressions into the following equation:

$$\psi_s(\vec{\rho}_R) = \int d^3 \vec{\rho}' G(\vec{\rho}_R, \vec{\rho}')[k^2(\vec{\rho}') - k_b^2]\psi_o(\vec{\rho}') \tag{A-13}$$

the scattered field can be expressed as:

$$\psi_s(\vec{\rho}_R) = \frac{j}{8\pi k_o \sqrt{\rho_T \rho_R}} e^{jk_o(\rho_T + \rho_R)} \int d\vec{\rho}' e^{-j(\bar{k}_R - \bar{k}_T)\vec{\rho}'} O(\vec{\rho}') \tag{A-14}$$

or

$$\psi_s(\vec{\rho}_R) = \frac{j}{8\pi k_o \sqrt{\rho_T \rho_R}} e^{jk_o(\rho_T + \rho_R)} O(\vec{k}_R - \vec{k}_T) \tag{A-15}$$

where O(k) is the Fourier transform of the object function. Therefore, with these approximations, the scattered field is related to the Fourier transform of the object. Both k_R and k_T have lengths k_o. By changing the direction of one of these vectors, a circle is defined in frequency space and information is obtained for frequencies less than k_o. By varying both the directions and the frequencies, information about a region of frequency space is obtained. The image is reconstructed via inverse Fourier transforms. This method is limited to scatterers of low contrast, does not consider multiple scattering, and is less effective for lossy media [50]. Additionally, the resolution is limited to half of a wavelength. This has motivated the development of iterative approaches to provide the capability to image realistic biological objects.

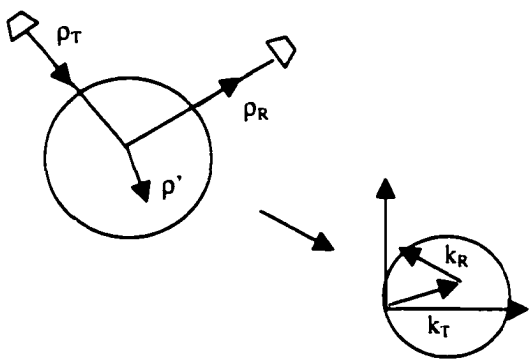

Fig. A. 2 Diffraction tomography

A. 2 Microwave imaging theory: nonlinear inverse scattering

The nonlinear inverse scattering problem has not been solved theoretically in multiple dimensions [50]. That is, methods, such as diffraction tomography, do not exist for the nonlinear case. Image reconstruction requires the use of numerical methods and iterative approaches. Two techniques that have been developed are the Born and distorted-Born iterative methods [50]. These approaches still require multiple views (i.e. illumination directions) in order to have sufficient data for image reconstruction.

The Born iterative method assumes that the object is placed in a homogeneous background medium. The algorithm involves updating estimates of the object contrast using improved estimates of the total field (Fig. A.3). This approach overcomes the limitations of the Born approximation to low contrast objects and objects of size less than a wavelength.

1. Solve Born approximation for $\delta\varepsilon_o$

$$\psi_s(r) = \omega^2 \mu \int_v d^3r' g_o(r-r')\delta\varepsilon_o(r)\psi_i(r)$$

2. Use $\delta\varepsilon_o$ to update scattered (Ψ_s) and total fields (Ψ).

3. Solve for $\delta\varepsilon_o$ using the updated fields:

$$\psi_s(r) = \omega^2 \mu \int_v d^3r' g_o(r-r')\delta\varepsilon_o(r)\psi(r)$$

4. Check for convergence. If not achieved, then return to step 2.

Fig. A.3 Born iterative method.

To improve the convergence of the Born iterative method, the distorted-Born method was introduced. This method assumes that the object is a perturbation in an inhomogeneous background. A Green's function is derived for this inhomogeneous background:

$$[\nabla^2 + k_b{}^2(r)]g_b(r,r') = -\delta(r-r') \qquad \text{(A-16)}$$

The scattered field can be written as:

$$\psi_{s,b}(r) = \omega^2 \mu \int_v d^3 r' g_b(r,r') \delta\varepsilon(r) \psi(r) \tag{A-17}$$

The distorted Born approximation substitutes the incident field with the background homogeneity ($\Psi_{i,b}$) for the total field on the right side of Eq.A-17. This equation is used to improve estimates of the object contrast, as indicated in Fig. A.4.

1. Solve the following equation for $\delta\varepsilon$:

$$\psi_{s,b}(r) = \omega^2 \mu \int_v d^3 r' g_b(r,r') \delta\varepsilon(r) \psi_{i,b}(r) \quad (*)$$

2. Check for convergence. If not achieved, then use $\delta\varepsilon$ to update the background inhomogeneity (ε_b), the Green's function (g_b) and fields ($\Psi_{s,b}$ and $\Psi_{i,b}$). Return to step 1.

Fig. A.4 Distorted Born iterative method.

For implementation, measured data replaces the scattered field on the left-hand side of the equation in Fig. A.4. To compute the incident and total fields, numerical techniques are used, so the problem space is discretized. For example, by discretizing the equation (*) in Fig. A.4 and considering the influence of frequency, and receiver and transmitter positions (r_{Ri}, r_{Tj}), we obtain:

$$\psi_{s,b}(r_{Ri}, r_{Tj}, \omega_k) = \sum_{n=1}^{N} \Delta v_n \omega_k{}^2 \mu g_b(r_{Ri}, r_n, \omega_k) \psi_{i,b}(r_n, r_{Tj}, \omega_k) \delta\varepsilon(r_n) \tag{A-18}$$

This can be written as a matrix equation:

$$\psi_{s,b} = M \cdot \delta\varepsilon \tag{A-19}$$

Because the matrix M is ill conditioned (due to fewer measurements than unknowns and the non-uniqueness of the solution), the equation is solved using optimization approaches. For example, a cost functional may be defined as:

$$I = \left\| \psi_{s,b} - M \cdot \delta\varepsilon \right\|_C^2 + \delta_t \left\| \delta\varepsilon \right\|_D^2 \tag{A-20}$$

where the matrix C is a positive definite matrix selected to weight the data, and the matrix D is selected to regularize $\delta\varepsilon$ (e.g. a difference operator to ensure smooth transitions). The functional is minimized by taking the derivative with respect to $\delta\varepsilon$:

$$[M^{+} \cdot C \cdot M + \delta_t D] \cdot \delta\varepsilon = M^{+} \cdot C \cdot \psi_s \tag{A-21}$$

Another approach to deriving the relation in (A-21) is referred to as Newton's method, Newton-Raphson method or Newton-Kantrovich method. It is called Newton's method because of similarity to the Newton-Raphson iterative method of solving nonlinear equations, and can be derived using Taylor series. The measured (true) and computed (approximate) electric fields depend on their wave numbers. Expanding about the approximate (computed) value, we obtain:

$$E_m(k_m^{\,2}) = E_c(k_c^{\,2}) + \frac{\partial E_c}{\partial k_c^{\,2}}(\Delta k^2) \tag{A-22}$$

When considering multiple excitation and observation points, the derivative term becomes the Jacobian matrix (J):

$$J\Delta k^2 = E_m - E_c \tag{A-23}$$

As the matrix J^TJ in often ill conditioned, a regularization method is applied and the equation that is solved for the electrical property update has the form:

$$[J^T J + \alpha I]\Delta k^2 = J^T (E_m - E_c) \tag{A-24}$$

where I is the identity matrix and α is the regularization parameter. This equation is similar to (A-21) because the distorted Born iterative method gives the Frechet derivative operator[1] (M), which is similar to the Jacobian matrix, J [50].

Iterative approaches have resolutions of up to $\lambda/10$, an improvement over the limit of $\lambda/2$ inherent in diffraction tomography. Additionally, larger contrasts can be inverted with iterative techniques and methods have been developed to enhance this capability [50]. As the iterative approaches do not rely on diffraction theorem and numerical techniques are used to model the system, the transmitters and receivers do not have to be in the far field of the object. However, this drastically increases the number of operations over FFT-

---

[1] the gradient of a multi-dimensional nonlinear function which relates two vectors

based diffraction tomography approaches. The number of operations increases from O(NlogN) to $O(N_t N_{iter} N^{\alpha})$ where N_t is the number of transmitters, N_{iter} is the number of iterations and N^{α} is the number of operations required to solve the forward problem [50]. This imposes an additional requirement for fast and accurate numerical techniques.

Various alternative approaches to or modifications of the DBIM are currently under investigation. For example, application of genetic algorithms to the optimization problem has been explored [116]. A variety of formulations for the direct problem have also been proposed to e.g. minimize computational cost [117]. Although much interesting work has been reported, this review is focussed on practical systems, which generally incorporate variations on the DBIM for image reconstruction. The next section reviews the evolution of microwave imaging, concluding with a comparison of several prototype systems.

A. 3 Microwave imaging systems

Early work on microwave imaging for biological applications was summarized in a book by Larsen and Jacobi [55]. The systems examined were immersed in water to provide better impedance match to the object than air, reduce multipath signal propagation, and reduce the wavelength for better resolution without increasing frequency. The basic image reconstruction techniques involved estimating S21 from the measurements [51]. This work suggested feasibility of biomedical microwave imaging, as well as the necessity of improved image reconstruction algorithms. The only system described in this volume that appears to have been pursued is that introduced by Guo et al [52]. This system used an array of water-immersed antennas, which was synthetically focussed in 3D for data acquisition. Image reconstruction was based on scanning the focus through the volume and applying the generalized Lorentz reciprocity theorem. More recently, Guo and Guo reported a high resolution image reconstruction algorithm, specifically a semi-analytic approach to solving the inverse scattering problem in three dimensions [53], [54]. However, experimental images have not been reported in the literature.

After the initial work reported in [55], a "second generation" of microwave imaging systems was introduced from the mid 1980s to the early 1990s. The two major systems used diffraction tomography to reconstruct images of objects immersed in a water bath and illuminated at 2.45 GHz. A group in France (J.-C. Bolomey and colleagues) developed a planar microwave scanner [56]. The object of interest was illuminated by a plane wave, and scattered fields were recorded at a receiver consisting of an array of 64 small dipoles positioned in a horn antenna. The object was rotated to obtain multiple views. The second system was introduced by a group in Barcelona, and consisted of a cylindrical scanner (i.e. 64 antennas encircling object) [57,58]. In this case, the incident plane wave was synthesized by appropriately exciting the transmitters and the direction of the wave was varied by adjusting the excitations. This system was used to image a human arm, and difference imaging demonstrated changes in blood flow [57]. Comparison of images reconstructed with planar and cylindrical systems showed many similarities: both systems reported resolutions of about 1 cm and capability to image electrical contrasts of about 1% [59]. However, diffraction tomography and its inherent limitations reduced the practicality of these systems. Both systems were also modified to use DBIM with the method of moments for image reconstruction (with the assumption of 2D TM mode of operation) [60, 61]. The planar system was also modified to use a "retina" of 32 by 32 small dipoles in the receiver [60]. The planar system was tested for robustness to external medium electrical properties, geometrical tolerances, and knowledge of the incident field [60]. The first two factors were not especially important, however errors in the incident field estimate degraded images, especially for high contrast objects. More recently, rapid image acquisition has been the focus of research with the planar system [118]. The cylindrical system showed that knowledge of temperature and dielectric contrast was important for accurate material property reconstruction, while frequency influenced the Green's functions [61]. Additionally, the utility of *a priori* information was demonstrated with images of a human forearm. These systems appear promising for further development of microwave imaging.

A research group at Dartmouth College has developed a microwave imaging system, initially for temperature monitoring during hyperthermia (e.g. [71]). This system has

more recently been applied to breast cancer detection [45]. This system images in 2D, and operates in the TM mode. The data acquisition initially consisted of waveguide transmitters and monopole receivers [72]. This was later adapted to monopole receivers and transmitters due to a better match between the measured data and numerical model [73]. The antennas encircle the object of interest, and the system is placed in a saline bath. A recently reported configuration [45] had a dynamic range of 135 dB, operated between 300 and 900 MHz, and had small (13 cm diameter, 16 antennas) and large (24 cm diameter, 32 antennas) imaging regions. For data acquisition, each antenna was excited consecutively and transmitted fields were measured at the antennas located opposite from the transmitter. To reconstruct images, an iterative Newton's method approach was used in conjunction with the hybrid element method [71]. This combines the finite element method, which describes the imaging region, with the boundary element method, which models the homogeneous source region. A dual mesh system was developed in order to increase computational efficiency [74]. Finer mesh was used to solve the forward problem and coarser mesh was used to reconstruct the electrical properties. The inclusion of non-active array elements has improved both localization and accuracy of reconstructed images [44]. However, errors in the position of inclusions and reconstructed values of conductivity remain present. Studies with phantoms consisting of the top of a plastic bottle filled with mixtures of corn syrup, water and salt demonstrated [119]:

- successful reconstruction of 2D slices of a 3D object (changes in diameter of contrast area with height),
- reasonable match between measured and reconstructed properties,
- reflections from the water/air interface at the top of the tank influenced images acquired near this interface, and
- the detection of a 2.5 cm diameter inclusion mimicking a tumor.

Studies of patients were also reported in [119]. Data acquisition involved exciting each antenna in the 16 element array, and recording the transmitted signals at the 9 elements opposite. Obtaining data for 25 frequencies and at 7 array heights took 20 minutes. Images of 7 planes separated by 1 cm were reconstructed, and showed consistency of

electrical properties of the breast within the same patient (both within one breast and between breasts). Additionally, an increase in permittivity was evident near the chest wall, likely attributable to the averaging of properties within the illuminated volume. In further clinical studies [113], the permittivity of breast tissue recovered from the images was significantly higher than expected from *ex vivo* measurements. The permittivity appeared to be correlated with radiographic breast density, and variations in tissue due to e.g. lumpectomy were evident in images. Several avenues of future investigation were suggested, including:

- an alternative coupling medium with better match to tissue properties,
- a better match between calibration and patient data acquisition procedures (For calibration, the antennas were immersed in a tank of coupling medium open to the air. When a patient was scanned, the chest met the coupling medium and the tank was not open to the air. A more appropriate calibration procedure might seal the tank with a bag of saline), and
- increased frequency for improved resolution, as the current system resolution is estimated as 1 cm.

Additionally, a conductive plastic suitable for simulating biological materials has been developed [120]. The material is proposed as an array housing for the microwave imaging system, however imaging results incorporating this housing have not yet been reported. Overall, the extremely exciting work by the Dartmouth group has demonstrated the feasibility of microwave breast imaging.

The Carolinas Medical Center recently introduced a microwave imaging scanner [74],[76]. This water-immersed cylindrical tomographic scanner was developed for imaging the heart. The initial system produced 2D images, operated at 2.45 GHz and had 64 antennas placed in a 36 cm diameter ring. The image reconstruction algorithms used an iterative approach with the Rytov approximation, which approximates the phase of the scattered field and can be expressed as:

$$\phi(\vec{r}) = A(\varepsilon - \varepsilon_o) \tag{A-26}$$

where ϕ is the phase and A represents the Rytov approximation. The updated permittivity was obtained using the inverse of the Rytov approximation:

$$\varepsilon^1 = \varepsilon^0 + \hat{A}^{-1}\phi \tag{A-27}$$

$$\varepsilon^{n+1} = \varepsilon^n + \hat{A}^{-1}(\phi - F(\varepsilon^n)) \tag{A-28}$$

where $F(\varepsilon^n)$ is the direct solution, which is found using an iterative approach. To increase computational efficiency, the system was modified to incorporate a dual mesh scheme [77]. In addition, the iterative algorithm was changed to a Newton's method approach and minimized a functional relating the change in the scattered field to the change in permittivity. A 3D approach to imaging with this system was introduced in [78], using clusters of transmitters with code division techniques to decrease data acquisition time. The transmitters illuminated the object with a localized 2D TM wave to allow for reconstruction of slices. Image reconstruction uses the Born approximation and the assumption of a 2D TM illuminating wave to find a relation between the measured scattered field and permittivity contrast. Taking the Fourier transform and discretizing results in a linear system of equations that is solved with Tikhonov regularization and a standard elimination method. Simulated data were used to obtain images of a sphere with inclusions, and experimental images of a heart model were obtained by illuminating with 1 transmitter. Initial results are promising, but limited to weakly scattering objects. The spatial resolution was investigated by operating the 3D tomograph in 2D mode, and found to be approximately 6.5 mm ($\lambda/2$) for a 2D complex object in a water bath and illuminated at 2.36 GHz [122]. Further investigations demonstrated the need to reconstruct images of complex objects with 3D approaches, rather than 2D slices [121]. The methods proposed for 2D imaging have been applied to the problem of breast cancer detection [123]. These investigations use computer simulations to illuminate a 2D model, consisting of breast tissue, skin, muscle, ribs, lung tissue and tumors, with an array of 31 monopole elements at 2 GHz. With appropriate modifications to the algorithms, detection of tumors at depths of up to 3-4 cm and directly under the array appears feasible.

A modified approach to microwave imaging has been explored by a group in Japan. As discussed earlier in this appendix, the principles of x-ray CT cannot be directly applied to

microwave imaging due to diffraction and multiple scattering. Chirp CT avoids these issues by isolating the directly transmitted signal (along the shortest path) [43]. In the proposed system, a chirp radar signal between 1 and 2 GHz was applied with a waveguide antenna. An identical receiving antenna was placed 28.2 cm from the transmitter. A portion of the transmitted signal was mixed with the received signal, resulting in a lower beat frequency. The frequency component of the signal corresponding to the distance between the two antennas was isolated and used with x-ray CT algorithms to reconstruct the image. In order to evaluate system resolution, two cylinders of 5.5 cm diameter and filled with 0.2% saline solution were placed in a 0.4% saline solution bolus. The distance between the cylinders was decreased from 6.0 cm to 0.5 cm, and inspection of images for separation of the two objects resulted in a resolution estimate of 1 cm. While this system was proposed for monitoring temperature increases during hyperthermia, it is also suitable for breast imaging. Recent investigations have involved image improvement via deconvolution of the estimated point spread function [124].

A microwave system for nondestructive testing and location of underground pipes was reported by Chew et al [80]. While this system was not developed for medical applications, it is of interest because of the combination of ultra-wideband signals and the DBIM. The FDTD method was used in conjunction with the DBIM to reconstruct images. In the time domain, the DBIM corresponds to updating the incident fields, and computing the scattered fields recorded at each receiver. The final step is back-propagation of the field recorded at the receiver to a point in the problem domain and correlation of this field with the incident field at that same point. This process is repeated for each transmitter. Therefore, 3 calls to the forward solver per transmitter position are required at each iteration. Techniques have been developed for imaging high contrast scatterers [81], as well as use of ultra-wideband signals [80]. This approach is extensible to 3D [50].

Microwave imaging of biological structures remains a difficult problem, in spite of advances in both data acquisition and image reconstruction methods. Measurements are

difficult to obtain. First, the frequency must be selected such that reasonable resolution and sufficient signal-to-noise ratios (SNR) are attained. As the scattered signals are small, a large dynamic range is required. Components with sufficient sensitivity and isolation must be used. Many systems use modulation and I/Q detection at a lower frequency to reduce costs. A large number of measurements is needed for image reconstruction, however measurement times must be of reasonable duration if the human subject is expected to remain still. This must also be balanced with sufficient time in each location to record a reliable signal. Once the measurements are completed, the data must be transferred from 3D measurement space to 2D image space. Some systems use calibration to compensate for this factor. The image reconstruction algorithms must be capable of inverting contrasts in electrical properties that will be present in objects (i.e. the assumption of small scattered fields may not be valid). *A priori* information may be required for optimum performance. The computational costs of image reconstruction must be considered, as e.g. applying the DBIM to a 3D object may be impractical. Overall, the system must have sufficient resolution, both spatial and in electrical contrast, as well as the ability to image objects of suitable dimension for the application. The performance of systems described in this chapter is compared in Table 2-3.

For detection of tumors in the breast, the microwave system must be capable of inverting large contrasts while providing sub-cm resolution. The Dartmouth system appears to image large contrasts, but has not yet achieved sufficient resolution. Promising results have been obtained with this system, implying the feasibility of microwave breast cancer detection. However, alternative methods, such as microwave confocal imaging, provide advantages in simplicity and robustness that make them an attractive alternative to the tomographic approach.

Appendix B: Ultra-wideband radar and buried object detection

Limitations inherent in microwave imaging have not been entirely mitigated with the advances in microwave imaging described in Appendix A. For example, resolution is restricted to about 0.1λ even with the most advanced approaches. This has motivated the search for alternative microwave imaging techniques for medical imaging. One particular area of interest is ground penetrating radar for mine detection. The problem of detecting a mine buried in soil, which is a lossy, heterogeneous substance, is an analogous problem to detecting tumors in normal breast tissue. Relevant literature from ultra-wideband ground penetrating radar is reviewed in this appendix.

For breast tumor detection, ultra-wideband radar is of interest. Ultra-wideband (UWB) is defined by DARPA as having a fractional bandwidth greater than 25% [87], where the fractional bandwidth is:

$$bw = \frac{2(f_H - f_L)}{f_H + f_L} x100\% \tag{B-1}$$

The signal for breast tumor detection is ultra-wideband due to the requirements for resolution and penetration into the breast. Sufficient penetration limits the upper frequency to 10 GHz, while sub-cm resolution demands a bandwidth of 5 GHz or greater, as the resolution is inversely proportional to the bandwidth. This results in an ultra-wideband signal.

The basic principles of UWB radar are similar to those of conventional radar, so similar performance limits are encountered [87]. For example, the detection range depends on the effective radiated power (and the antenna), response of the target, propagation medium and clutter. However, UWB offers several advantages. For the breast cancer application, a key advantage is the resolution capability. Another benefit is the availability of information about the target over a wide range of frequencies. This may allow for identification of resonant frequencies, which relate to the shape of the tumor. UWB radar does require consideration of issues not encountered in conventional radar

[87]. For example, antennas appropriate for radiation of UWB signals must be designed. With the use of antenna arrays, the transmission of pulses results in different design and performance issues. The beamwidth is determined by the extent over which the pulses arrive simultaneously. Sidelobes are created by interference of pulses, and can be modified by the pulse repetition frequency. The radiated signal may experience dispersion as it travels through the medium, and the pulse may be designed to compensate for these effects. Adequate signal-to-noise ratio (SNR) must be achieved, and this is complicated by the noise throughout the spectrum, as well as differences in signal attenuation over the frequency band. While range resolution is determined primarily by signal bandwidth, synthetic aperture approaches may be used to improve resolution in the azimuth direction (i.e. scanning the antenna to create a larger aperture and applying appropriate signal processing techniques to form an image). Especially appropriate for medical applications is a circular aperture [66]. Hardware issues also arise, as transmitters and receivers capable of generating and receiving short pulses are required. In this thesis, the focus is on appropriate antenna design and signal processing for effective image formation, rather than the related hardware issues. In the next two sections, antennas and signal processing are reviewed.

B. 1 Antennas for remote sensing

Remote sensing or buried object detection involves the radiation of temporally short pulses and examination of (usually) back-scattered signals. This requires an antenna to radiate the pulse, as well as a method of detecting small backscattered signals in the presence of clutter. The clutter in this case may include large reflections from other scatterers, small reflections from non-uniform media, and reflections from the antenna itself. Effective radiation and reception of an ultra-wideband pulse requires both constant gain for transmission and constant receiving area over the frequency band [88]. With constant gain for transmission, the radiated power per unit area at distance R is:

$$P_a(f) = \frac{P_t(f)G_t(f)}{4\pi R^2} \tag{B-2}$$

The received power reflected from a target is:

$$P_r(f) = \frac{K(f)P_t(f)G_t(f)A_{target}(f)A_{re}(f)}{(4\pi R^2)^2} \tag{B-3}$$

where K is the system sensitivity, A_{re} is the receiving area of the antenna and is related to gain by:

$$G_r(f) = \frac{4\pi A_{re}(f)}{\lambda^2} \tag{B-4}$$

If the same antenna is used for reception and transmission, then the requirements of constant gain and area cannot be simultaneously met. An alternative approach is to use signal processing to extract information about the antenna from the received signal, such as correcting for the antenna transfer function.

The antenna transfer functions for transmitting and receiving are thus of interest. An antenna transmitting an UWB signal has a radiated field that is proportional to the derivative of the excitation signal [87]. It can be shown that the electric field and magnetic vector potential are related as:

$$E = \frac{\partial A}{\partial t} \tag{B-5}$$

Because the magnetic vector potential is related to the current, the electric field is proportional to the time derivative of the current. If the current is given by an envelope modulating a sinusoid:

$$s(t) = a(t)\cos\omega_c t \tag{B-6}$$

then the derivative is:

$$\dot{s}(t) = -\omega_c a(t)\sin\omega_c t + \dot{a}(t)\cos\omega_c t \tag{B-7}$$

The derivative of the envelope is proportional to the bandwidth of the signal. For a narrowband signal, the first term dominates the derivative, as the center frequency is much greater than the envelope bandwidth. For a wideband signal, the second term dominates. Therefore, the transmitted signal is similar to the derivative of the excitation. Another important distinction for antennas radiating UWB signals is reciprocity. The Carson-Rayleigh reciprocity theorem must be considered [89]:

$$F_o(\theta,\phi,\omega) = \beta h_e(\theta,\phi,\omega) \quad \text{(B-8)}$$

where F_o is the field factor, h_e is the effective height, and β is the phase constant. Again, the transmitted field is proportional to the derivative of excitation. Further, for the field incident on the antenna to be the same as the transmitted field, the antenna excitation must be proportional to the time integral of the incident field.

Additional factors must be considered when designing antennas for radiating pulsed EM fields [88]. First, the narrowband definition of far field does not apply to ultra-wideband signals. For UWB antennas, the far field is the distance at which pulses from locations along the antenna arrive simultaneously. The pulse shape is therefore constant and the peak power varies inversely with R^2. The antennas require broad bandwidth, which should be considered in terms of both impedance matching and radiation pattern. For UWB antennas, radiation pattern may be defined in terms of the peak power, or the total power. The phase center is the apparent point from which the antenna radiates at a specified frequency. If the phase center changes with frequency, then a frequency dependent time lag is added to fields off the antenna axis, thus changing the transfer function of the response. The transient pulse propagation characteristics on the antennas are also examined, especially for reflections at the feed and end that cause signal distortion. Both attenuation and dispersion (resulting in increased pulse width) can be problematic. Measures for the characterization of antennas with respect to ultra-wideband excitations have been proposed, and a set of these are summarized in 4.1.

Many designs for ultra-wideband antennas have been proposed, including biconical antennas, the TEM horn, spiral antennas, notches, bowties, and loaded dipoles [88]. Some of these antennas are not well suited to the breast cancer application, due to lack of physical compatibility (e.g. horns), variation of parameters with frequency, or radiation of circular polarization (e.g. spirals). In selecting an antenna for this research, the focus is on resistively loaded dipoles and bowties. Cylindrical monopole, conical monopoles and bowties have been previously investigated.

The resistively loaded dipole antenna was originally proposed by Wu and King [103], and incorporates a resistive profile such that a travelling wave results (Appendix C). More recently, Maloney and Smith investigated the resistively loaded monopole antenna with a Wu-King profile designed at zero frequency [90]. The antenna was simulated with the FDTD method, incorporating subcell modeling of thin sheets. The reflected voltage in the feed line, surface charge density on the antenna, and far zone electric fields were computed for Gaussian and differentiated Gaussian pulses. An antenna was constructed with high frequency resistors, and measurements made of S11 and S21 (with a small probe). Excellent agreement between FDTD simulations and measurements were obtained. Montoya and Smith [91] compared several approaches to designing loaded monopoles, including the resistively loaded Wu-King profile, a resistive-capacitive Wu-King profile, an empirically designed resistive-capacitive profile, an exponential capacitive profile and a linear capacitive profile. With the FDTD method, reflected voltages in the feed line, reflected energy, efficiency, time-domain gain, and fidelity were computed. Minimum reflected voltages and a radiated signal similar to the input pulse were obtained with Wu-King profiles. The trade-off was greatly reduced efficiency. Resistively loaded vee dipoles were investigated, as these antennas increased the directivity and SNR over that obtained with a dipole [92]. PEC, constant and linearly tapered (i.e. Wu-King profile) resistive loading were compared. The antennas were modeled in free space and operating over a ground plane. Results indicated a decrease in clutter (due to reflections from the surface, multiple reflections, and reflections from the antenna ends) with resistive loading, especially for the tapered profile. Also, the spot width decreased slightly with tapered loading, hence increasing spatial selectivity. For detection of objects, the reflections from objects, which were reduced with the resistive loading, must be greater than the system noise for detection. As a greater signal was received with the tapered profile, that design was recommended. Montoya and Smith [93] also investigated the resistively loaded vee dipole for the detection of cylindrical land mines buried in soil. A pulse was selected to provide adequate penetration and similar reflection ratios between the mine and soil surface with various soil types. The resistively loaded vee dipole was required for mine detection, as this antenna reduced clutter below the level of the mine returns. The influences of changing the height of the

antenna over the surface, the depth of mine, and the inclusion of rocks were studied. The FDTD results were confirmed with simple experiments. The previously published studies indicate that resistively loaded dipoles are useful for radiating UWB pulses. Vee dipoles appear feasible for mine detection, and should provide better directivity and hence SNR than straight dipoles.

Other antenna designs have been investigated for pulse radiation. Maloney and Smith examined a resistively loaded rotationally symmetric conical monopole with FDTD [94]. The antenna was optimized by adjusting the offset between the ground plane and cone, the addition of a matching ring, and use of a resistive sheet. The resistive loading ensured that the reflected voltages were -40 dB compared to the excitation. Pulse shape, reflection coefficient and gain over the frequency range were examined. Antennas were constructed and measurements found to be in good agreement with computations. Overall, the resistively loaded antenna had a wider bandwidth (10 to 1) and better pulse replication abilities than the metal conical monopole.

Bowtie antennas for pulse radiation have been explored by several authors. Shlager et al modeled bowties using FDTD [95]. First, simulations of a metallic bowtie were compared to measured results for unipolar bowties. To improve the bowtie for UWB radiation, capacitance was added to reduce feed point reflection, and resistive loading was added to minimize end reflections. Computations were compared to measurements, and good agreement was obtained. The resistively loaded bowtie antenna has been further modified by Hagness et al for use in biological sensing [85]. The bowtie design incorporated resistive loading with material properties selected to suppress the reflected pulse effectively. This antenna was described in Section 3.4, and computed end reflections were 125 dB below the excitation. A variation on this design was recently proposed, involving two bowtie monopoles oriented orthogonally and mounted on a vee-shaped ground plane [125]. The space between the bowties and ground plane was filled with absorbing material to provide current attenuation along the bowtie. Results indicated wide bandwidth (400 to 6000 MHz), stable field pattern over the bandwidth and relatively constant impedance. Bourgeois and Smith have used metallic bowties for

remote sensing [96]. These antennas were placed in a shielded metal box, and had a 200 ohm load connected to each corner. With the antenna placed above ground, a differentiated Gaussian pulse (derivative of excitation) was evident in the radiated field. This pulse decreased in magnitude off boresite, and directivity increased with increased height above ground. Signals reflected from pipes were observed, and subtraction of simulations with and without the pipe present was used to reduce effects of reflections that could not be windowed out. In summary, the bowtie has been selected for several buried object detection applications, but requires resistive loading for sensitivity to breast tumors.

The antennas described in this section have been examined as single elements, not as an array. Further investigation is required to resolve issues such as coupling between elements, causing changes in element characteristics and pulse re-radiation.

B.2 Signal processing

The UWB signal is radiated by the antenna, and reflections from the region under interrogation are recorded. The receiver may record a copy of the signal, or use threshold or correlation detection [97]. Threshold detection requires the received signals to be greater than a certain level, while correlation detection involves determining the similarity of the received signal to a reference. In both cases, the original signal is lost. For ultra-wideband radar imaging used in inspection of subsurface structures or buried object detection, images of the interrogated region are created. A simple image formation algorithm is applied to the recorded returns [98-101], and has been used by Hagness et al for breast tumor detection [41]. First, the time delay from each antenna location to a point in the interrogated region is computed:

$$t(k,x,y,z) = 2\frac{d(k,x,y,z)}{v} \tag{B-9}$$

where k is the antenna number, t is the time delay, d is the distance from antenna k to the point of interest, and v is the velocity of propagation. Next, the signals from each antenna are summed:

$$I(x,y,z)=\sum_{k=1}^{N} R(k,t(k,x,y,z)) \tag{B-10}$$

where I is the pixel value, N is the number of antennas, and R is the matrix of recorded returns. This algorithm uses knowledge of the velocity in the media of interest, which may be difficult to obtain in the case of mine detection [99]. The algorithm described above applies to returns recorded monostatically, but is extensible to the bistatic case. With an oblique angle of incidence, the ray refracts when it enters different media. Techniques based on planar layered media have been proposed to estimate the path length that the signal travels, and result in improved images [98].

To further improve the image, the signal may be modified before the image formation algorithm is applied. For example, information about the antenna pattern may be incorporated [87, 98]. As shown in Fig. B.1, returns at a given antenna location may be used to form only a limited portion of the image, corresponding to points within the antenna beamwidth. Knowledge of the antenna pattern may be used to equalize returns incident from different angles. The attenuation of the signal as it travels through the medium may be corrected by scaling returns by r^2, where r is the distance from the antenna to the point of interest [98]. Clutter reduction is an active area of research, and several approaches to this problem have been proposed. For signal sets in which common elements, such as returns from the air-ground interface, are present, signals may be aligned, using this characteristic reflection and averaged, to remove this effect [99,101]. Another approach is parametric modeling of the clutter, and a recently proposed iterative algorithm fit damped exponential models and estimates of the target signature to data [126]. Extremely impressive results were obtained, both with simulated data including inhomogeneities and measurements of a plastic mine embedded in soil [126,133]. After clutter reduction, targets are easily identified and false alarms are not apparent in images. In addition, the impact of various factors on clutter (and therefore detection capability) have been examined with computer simulations. The influence of polarization on clutter [130] and appropriate models for clutter from rough air-ground interfaces [129] have been examined. Additionally, changes in the scattered signal from the target with dispersive materials [131], various antenna-target orientations [128] and

use of polarizations [132] have been examined. Such studies provide interesting techniques for application to confocal microwave imaging, and underline the necessity of understanding both the clutter and target reflections for development of effective signal processing methods.

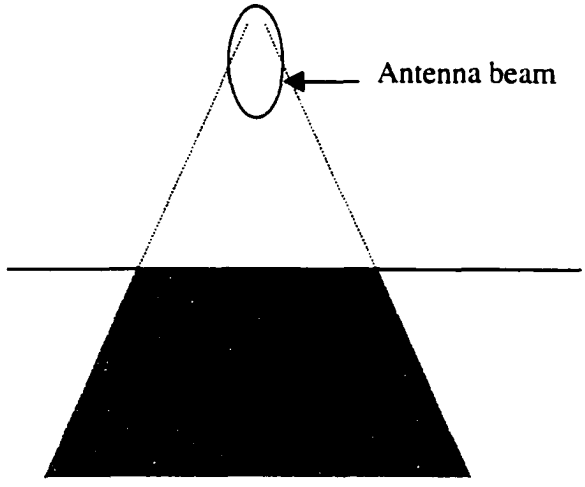

Fig. B.1 Illustration of range over which returns from a given antenna are used in image reconstruction.

Once the image is formed, reliable detection of objects may involve further signal processing. For example, resonant frequencies of objects may be obtained using techniques such as the singularity expansion method [87]. Complex natural resonance of dielectric spheres and bubbles have been studied for application to mine detection [102]. Energy penetrates, reverberates, and radiates from plastic mines, providing frequency signatures, however contrast between the mine and background medium is required for significant signals [100,102]. This technique is promising for breast cancer detection due to the large contrast between tumors and normal tissues. Hagness et al have examined the frequency responses of different tumor shapes, finding significant differences between cylinders and spheres [48]. Another method of image enhancement relates to advances in computational techniques that make modeling of large, complex domains feasible. Model-based template matching was proposed for mine detection [100]. The responses of mines at various depths and in various soils were computed, and used to form image templates. The variables (location and soil) were included in a vector γ, and

described with probability density functions p_γ. The image created from the measured data was compared to each template shifted to various image locations:

$$I(x_o, y_o) = \int dx \int dy \int d\gamma M(x, y) I(x - x_o, y - y_o; \gamma) p_\gamma(\gamma) \qquad \text{(B-11)}$$

where I is the computed image, M is the measured image, (x_o, y_o) is the shift in location of the template. The result is compared to a threshold for object detection. Variations on this approach have been tested in order to reduce computational costs. The technique was applied to a series of images represented with increasing resolution (i.e. images formed with lower frequency data). Only regions of interest identified on lower resolution images were examined further. Another approach involved matching a 1D slice through the image at the suspicious location with 1D templates. A similar technique involving matching measured and reference waveforms has also been proposed [**127**]. This method was developed for layers of water and ice, and proved capable of detecting mine-like targets in frozen ground.

In this appendix, ultra-wideband ground penetrating radar was reviewed with an emphasis on antennas for radiating ultra-wideband signals and signal processing. Common to the systems and approaches reported in the literature is the necessity for detailed understanding of the antenna performance, the interactions between the target and antenna, and the behaviour of the clutter in order to provide successful target detection.

Appendix C: Wu-King design equations

The Wu-King resistive profile is designed such that the internal impedance per unit length ($Z^i(z)$) supports only an outward travelling wave [103]. With time-harmonic fields, an axial current ($I_z(z)$) flowing along the antenna and a voltage source located at z=0, this antenna can be described by the following equation:

$$(\frac{\partial}{\partial x^2}+k^2)A_z(z)=\frac{jk^2}{\omega}(Z^i(z)I_z(z)-V_o\delta(z)) \tag{C-1}$$

where $A_z(z)$ is the axial component of the vector potential on the surface of the antenna. The vector potential may also be expressed as:

$$A_z(z)=\frac{\mu_o}{4\pi}\int_{-h}^{h}I_z(z')K(z,z')dz' \tag{C-2}$$

where

$$K(z,z')=\frac{e^{-jkr}}{r} \tag{C-3}$$

and

$$r=\sqrt{(z-z')^2+a^2} \tag{C-4}$$

where a is the radius of the antenna. In order to have the ratio of vector potential and current constant,

$$\int_{-h}^{h}I_z(z')K(z,z')dz'\approx I_z(z)\varphi \tag{C-5}$$

Then the vector potential can be expressed as:

$$A_z(z)=\frac{\mu_o}{4\pi}I_z(z)\varphi \tag{C-6}$$

and (C-1) becomes:

$$(\frac{\partial^2}{\partial z^2}+k_o^2)I_z(z)\approx j\frac{4\pi k_o}{\varsigma_o\varphi}[Z^i(z)I_z(z)-V_o\delta(z)] \tag{C-7}$$

where ζ is intrinsic impedance. By defining:

$$f(z)=\frac{4\pi}{\varsigma\varphi}Z^{i}(z) \tag{C-8}$$

then

$$(\frac{\partial^2}{\partial z^2}+k^2-jkf(z))I_z(z)=-j\frac{4\pi k}{\varsigma\varphi}V_o\delta(z) \tag{C-9}$$

The right-hand side of the above equation is zero, except at the driving point. If the function f is given the value:

$$f(z)=\frac{2}{h-|z|} \tag{C-10}$$

then (C-9) becomes:

$$(\frac{\partial^2}{\partial z^2}+k^2-j\frac{2k}{h-|z|})I_z(z)=0 \tag{C-11}$$

The solution to (C-11) is an outward travelling wave:

$$I_z(z)=C(h-|z|)e^{-jk_o|z|} \tag{C-12}$$

By applying the Lorentz condition, the constant C is determined:

$$C=\frac{j2\pi\omega\varepsilon_o V_o}{\varphi(1+jkh)} \tag{C-13}$$

To find the design parameter φ, expressions for I and K are substituted into (C-4),

$$\varphi(z)=\frac{\int_0^h(h-z')e^{-jkz'}[\frac{e^{-jkr_1}}{r_1}+\frac{e^{-jkr_2}}{r_2}]dz'}{(h-z)e^{-jkz}} \tag{C-14}$$

At z=0 and assuming kz<<1 and a<<h,

$$\varphi=2\int_0^h\frac{e^{-j2kr_o}}{r_o}dz'-\frac{2}{h}\int_0^h e^{-j2kz'}dz' \tag{C-15}$$

which is approximated by:

$$\varphi=2[a\sinh h/a-C(2ka,2kh)-jS(2ka,2kh)]+\frac{j}{kh}(1-e^{-j2kh}) \tag{C-16}$$

where C and S are generalized sin and cosine integrals. The variation in antenna impedance with length is found by combining (C-8) and (C-10):

$$Z^{i}(z)=\frac{\varsigma\varphi}{2\pi(h-|z|)} \tag{C-17}$$

Appendix D: Antenna modeling results

D. 1 Antenna 2: Resistively loaded monopole designed in skin.

Results for antenna 2 are presented in Fig. D.1 to Fig. D.3. Maximum fields measured 0.5 cm and 1 cm from the antenna are shown in Fig. D.1 and Fig. D.2. Results are very similar to those of antenna 1. Additionally, fidelity to the derivative of the excitation is better than 0.95 for the dominant θ component computed 1 cm from the antenna. As shown in Fig. D.3, time domain gain is greater for this antenna than antenna 1.

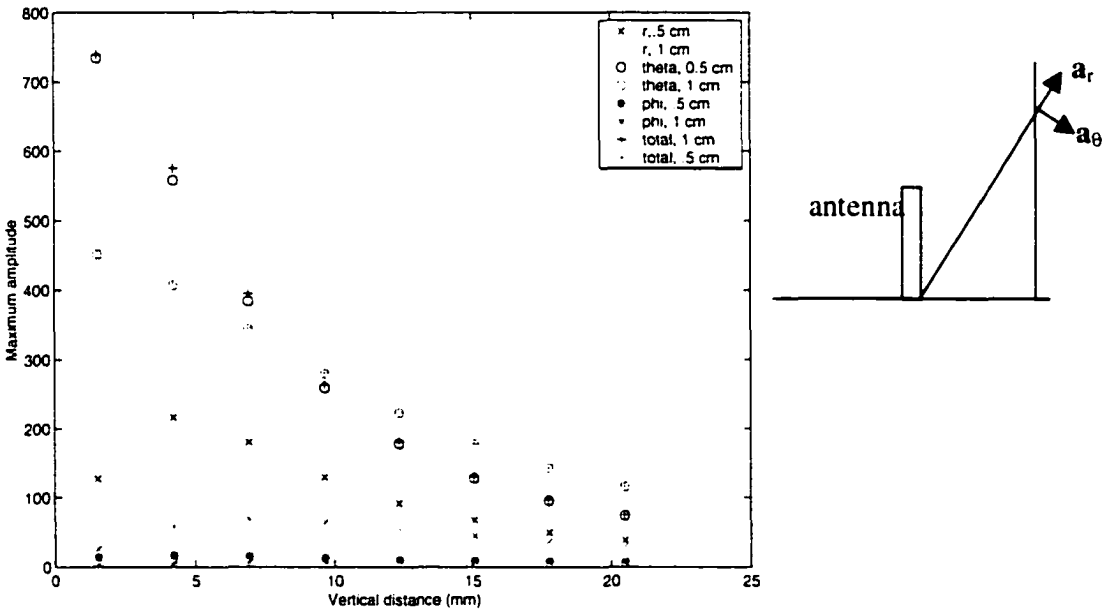

Fig. D.1. Maximum field variation with height above the ground plane. Fields are recorded parallel to the antenna.

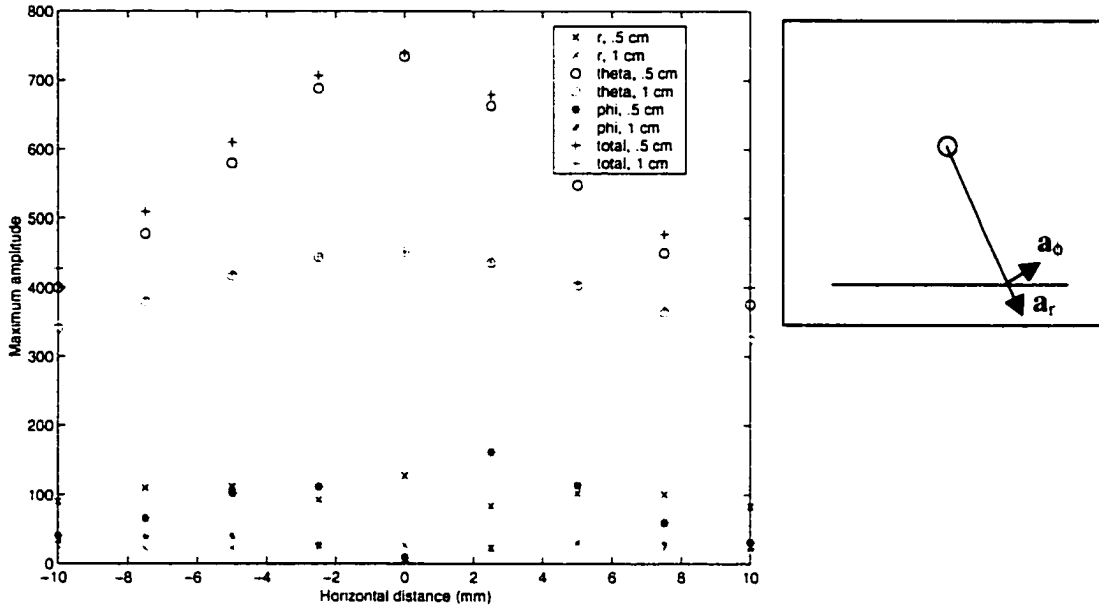

Fig. D.2. Maximum field variation with horizontal distance. Fields are recorded along line perpendicular to the antenna at a height of 1.5 mm above the ground plane.

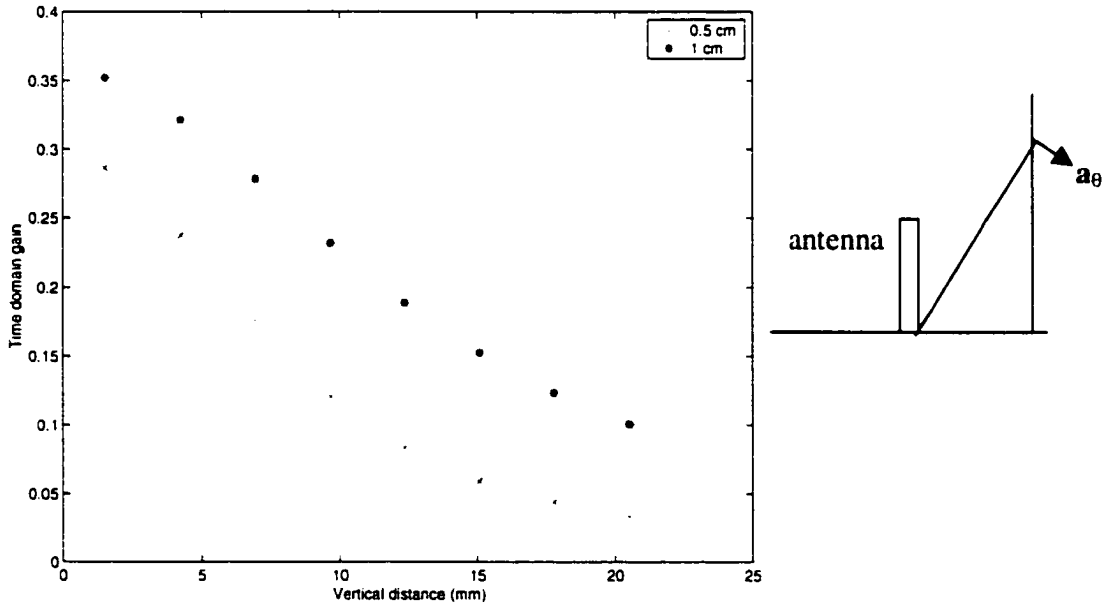

Fig. D.3. Time domain gain variation with height above ground plane for dominant fields recorded parallel to antenna.

D. 2 Antenna 3: Vee dipole designed in breast tissue

The vee dipole designed in breast tissue is examined at 2 and 2.5 cm from the antenna feed (1.4 and 1.9 cm from the end of the antenna). Maximum field amplitude variation with height is shown in Fig. D.4 for the plane parallel to the antenna and in Fig. D.5 for the perpendicular plane. The field pattern shows a greater r component than those of the straight dipoles. High fidelity to the derivative of the excitation is obtained for both field components (Fig. D.6). The time domain gain (Fig. D.7) is greater than that obtained with antenna 1 at 2 cm from the feed, as expected. However, the gain is lower than that obtained at a comparable distance (1 cm) with antenna 2.

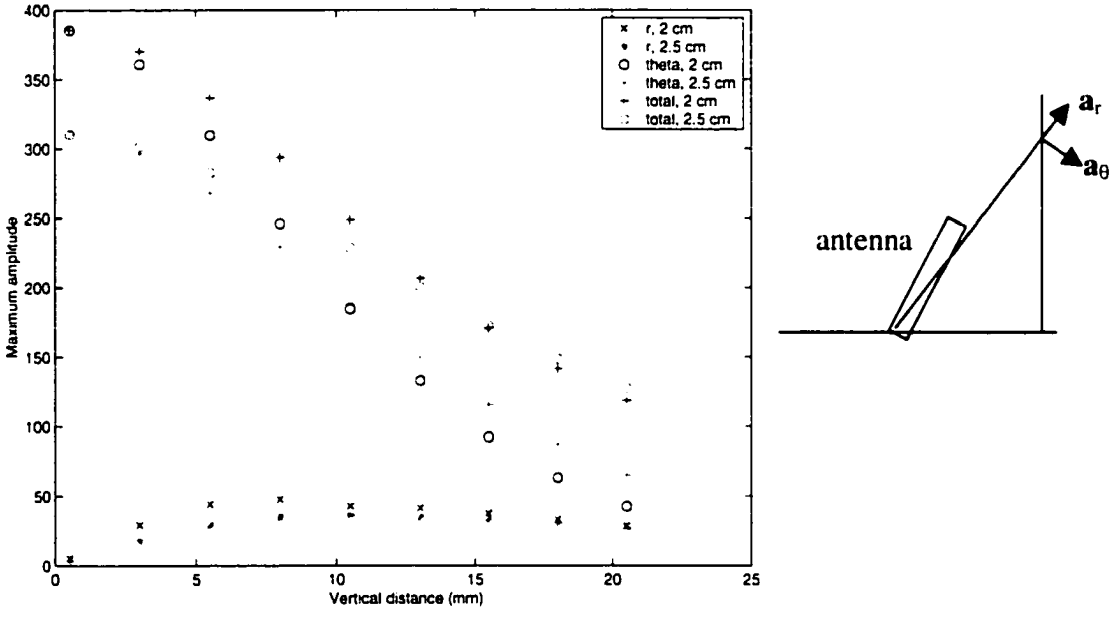

Fig. D.4. Maximum field variation in plane parallel to antenna.

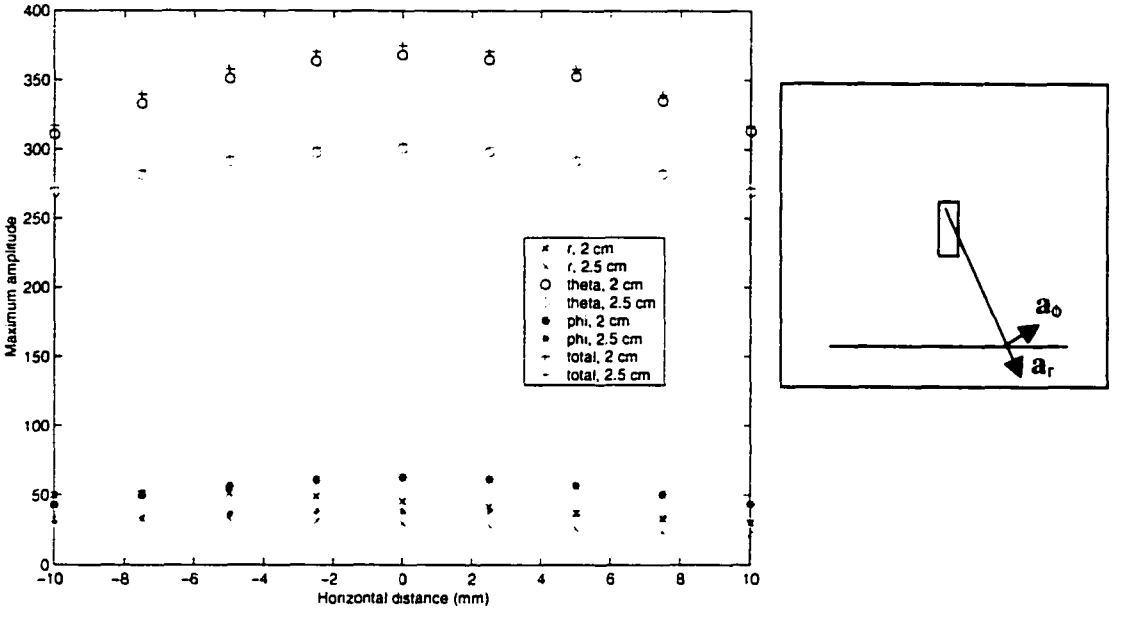

Fig. D.5. Maximum field variation in plane perpendicular to antenna at height of 2.5 mm above the ground plane.

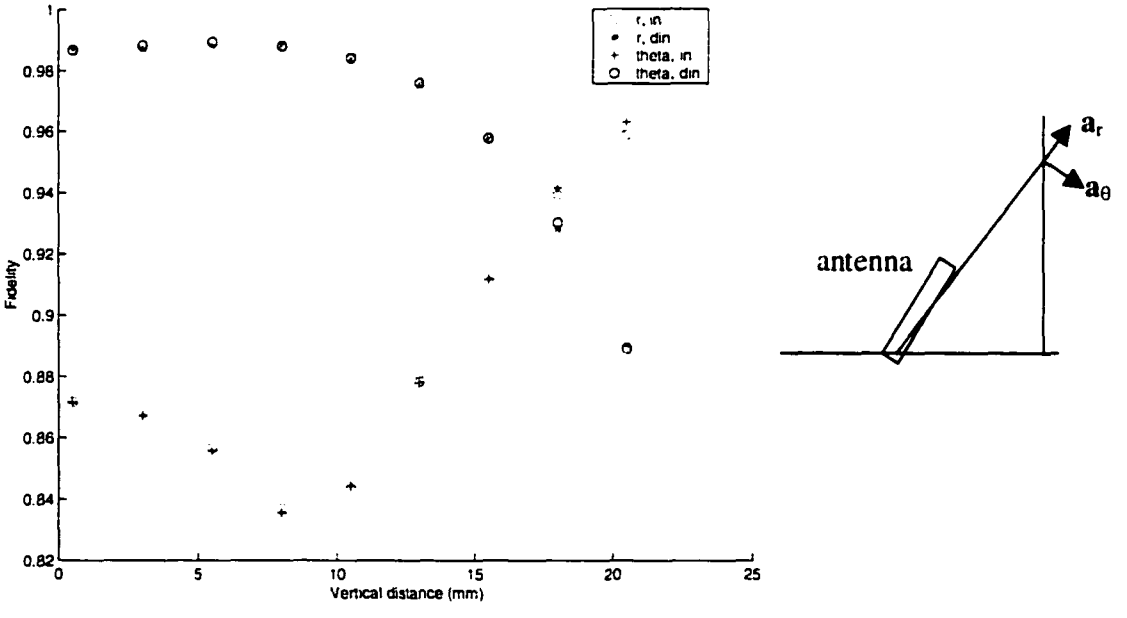

Fig. D.6. Fidelity for fields computed 2 cm from and parallel to antenna 3.

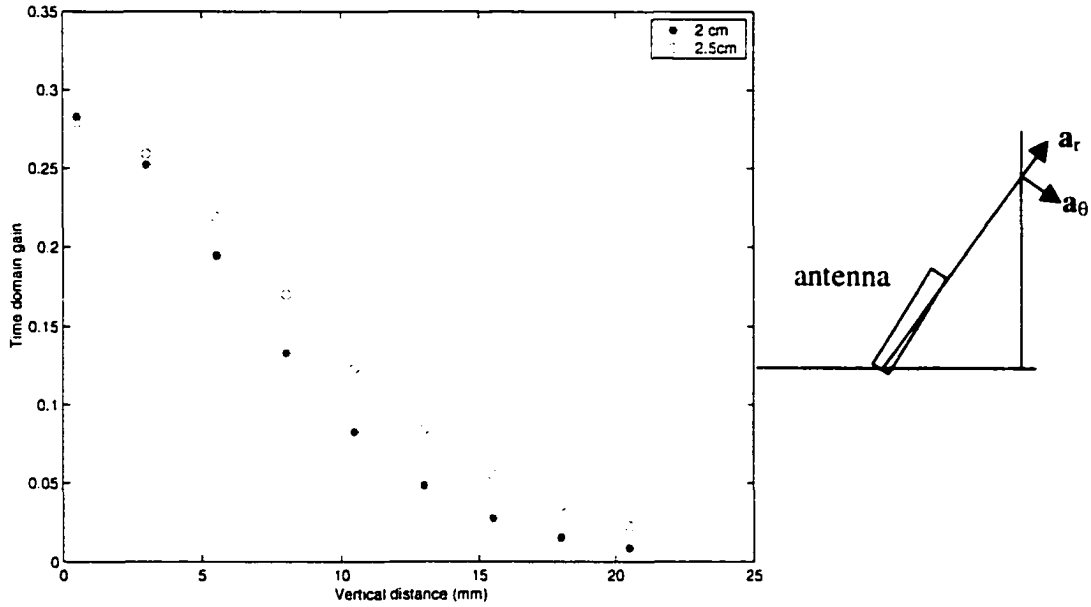

Fig. D.7. Time domain gain for dominant field components of antenna 3.

D.3 Antenna 4: bowtie designed in breast tissue

Results for the bowtie antenna are summarized in Fig. D.8 to Fig. D.12. Similar to the vee dipole, maximum field variations show greater contributions from the r component. Both maximum field and fidelity results indicate that fields are changing 1 cm from the antenna, so a placement of 2 cm is suggested. Finally, the time-domain gain of this antenna is the smallest of all candidate designs.

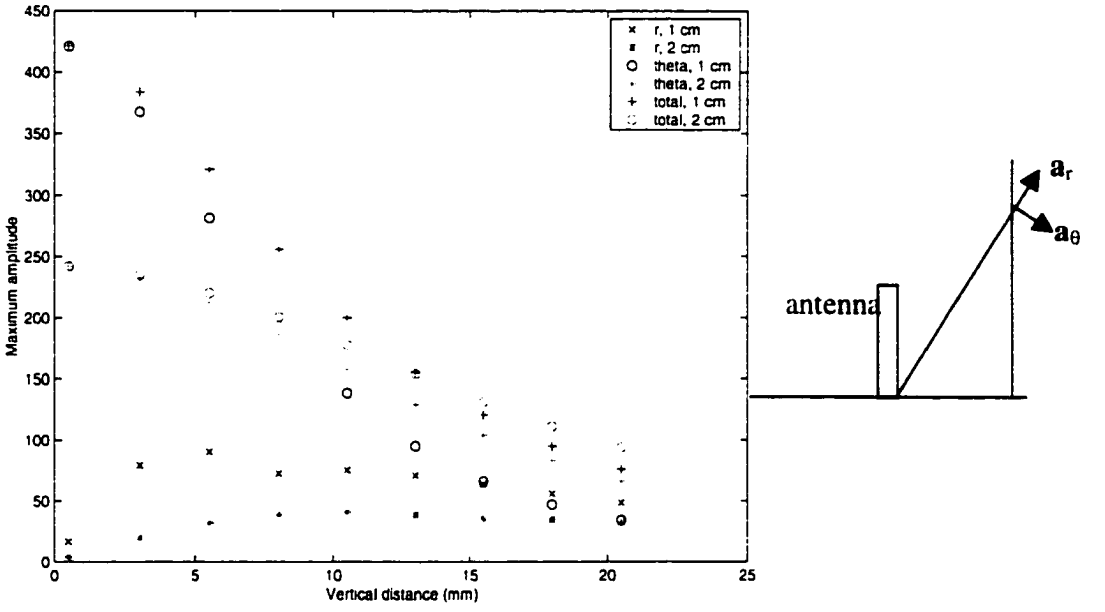

Fig. D.8. Maximum field amplitude variation with height above the ground plane. Fields are measured parallel to the bowtie.

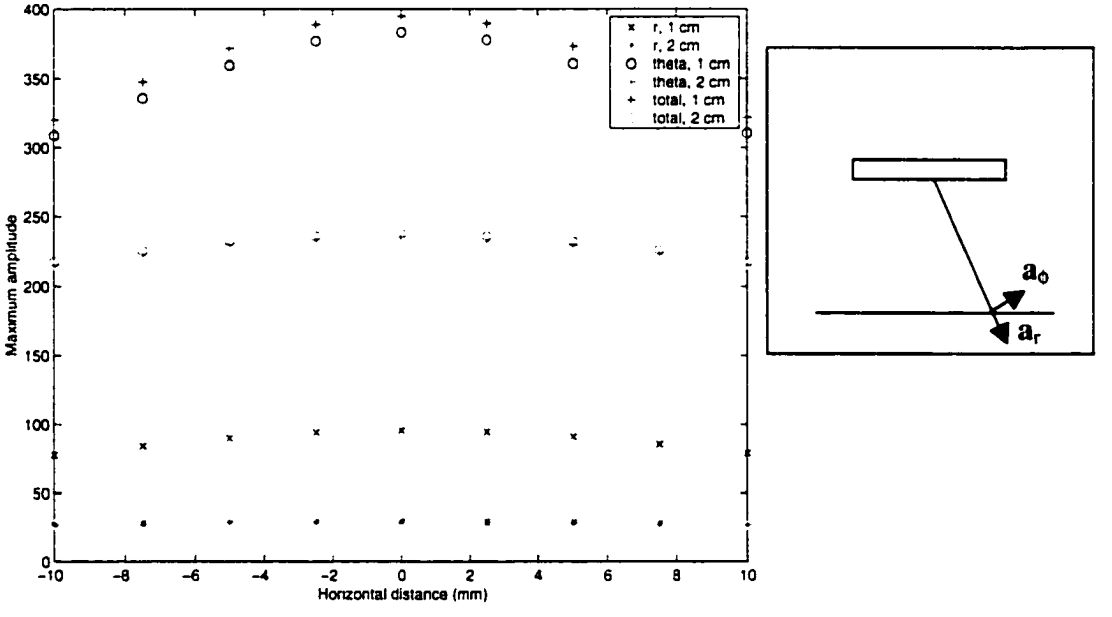

Fig. D.9. Maximum field variation in direction perpendicular to the bowtie at height of 2.5 mm above the ground plane.

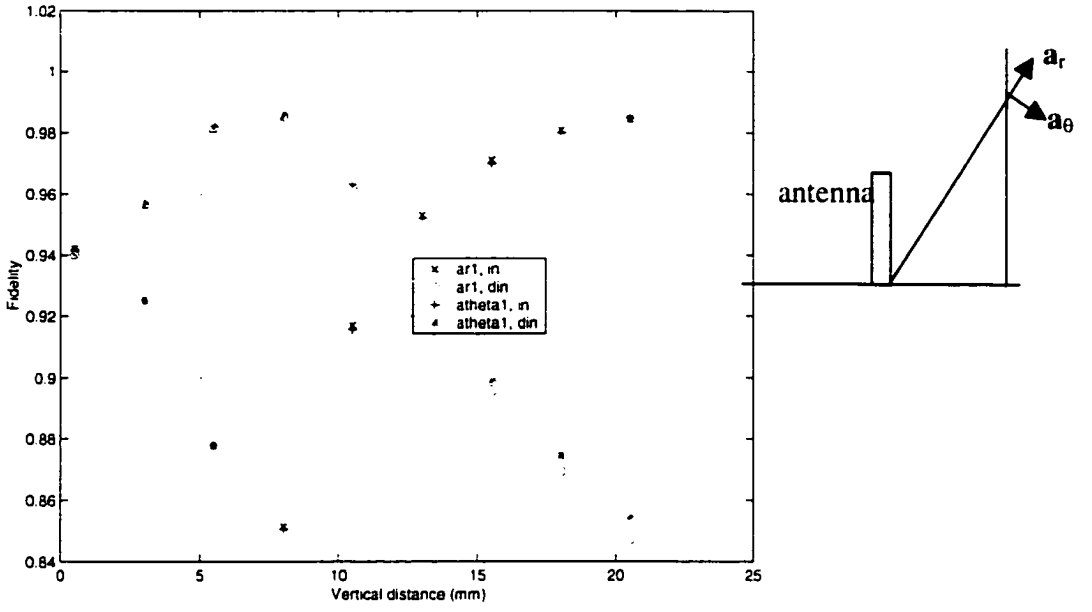

Fig. D.10. Fidelity for fields 1cm from and parallel to the bowtie.

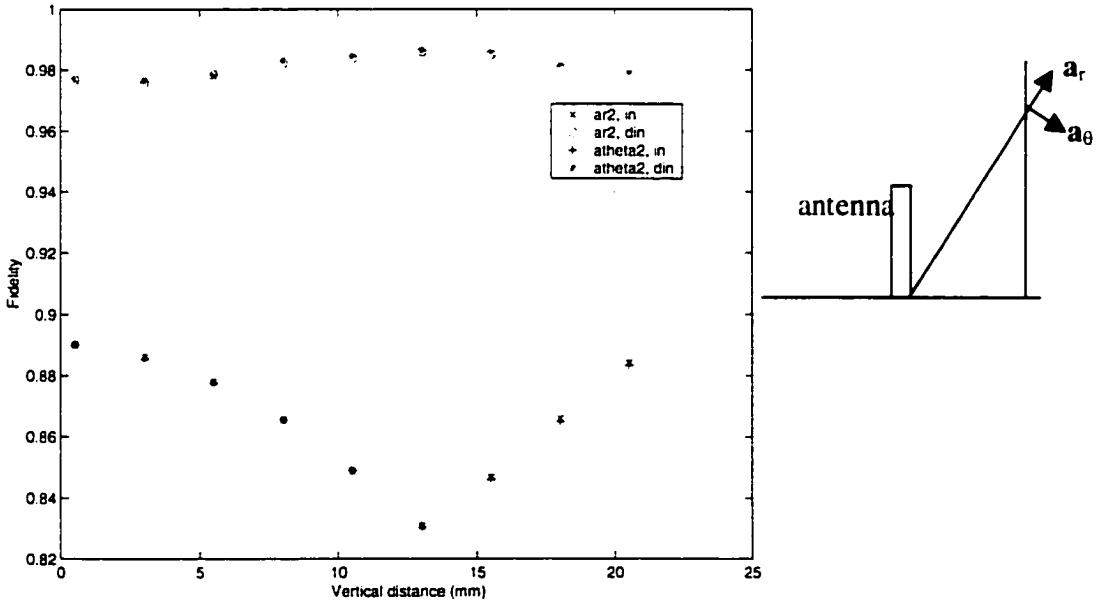

Fig. D.11. Fidelity for fields 2 cm from and parallel to the bowtie.

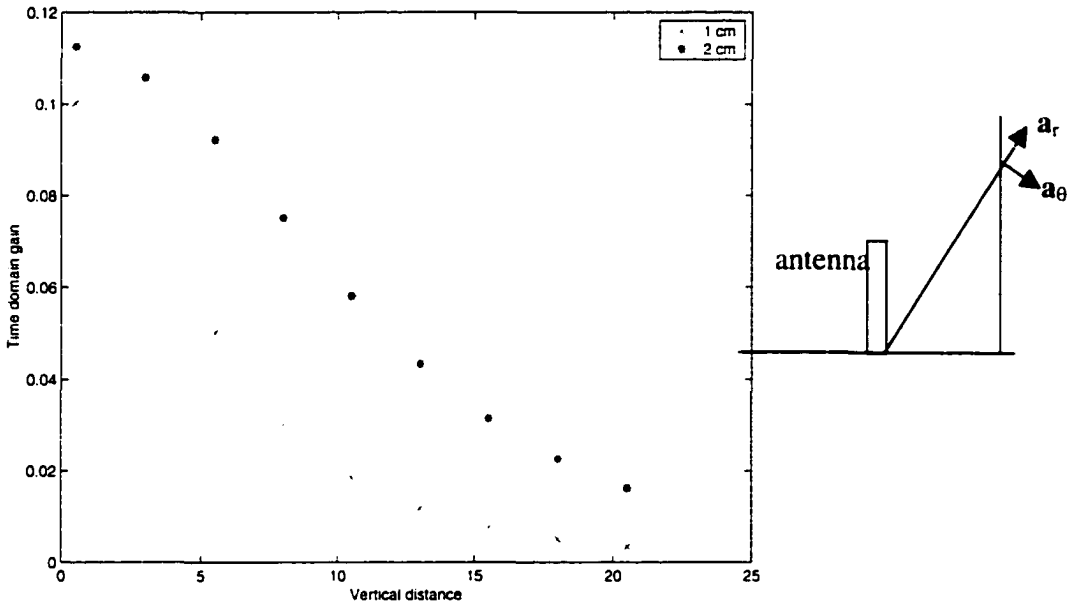

Fig. D.12. Time domain gain variation with height above the ground plane for dominant field component.

Appendix E: Statistical tests for regions of interest

To compare images, statistics are computed for regions of interest and compared with standard statistical tests [110]. The first test of interest is whether a sample distribution (g(x)) fits a distribution such as the normal distribution (F(x)). A measure of the deviation of g(x) from F(x) is required, and referred to as χ_o^2. It is assumed that this deviation has a chi-square distribution. If the observed value (χ_o^2) is less than the value computed with the chi-square distribution, this indicates a good fit to the originally proposed distribution (F(x)).

The first step in the goodness of fit test is dividing the range of pixel values into bins, with at least 5 pixels per bin. The expected number of pixels in a given bin (e_j) is computed using the distribution of interest (in this case the normal distribution). That is, the sample mean and variance are computed, used to normalize the bin range, and the proportion of the normal distribution in each normalized range (p_j) is calculated. The expected number of pixels is computed as np_j where n is the total number of pixels. The deviation between the expected (e_j) and actual distributions (b_j) is computed and normalized to the expected number:

$$\chi_o^2 = \sum_{j=1}^{n} (b_j - e_j)^2 / e_j \qquad \text{(E-1)}$$

The value of the χ^2distribution (c) that corresponds to the appropriate significance level (α) is found with:

$$P(\chi^2 \le c) = 1 - \alpha \qquad \text{(E-2)}$$

where a look-up table is used to find c for n-r-1 degrees of freedom, where n is the number of samples, and r is the number of parameters estimated (e.g. mean and standard deviation). If the computed value of χ_o^2 is less than c, then it is reasonable to assume that the values are normally distributed.

With the assumption of normalcy, the means of ROI can be compared with a Student's t-test. A hypothesis, such as the means of two regions are equal, is tested against a second

hypothesis, such as the mean of region 1 is greater than region 2. The sample means (x, y) and standard deviations (s_1, s_2) are computed for both regions. The value of the normal distribution (c) corresponding to a given significance level is determined:

$$P(T \le c) = 1 - \alpha \tag{E-3}$$

From the sample statistics, the following parameter is computed:

$$t_o = \sqrt{\frac{n_1 n_2 (n_1 + n_2 - 2)}{n_1 + n_2}} \frac{x - y}{\sqrt{(n_1 - 1)s_1^2 + (n_2 - 1)s_2^2}} \tag{E-4}$$

If t_o is less than c, then the hypothesis that the means are equal is accepted. Otherwise, the alternative hypothesis that the mean of region 1 is greater than that of region 2 is accepted.

The sample variances are compared using an F-distribution. The hypothesis that the variances are equal is tested against the hypothesis that one is larger than the other. The ratio between the sample variances (v_o) is compared to a tabulated value (c) selected for the appropriate significance level (α) and degrees of freedom (n_1-1,n_2-1):

$$P(v \le c) = 1 - \alpha \tag{E-5}$$

If v_o is less than c, then the hypothesis of equal variances is accepted.

Appendix F: Comparison of results from LC and TOTEM FDTD codes

Antenna 1 is simulated with LC and TOTEM. With LC, the antenna is modeled as a monopole. With TOTEM, the antenna is a dipole. Both problem domains have the same dimension. The LC simulation is discretized with 0.25 mm grid, while the TOEM simulation is discretized with graded mesh to provide 0.25 mm grid size near the antenna and 0.75 mm in the rest of the problem domain. The mesh differences introduce differences between the simulations, as fields are not recorded at exactly the same spatial locations. The dipole has twice the input impedance of the monopole, and this is accounted for in performance measures. For example, the source resistance in the TOTEM model is increased to 40 ohms compared to 20 ohms in LC. Both antennas are excited with 18.8 V, and the total voltages are recorded at the antenna feed (i.e. sum of excitation and reflection). Fig. F.1 shows reasonable agreement between these voltages. Error is introduced by differences in feed models. In LC, the antenna is fed by a coaxial line, which is excited by a current source. In TOTEM, the antenna is excited at its terminals with a voltage source that has internal resistance of 40 ohms. Because of the greater impedance of the dipole, approximately half the current flows when compared to the monopole. The decreased current results in smaller radiated fields. To compare fields radiated by the antennas in a reasonable manner, either the voltage or fields associated with the dipole are doubled. The field energy (z components) for both antennas is plotted in Fig. F.2, showing reasonable agreement with errors of less than 10%. The transfer functions for both antennas are compared in Fig. F.3. The TOTEM simulation shows greater attenuation of higher frequencies, perhaps due to the increased mesh size. Overall, the agreement between both techniques is reasonable. LC is used only for antenna characterization, as the visualization tools and ability to model the coaxial feed line in detail are beneficial. The comparison between LC and TOTEM demonstrates that it is reasonable to expect very similar behaviour from antennas modeled in LC and TOTEM. Therefore, antenna characterization does not need to be repeated in TOTEM and e.g. it may be assumed that the resistively loaded antenna

designed in low-loss breast tissue radiates the derivative of the excitation at a distance of 2 cm. The image reconstruction algorithms incorporate simulation results from TOTEM only. That is, additional simulations in which only a dipole antenna is present are performed in TOTEM, and are not the results of the antenna characterization (of monopoles) in LC. Therefore, the differences between results obtained with LC and TOTEM are not expected to impact on image reconstruction.

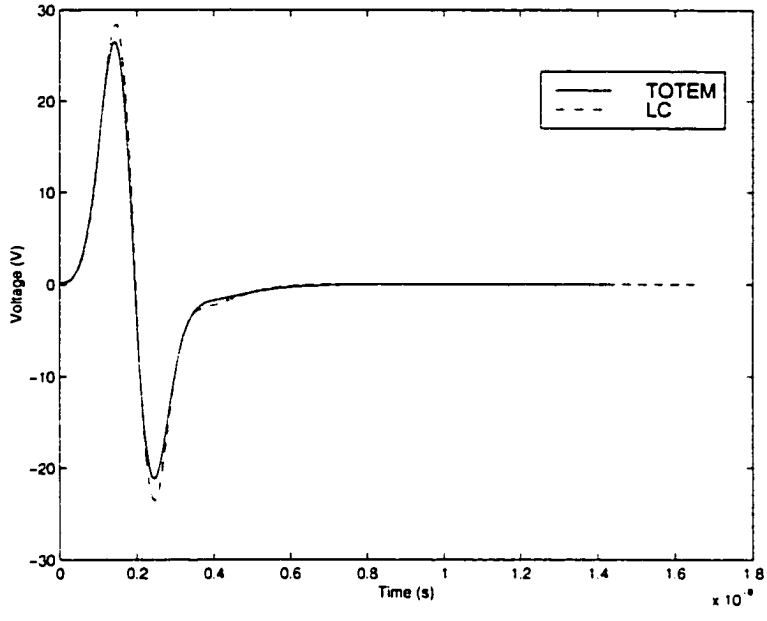

Fig. F.1. Voltages recorded at antenna feeds.

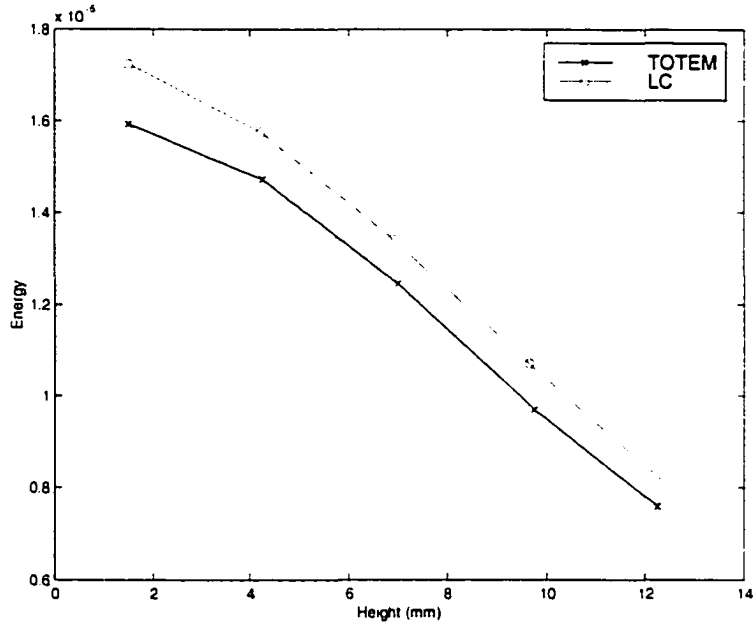

Fig. F.2. Energy variation with height above the ground plane (LC) or above position of antenna feed (TOTEM). Fields are measured at a radial distance of 2 cm from both antennas, and energy is the squared electric field summed over the observation time.

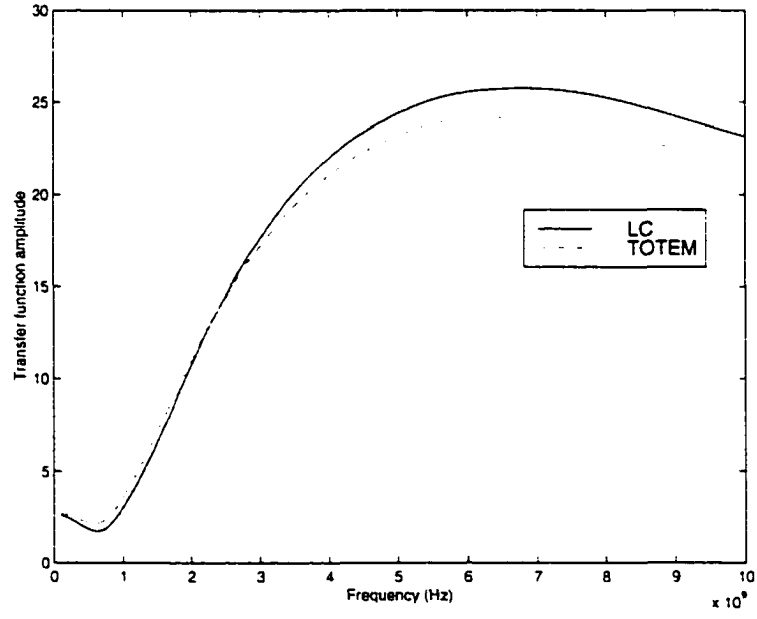

Fig. F.3. Comparison of transfer functions at 4.25 mm above the ground plane and radial distance of 2 cm from the antennas.

Appendix G: Detailed results for breast imaging

G. 1 Calibration

The initial calibration step, or subtraction of returns recorded without a breast model present, was illustrated in Chapter 5. This step helps to reduce clutter from the initial pulse, antenna reverberation, and PML reflections. However, the dominant component of the calibrated signal is the reflection from the thin layer of skin, and this reflection must be reduced to allow for tumor detection. To gain insight into the action of the first calibration step and the need for subsequent skin subtraction, the ratios between the peak-to-peak responses of the tumor and total signal are calculated as outlined in Chapter 5. The computed ratios for different immersion media and antenna-tumor distances are summarized in Table G. 1. The initial ratios illustrate the dynamic range challenges of a practical system. After the initial calibration step, the relative tumor response improves by more than 55 dB in all cases. Comparison of results for different breast models and immersion media leads to the following observations:

- Dynamic range requirements increase for a lossy immersion medium. The returns are essentially a scaled version of those recorded in the lossless case, so the same signal processing techniques are applicable.
- Initially, the relative tumor response is larger for the system immersed in liquid 1 compared to that immersed in liquid 2. The incident pulse includes reflections due to the mismatch between the feed and antenna, so this is likely due to the greater mismatch evident with antenna 2. After calibration, the relative tumor response is greater for the system immersed in liquid 2.
- In terms of clutter reduction, the most effective approach involves calibration signals recorded at each physical antenna location. The antenna impedance and reflections from PMLs change slightly with distance from the absorbing boundary conditions. However, this is an extremely computationally intensive approach, and is tested only with breast models 3 to 5.

Table G. 1 Ratio between peak-to-peak tumor and peak-to-peak total signal. The total signal is obtained by illuminating a heterogeneous breast model with antenna 1 (breast tissue) or antenna 2 (skin).

Breast model	Immersion medium	Distance from antenna (mm)		Peak-to-peak ratio Tumor to total signal (dB)	
		Tumor	Skin	Initial Signal	After calibration
2	Low-loss	50	20	-104.2	-47
4	breast	51	10	-109.85	-57.7
4		40	10	-99.6	-48
4	Lossy breast	51	10	-115.37	-57.6
4	Low-loss skin	36	6	-100.71	-44.4

G.2 Skin subtraction

Two approaches to skin subtraction are described in Chapter 5. In this section, the robustness of the phantom method to differences between the phantom and breast model is evaluated. Specifically, changes in shape, size and material properties are investigated. The averaging method is investigated for breast models with tumors at the center, as well as with different numbers of returns used to calculate the average response. Finally, applying each method to three models provides a more specific comparison of the phantom and averaging methods.

G.2.1 Phantom approach

In Chapter 5, the phantom skin subtraction algorithm is demonstrated with breast model 2 and a similarly sized and located skin phantom. Actual breast shapes, sizes and electrical properties are expected to differ from the skin phantoms. The robustness of the phantom skin subtraction algorithm to changes in these parameters is investigated by comparing the total energy and peak signals, before and after skin subtraction. The error resulting from use of cylindrical skin phantoms in approximating reflections from differently shaped and sized breast models is investigated in Table G. 2. Table G. 3 compares results obtained with skin thickness ranging from 1 to 2.5 mm. The impact of the mismatch in electrical properties of the breast and skin cylinder is summarized in Table G. 4. Overall, the results in Table G. 2 to Table G. 4 show that, despite its simplicity, the phantom skin subtraction method is quite robust when applied to systems immersed in

low-loss breast tissue. Even with variations in shapes and sizes of the breast model and skin phantoms, several skin thickness and different electrical properties, reflections from the skin are significantly reduced.

Table G. 2 Performance of skin subtraction algorithm with mismatches in geometries (values in brackets give the nominal dimension). The voltage ratio compares the peak-to-peak voltages before and after skin subtraction. The height of the breast models and cylinders is 7 cm. Variations on breast model 2 are illuminated with antenna 1.

Breast Model Diameter (cm)	Skin cylinder		Location (cm)	Thickness (mm)	Energy Remaining (%)	Voltage Ratio (dB)
	Diameter (cm)	Distance to antenna (cm)				
6	6	2	2.18 (2)	2.1 (2)	0.3	-28
6	10	3	2.24 (2)	2.1 (2)	1	-21
2 of 6 (overlapping)	6	2	2.31 (2)	3.2 (2)	0.75	-22
6 to 4 (conical)	6	2	2.56 (2)	2 (2)	0.2	-30

Table G. 3 Performance of skin subtraction algorithm with variations in skin thickness (values in brackets give the nominal dimension). Breast model 1 is illuminated with antenna 1. The skin phantom height is 4 cm and diameter is 10 cm.

Location (cm)	Thickness (mm)	Energy Remaining (%)	Voltage Ratio (dB)
3.08 (2.95)	2.6 (2.5)	1.6	-18
3.12 (3)	2.1 (2)	1.2	-21
3.13 (3.05)	2 (1.5)	2.3	-18
3.16 (3.1)	1.9 (1)	4	-15

Table G. 4 Performance of skin subtraction with various electrical properties of breast tissue. Breast model 2 is illuminated with antenna 1. The skin cylinder has diameter 6 cm, ε_r=36, σ=4 S/m and is located 2 cm from the antenna.

Breast model		Location (cm)	Thickness (mm)	Energy Remaining (%)	Voltage Ratio (dB)
Relative Permittivity	Conductivity (S/m)				
36	4	2.18 (2)	2.1 (2)	0.3	-28
36	5	2.19 (2)	2.1 (2)	1	-28
36	3	2.17 (2)	2.1 (2)	0.75	-26
30	4	2.18 (2)	2 (2)	0.2	-28
30	5	2.19 (2)	2 (2)	0.2	-19

The phantom skin subtraction algorithm is also evaluated for systems immersed in liquid 2. These systems are of interest due to the improved antenna performance (e.g. time-domain gain as shown in Chapter 4). As shown in Chapter 5, the reflections from the skin-breast interface are also expected to be smaller, allowing for greater transmission of energy into the breast. Returns are computed for two phantoms: a lossy skin cylinder immersed in low-loss skin, and a breast tissue cylinder immersed in low-loss skin. After subtraction, the peak-to-peak voltage is 6.4% and the energy 0.7% of the original signal. Although this approach appears effective for immersion in liquid 2, two additional simulations are required. This motivated the development of an algorithm that requires less *a priori* information and is applicable to both systems without modifications.

G.2.2 Averaging method

The results of two approaches to the averaging technique are compared for breast model 2 with a 6-mm diameter tumor located at the center and equidistant from all antennas. With the windowing approach, the average is subtracted over a segment of the signal with magnitude greater than 5% of the maximum value of the signal. Without a window, the average is subtracted over the entire signal. Results of the two approaches are presented in Fig. G.1, along with the calibrated signal. Without a window, the skin reflection is more effectively reduced. However, the tumor is at the center of the model and its response is eliminated without windowing. The tumor response at a single antenna, the average tumor response and the results of subtracting these two signals are shown in Fig. G.2, clearly demonstrating the annihilation of the tumor response. In reality, tumors are not likely to be located in the center of the breast. Fig. G.3 shows the tumor response and signal subtracted with averaging for breast model 2 with a 4-mm diameter tumor located 14 mm from the breast model center. In this case, the averaging approach has limited influence on the tumor response. Therefore, annihilation of the tumor response is only a concern in cases where the tumor is located at the breast center. This is mitigated by applying the average over a window. Otherwise, the averaging approach preserves the tumor response.

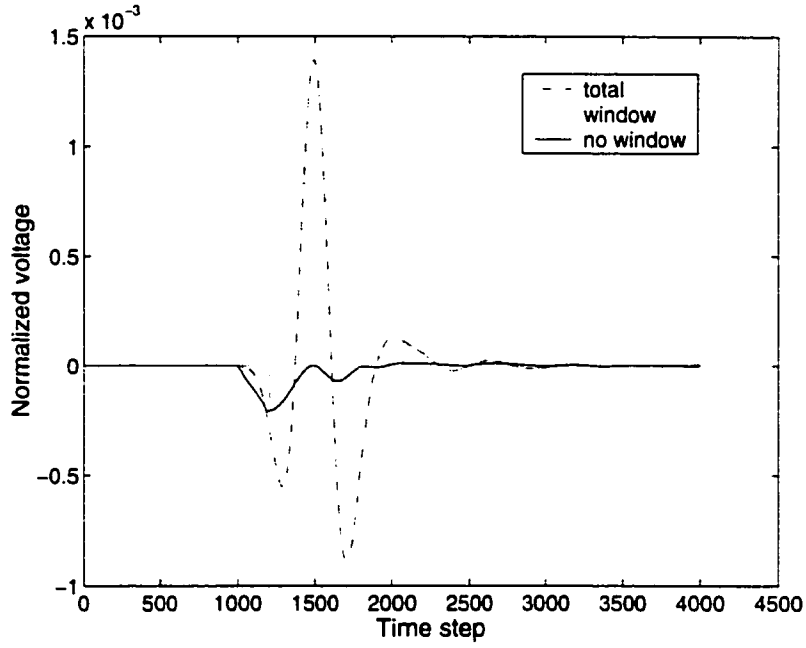

Fig. G.1. Signals before and after application of the averaging approach to skin subtraction. Results with and without a window are presented.

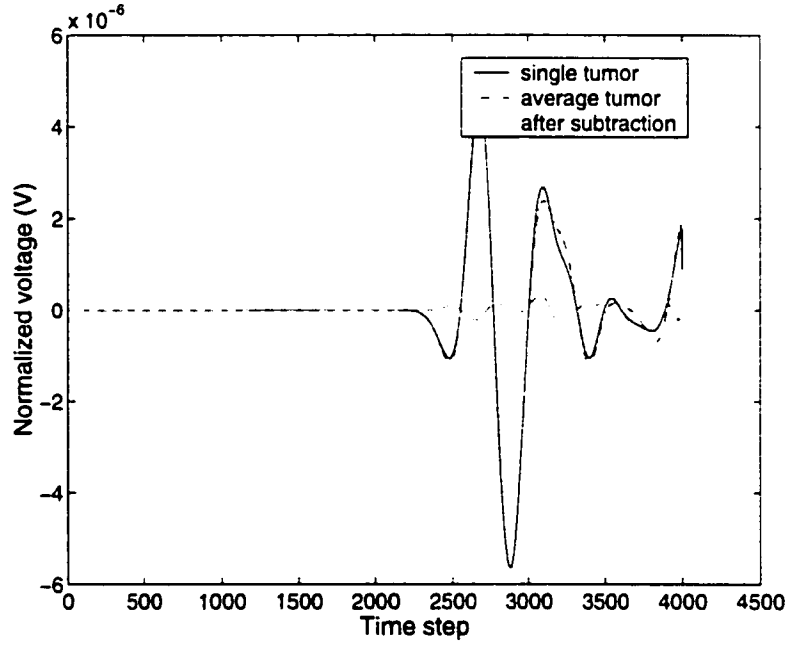

Fig. G.2. Tumor response, average tumor response, and result of subtracting the two responses. Results are presented for breast model 2 with 6-mm diameter tumor at the center.

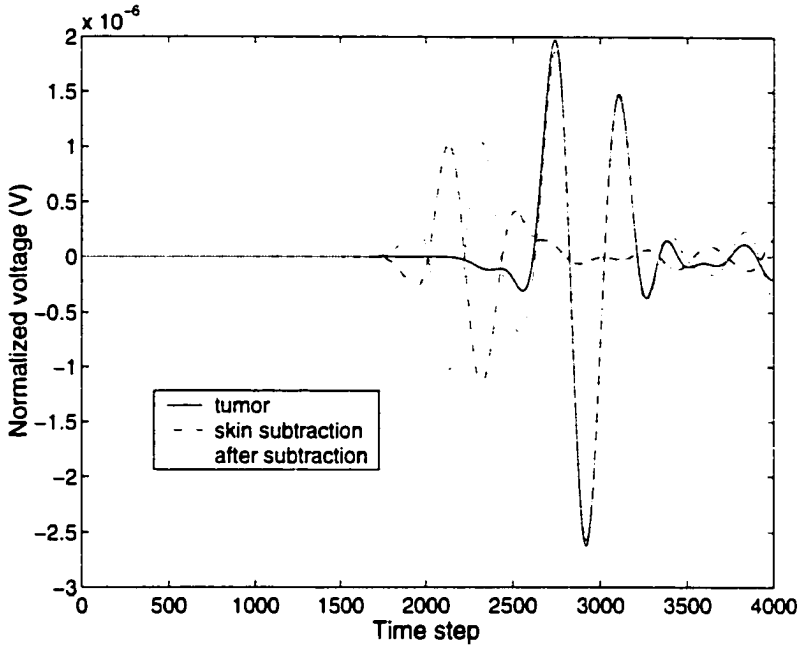

Fig. G.3. Tumor response and average tumor response for skin subtraction. Results correspond to breast model 2 with a 4-mm diameter located 14 mm from the center.

To compute the results summarized in Fig. G.1 to Fig. G.3, responses recorded at 30 antenna locations are used. The influence of using fewer signals to compute the average response is explored. For breast model 2 with a 6-mm diameter tumor at the center, the average response is computed using windowing and 5 to 30 antennas. The peak-to-peak isolated tumor response is compared to the peak-to-peak total signal at the same 5 antennas (Table G. 5). Similar peak-to-peak ratios are obtained in all cases, indicating that the number of antennas used to compute the average signal has limited influence on the effectiveness. However, the test case is a simple cylindrical model. A greater number of antennas may be more effective for realistic breast models with variations in shape.

Table G. 5 Minimum, maximum and mean peak-to-peak values calculated at 5 antennas after skin subtraction. 5 to 30 signals are used to calculate the average response.

	Number of signals			
Peak-to-peak (dB)	30	15	10	5
Minimum	-22.9	-22.9	-22.9	-22.9
Maximum	-31.1	-31.0	-31.8	-31.2
Mean	-27.4	-27.6	-27.8	-27.7

The averaging approach is applied to signals recorded for breast model 4 with two different immersion media. Results are compared for tumors located 30 mm beneath the skin, and antennas located 1 cm (liquid 1) or 0.6 cm (liquid 2) from the skin. In both cases, the average response is computed with 10 calibrated returns. After skin subtraction, the peak-to-peak ratio between the tumor and total signal is -20.1 dB (liquid 1) and -14 dB (liquid 2). As shown in Table G. 1, the ratios after calibration are -48 dB and -44.4 dB, respectively. Therefore, the averaging method of skin subtraction is effective in both cases, and maintains the larger relative tumor response observed in liquid 2.

G.2.3 Comparison of skin subtraction methods

The previous two sections have examined the robustness of the algorithms with respect to changes in various parameters. The skin subtraction methods are now compared on the same three models: breast model 2 with a 6 mm diameter tumor at the center; breast model 4 with a 6 mm diameter tumor located 6 mm from the center; and the realistic breast model. For the first model, Table G. 6 compares the peak-to-peak ratios between the tumor response and total signal, as well as the energy remaining in the signal after subtraction. Both measures show the slight advantage of the averaging approach. For the second model, Table G. 7 summarizes the peak-to-peak and energy ratios. Again, the averaging method provides performance advantages. The skin subtraction algorithms are compared graphically for the realistic breast model. Fig. G.4 shows the reflection from the breast model, similarly shaped skin phantom, and the remainder. Fig. G.5 shows the

phantom signal after scaling and time shifting to fit the remainder. The reflection from the breast model and average response of 8 antennas are shown in Fig. G.6. The averaging approach provides a much better approximation to the breast model reflection at reduced computational cost when compared to the skin phantom approach.

Table G. 6 Results for breast model 2 with 6-mm diameter tumor located at center. The phantom method uses a 6 cm diameter skin phantom located 2 cm from the antenna. Signals at 30 antennas are used to determine the average response. The peak-to-peak ratio compares the tumor response and total signal. Total energy after skin subtraction is compared to the energy in the signal after calibration.

	Peak-to-peak ratios (dB)				Energy ratio (%)	
	Initial	Calibration	Phantom	Averaging	Phantom	Averaging
Maximum	-104.7	-46.2	-29.8	-22.9	2.5	0.25
Minimum	-103.0	-47.7	-35.7	-32.1	16.7	6.6
Mean	-104	-47	-32.3	-28.5	7.1	2.4

Table G. 7 Results for breast model 4 with a 6-mm diameter tumor located 6 mm from the center. The phantom method uses a skin phantom with 6 cm diameter and located 1 cm from the antenna. Responses at 10 antennas are averaged to find the skin subtraction signal. The peak-to-peak ratio compares the tumor response and total signal. Total energy after skin subtraction is compared to the energy in the signal after calibration.

	Peak-to-peak ratios (dB)		Energy ratio (%)	
	Phantom	Averaging	Phantom	Averaging
Maximum	-26.2	-17.7	1	1.34
Minimum	-36.2	-36.1	0.7	0.06
Mean	-30.8	-28.4	0.8	0.6

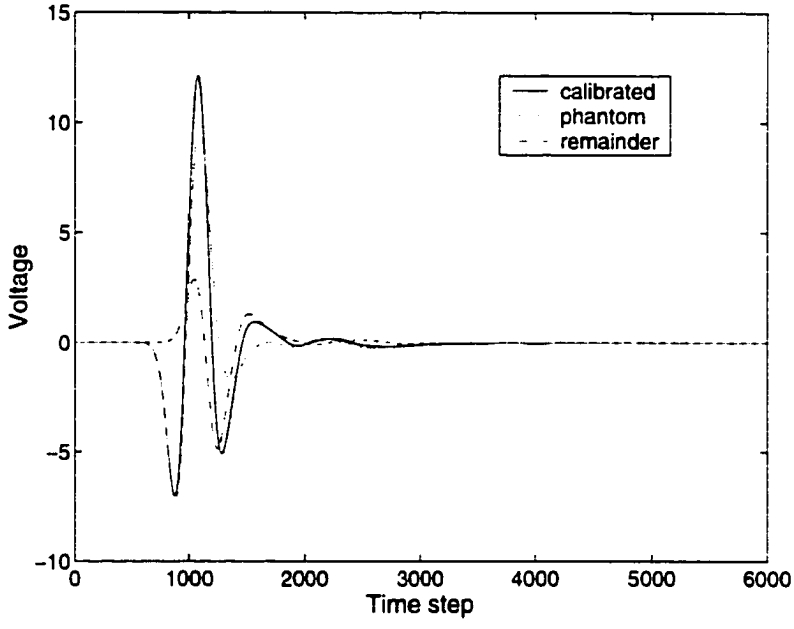

Fig. G.4. Reflections from realistic breast model, similarly shaped skin phantom, and the difference between these two signals.

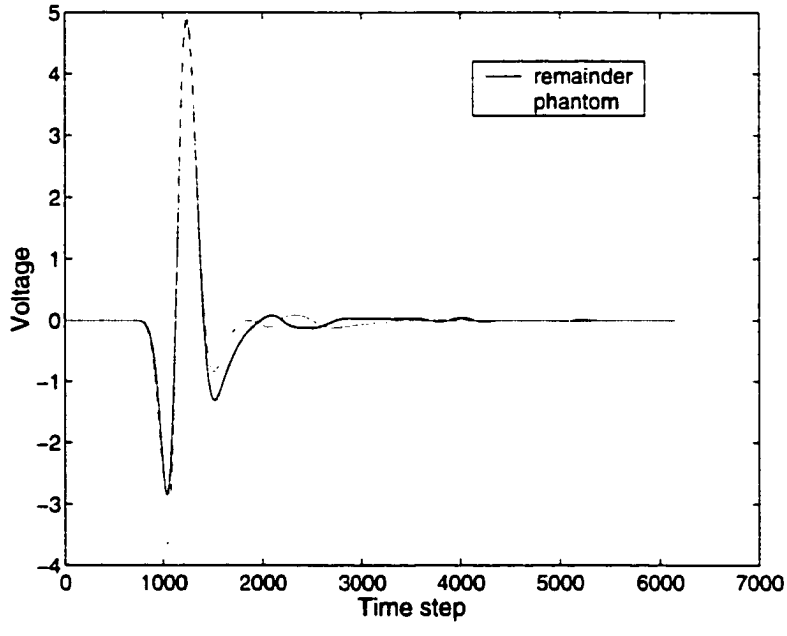

Fig. G.5. Remainder from Fig. G.4, and skin phantom reflection fit to this data.

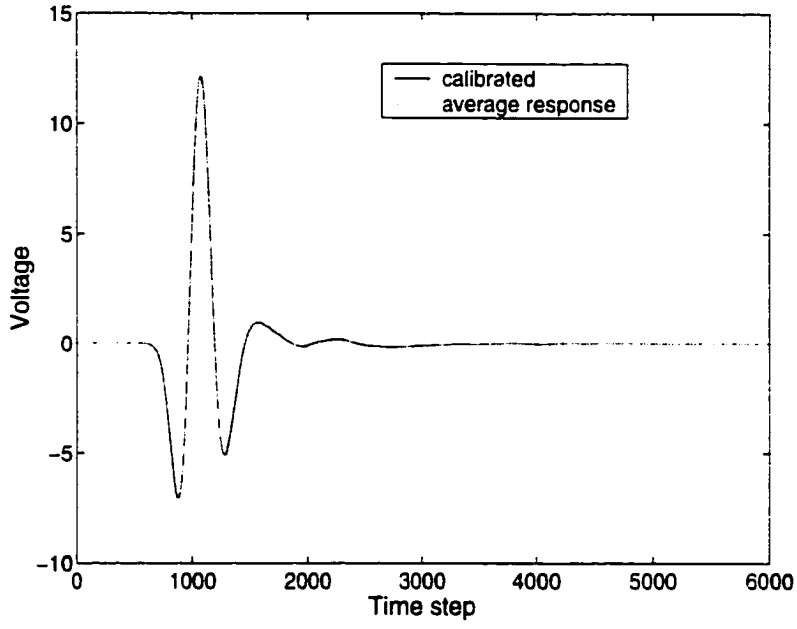

Fig. G.6. Reflection from realistic breast model and average response recorded at 8 antennas.

Both methods of skin subtraction are effective for simple breast models. In initial work with image reconstruction, the skin phantom approach is used. While the averaging approach provides a slight advantage for simple cylindrical models, this is not significant for e.g. feasibility testing of tumor detection with 2D models. For more complex models (including those in which the tumor is not located at the center) and for localization in 3D, the averaging approach is utilized. For an array of antennas that encircles the breast, both skin subtraction algorithms provide an indication of the breast contour. This may be used to apply a time gate to the signal in order to remove reflections from the opposite skin interface, as well as to define limits for image display in order to remove clutter occurring outside of the breast.

G. 3 Return enhancement

After calibration and skin subtraction, clutter is significantly reduced. The next signal processing step, return enhancement, focuses on selective enhancement of the tumor response. Two methods of return enhancement are compared, namely correlation to a reference signal and integration. First, the action of correlation and integration on the isolated tumor response is examined. By comparing the peak-to-peak tumor response to

the peak-to-peak total signal, the impact of each method is better understood. Finally, the robustness of both methods to different tumor shapes is examined.

The isolated tumor response and the reference signal for correlation (derivative of the incident pulse) are shown in Fig. G.7. The results of correlation and integration are shown in Fig. G.8 and Fig. G.9, respectively. The enhanced tumor responses have dominant peaks and significant side lobes. Therefore, both methods appear to have similar actions on the tumor response, with integration resulting in lower sidelobes.

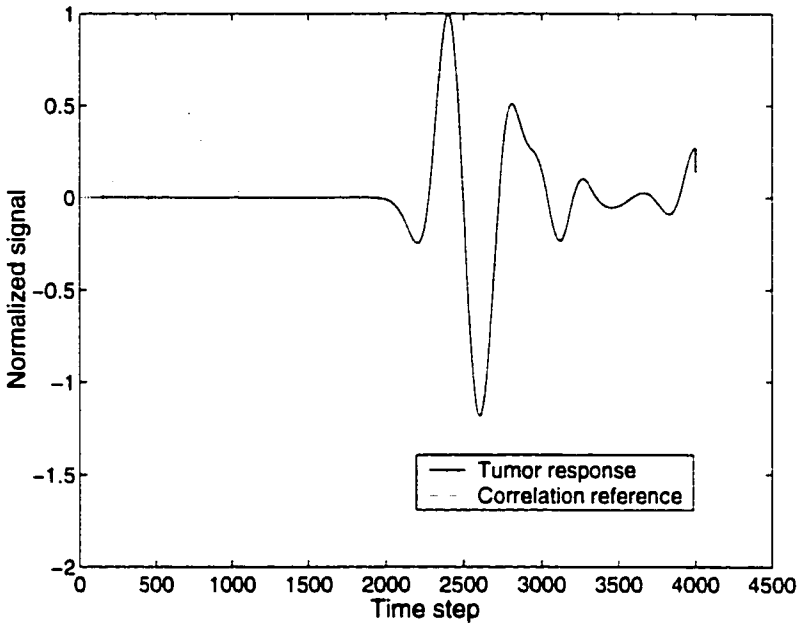

Fig. G.7. Isolated tumor response and reference signal for correlation. The reference signal is the derivative of the signal recorded at the antenna without a breast model present.

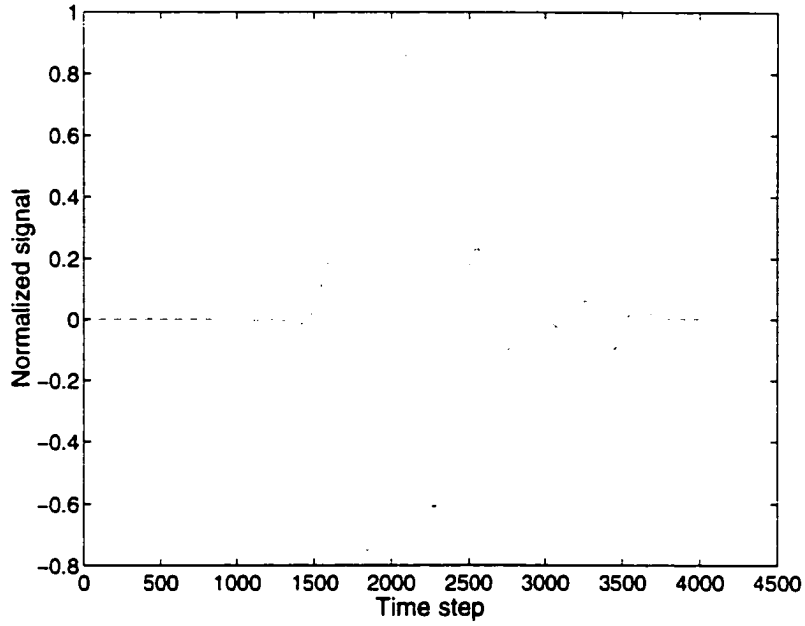

Fig. G.8. Tumor response after correlation to the reference signal.

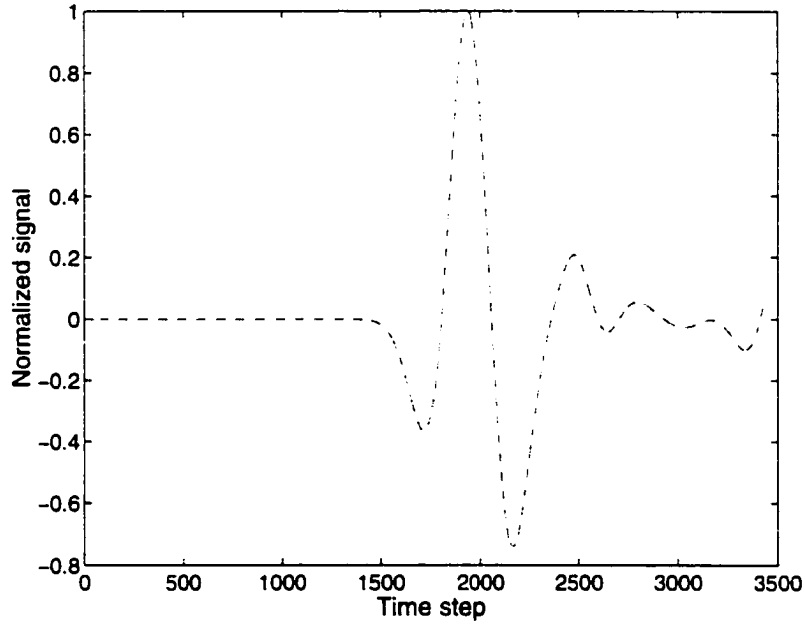

Fig. G.9. Tumor response after integration.

To give insight into the influence of these processes on the total signal, ratios between the peak-to-peak tumor response and total signal are compared Table G. 8. For both the tumor and total signal, the peak-to-peak values are calculated after return enhancement. The results in Table G. 8 suggest that integration enhances clutter as well as the tumor

response, as the peak-to-peak ratios are fairly consistently smaller than those calculated with correlation. Both methods maintain the improved peak-to-peak ratios observed for the system immersed in liquid 2.

Table G. 8 Ratio between peak-to-peak values of tumor and total signal. Peak-to-peak values are calculated after correlation or integration. The averaging skin subtraction method uses returns at 30 antennas to calculate the average response.

Breast model	Immersion media	Skin subtraction Method	Result	Correlation	Integration
2	Breast tissue	Phantom	• Single signal (equidistant antennas)	-29.1	-32.8
		Averaging	• Single signal	-25.3	-34.2
4	Breast tissue	Averaging	• Mean of 30 • Minimum of 30 • Maximum of 30 • Antenna 4 cm from tumor	-21.9 -31.6 -15.75 -17.3	-23.8 -29.24 -19.7 -23
4	Skin	Averaging	• Antenna 3.6 cm from tumor	-11.5	-15.9

G.4 Compensation

After calibration, skin subtraction and return enhancement, compensation may be applied to the signals to correct for attenuation due to path loss and radial spreading. To evaluate the effect of compensation, the peak-to-peak tumor response is compared to the peak-to-peak total signal. This comparison is made after calibration, skin subtraction with averaging, integration and the specified compensation. Path loss compensation is applied after a time delay corresponding to the estimated skin location. Table G. 9 compares results for two immersion liquids and antennas located at equivalent distances from the tumor. For both cases, radial spreading compensation is most effective for tumor enhancement, and incorporation of path loss degrades the results. One reason for this is the enhancement of late arrival time clutter resulting from the exponential model used to estimate path loss. Similarly, clutter from sources outside of the breast and arriving after the application of path loss compensation is unrealistically enhanced. The larger relative tumor response observed with immersion liquid 2 is not preserved, because of enhancement of clutter near the tumor.

Table G. 9 Results of applying various types of compensation to returns from breast model 4 with the tumor 3 cm below the skin.

Immersion liquid	After integration	Radial spreading	Path loss	Radial spreading and path loss
Liquid 1	-23	-7.0	-10.7	-8.65
Liquid 2	-15.9	-9.1	-10.5	-11.8

Compensation is applied after return enhancement, however it could be placed earlier in the signal processing sequence. As a test, radial spreading compensation is applied after skin subtraction and before return enhancement. For the model immersed in liquid 1, the ratio of peak-to-peak tumor and total signal is −10 dB after compensation, -9.4 dB after correlation, and −12.7 dB after integration. Better results are achieved by applying compensation after return enhancement, as less clutter enhancement occurs.

G. 5 Detection of 2D tumors

Breast models 1 and 2 contain long cylindrical tumors that provide greater returns than spherical tumors. Therefore, breast models 1 and 2 allow for initial evaluation of the feasibility of tumor detection and the impact of the number and configuration of antennas.

Breast model 1 contains a 5 mm diameter tumor at a minimum depth of 12.5 mm below the skin. The antenna positioning is shown in Figure 5-7, and consists of 8 antennas located 3 cm from the skin and spaced by 1 cm. The image reconstruction algorithms described in Table 5-8 are applied, with the phantom skin subtraction method incorporating returns from a similarly sized and located skin cylinder. The image is presented in Fig. G.10, and the tumor response is evident and has a maximum at (x=81 mm, y=42 mm). This is in good agreement with the physical location of the tumor (x=80 mm,y=45 mm).

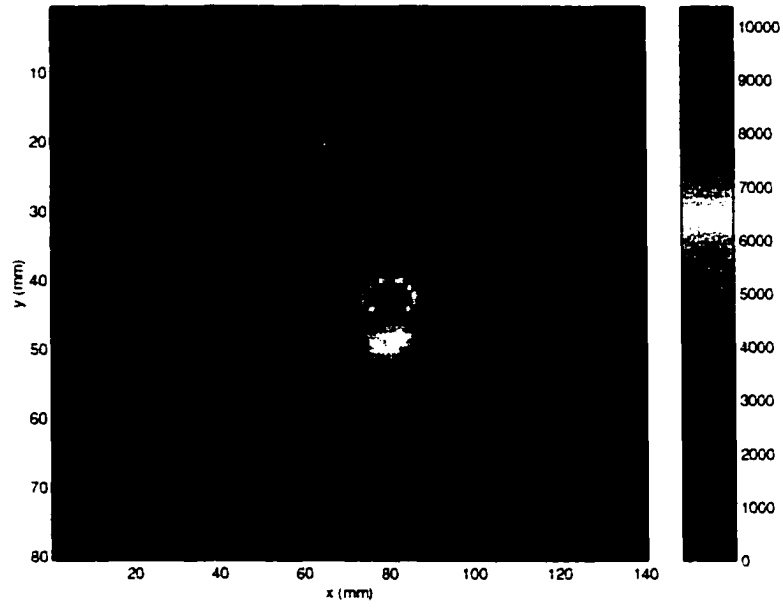

Fig. G.10. Image of breast model 1. The tumor response is located at (x=81, y=42) and has FWHM size of 142 pixels.

The influences of antenna position, array sizes and spacing are examined with breast model 1. A 4 mm diameter tumor is located at a minimum distance of 2 cm below the skin surface, and up to 15 antennas are located at distances varying between 2 and 3 cm from the skin. Three arrays are created from subsets of the 15 antennas, as described in Chapter 5. Table G. 10 summarizes tumor responses obtained with the three arrays. Results indicate that successful detection of tumors is achieved with antennas located non-uniform distances from the breast model. As expected, more of the breast is imaged with 15 antennas distributed on a larger arc. If the tumor location is unknown, then encircling the whole breast provides a scan. If *a priori* information is available on the location of suspicious areas, the formation of images with localized arrays may be preferred, as much larger detection ratios are achieved. A larger detection ratio is achieved with more elements (decreased spacing) spanning the same arc.

Table G. 10 Tumor response with various antenna arrays. The FWHM tumor response and maximum tumor response location (actual location is x=98, y=46) are provided. The detection ratio is the ratio between the means of the FWHM tumor response and a region in the image away from the tumor (x=40 to 60, y=40 to 50).

Number of Antennas	Antenna Spacing (cm)	Maximum Response Location X (mm)	Y (mm)	Tumor Size (mm^2)	Detection Ratio
15	1	96	49	116	2.6
7	1	96	49	106	18
13	0.5	96	49	127	25

G. 6 Detection of spherical tumors: Homogeneous models

The results (presented in Chapter 5) obtained with the heterogeneous model and spherical tumors demonstrate the feasibility of tumor detection in a 2D cross-section with either skin subtraction method. Next, results obtained with heterogeneous and homogeneous models are compared. The homogeneous breast model is symmetric, so the returns at one antenna position are used to represent the returns recorded at the 30 antenna locations examined in the heterogeneous case. This is a great saving in computational effort. To gain insight into the differences between single signals, the ratio between the peak-to-peak tumor response and total signal is computed after calibration and after skin subtraction for both models. The phantom skin subtraction method is selected for use in this section. After calibration, the ratio is –47.8 dB and –48 dB for the homogeneous and heterogeneous models, respectively. The ratios increase to –21.8 dB and -23.2 dB after skin subtraction. Therefore, the relative tumor response is slightly larger with the homogeneous model, as expected. Images of both models are reconstructed with various numbers of antennas, and tumors are easily detected by visual inspection in all images. Statistics for the images are computed for the ROI indicated in Chapter 5, Figure 5-27 and summarized in Table G. 11. A larger difference between the maximum tumor value and the mean of the interior ROI, plus a smaller standard deviation in the interior ROI indicate improved detection. For the heterogeneous model, the maximum of the tumor response increases with fewer antennas, however the FWHM tumor area decreases, and the mean and standard deviation of the interior ROI both increase. With the homogeneous model, there is a lesser change in the standard deviation and tumor area

with fewer antennas. Additionally, the ratios between the means of the FWHM tumor response and interior ROI are much larger than for the heterogeneous model. Studies using homogeneous models likely provide optimistic results, however allow for rapid reconstruction of images and testing of algorithms.

Table G. 11 Statistics computed for ROIs of various images. Model A is a heterogeneous version of breast model 2. Model B is a homogeneous version of breast model 2. The breast interior ROI contains 231 pixels.

Model	Antennas	Interior Mean (*1000)	Interior Standard Deviation	Tumor Max (*1000)	FWHM Tumor Mean (*1000)	FWHM Tumor Pixels
A	30	2.1	432	3.79	2.7	56
A	15	2.1	600	4.07	2.9	52
A	10	2.5	787	4.62	3.7	44
B	30	1.9	696	5.8	4.3	47
B	15	1.9	787	6.02	4.4	46
B	10	2.2	600	5.96	4.4	47

G. 7 Detection of spherical tumors: smaller tumors

An initial study on the detection of smaller tumors is performed with the homogeneous model. Tumors of diameters 2 and 4 mm are located at the center of the breast model. After calibration, the peak-to-peak ratios between the tumor and total signal are –53.7 dB and –67.9 dB for the 4 and 2 mm tumors, respectively. After phantom skin subtraction, the ratios improve to –23.6 dB and –37.9 dB. Table G. 12 compares statistics for images of breast models with and without tumors. The maximum and mean of the tumor response decrease as the tumor size decreases, as expected. However even without a tumor present, a significant response is evident at the center of the breast. To gain insight into the cause of this "ghost" tumor, an image of a tumor-free heterogeneous model is also reconstructed. Statistics for and visual inspection of this image do not indicate the presence of a tumor. Further investigation suggested that the "ghost" tumor resulted from reflections at the ends of the cylinder which are further enhanced with the use of the same signal to represent all returns. Embedding the ends of the cylinder into the PMLs mitigates this.

Table G. 12 Response of tumors of smaller sizes in images. Breast models are the same as in the previous table, and 15 antennas are used to reconstruct images.

Model	Tumor Diameter (mm)	Interior Mean (*1000)	Tumor Max (*1000)	FWHM Tumor Mean (*1000)	Pixels
B	6	1.9	6.02	4.4	46
	4	1.8	4.93	3.6	49
	2	1.75	3.9	2.9	57
	-	1.74	3.77	2.76	60
A	6	2.1	4.07	2.9	52
	-	1.9	2.35	1.7	56

G.8 Initial feasibility study of localization in 3D

To test the feasibility of localizing the tumor response in 3D, a variation of breast model 4 is used. The breast model 3 consists of an infinite cylinder with 2D random variations in the breast tissue electrical properties (Chapter 5, Figure 5-4). The following procedure is used to synthesize data:

- Returns are recorded for breast models with and without tumors at z=a.
- The breast model does not change along the z-axis, so returns from a tumor-free breast model at z=b are represented by those recorded at z=a.
- The tumor response varies as the antenna is moved along the z-axis. The antenna located at (x0,y0) is scanned past the tumor, and the change in the tumor response is examined at each vertical position.
- The tumor response at each antenna is isolated for z=a. The isolated tumor response is estimated for all antennas located at z=b, c, ... by time shifting and scaling according to observations made at the physically scanned antenna.
- Data are synthesized at z=b, c, ... by adding the returns from the tumor-free breast model and the estimated tumor response at z=b, c, ...

To ensure that the synthesized data set is a reasonable approximation of simulated data, several tests are applied. First, returns from a tumor-free breast model at z=a and z=b are compared. Next, the change in response as the antenna is scanned past the tumor is

examined and a model for transforming the response at z=a to z=b, c, ... is developed. Both isolated tumor response and total signals are synthesized for z=b, and compared to simulated data. The entire synthesized data set is then used to reconstruct images.

The recorded returns at 30 antennas encircling a tumor-free breast model are compared for z=40 mm and z=42 mm. Before skin subtraction, differences more than 60 dB below reflections from the skin are observed. These differences result from changes in reflections from the absorbing boundaries, as these reflections change with antenna-boundary distances. The averaging skin subtraction method is applied to signals recorded at the same vertical antenna location. The differences in signals recorded at 2 antenna heights after skin subtraction are more than 75 dB below reflections from the skin. Therefore, the returns at z=a reasonably represent returns at z=b after the averaging method reduces reflections from common sources.

The returns from the tumor-free breast model are combined with the estimated tumor response to synthesize the data. Estimating the tumor response involves approximating changes in time delay and amplitude with change in vertical location. To estimate the time delay, tumor responses at 30 antennas positioned at z=40 mm are compared to responses at the same array positioned at z=42 mm. The best results are achieved by combining the time delays computed for z=40 mm with the calculated time delay corresponding to the changes in height. For data recorded with the antenna feed at z=42 and all 30 locations, this approaches gives a maximum error (compared to computed data) of 1 time step. To estimate the changes in amplitude of the tumor response as the antenna array is translated vertically, the changes in tumor response as one antenna moves along the z-axis are computed. The changes in voltages recorded at the (x=115, y=50) antenna are examined as the antenna feed is scanned from z=40 mm to z=50 mm in 2 mm increments. The ratio between the maximum tumor response at each vertical location and the z=40 mm position is calculated. The amplitudes of the tumor responses at z=42 mm are predicted by scaling the response at z=40 mm by the appropriate ratio, resulting in a mean error of less than 0.5%.

Therefore, the tumor response at 30 antenna locations is needed to form a basis for estimating data as the antennas are scanned past the tumor. These base responses are necessary, as the breast tissue is heterogeneous and the magnitude and locations of the tumor responses cannot be accurately predicted from the returns recorded at one antenna location. The incremental time delay resulting from scanning the antenna is calculated with the known vertical displacement. The change in amplitude is determined by simulating one antenna at the desired vertical location, and taking the ratio between the maximum amplitudes at the desired and original locations.

Comparing synthesized and computed results for antenna locations not involved in data synthesis tests the approximations. The differences in synthesized and computed signals are calculated for antennas at z=44, 46, 48 and 50 mm. The difference signal has less than 3% of total energy of the computed tumor response. The differences between the total computed and synthesized signals are also calculated. These difference signals contain less than 1% of the total energy in the computed signal. Therefore, the synthesized data appear to be reasonable approximations of the computed data.

Data are synthesized for an array consisting of 30 antennas at each vertical position, and vertical locations ranging from z=24 to 56 mm in 2 mm increments. To determine whether the tumor response is localized in 3D, an image of the plane passing through the tumor and along the cylinder axis is reconstructed and shown in Fig. G.11. This image demonstrates the successful localization of the tumor response in 3D. Asymmetries are due to the addition of clutter to the tumor response.

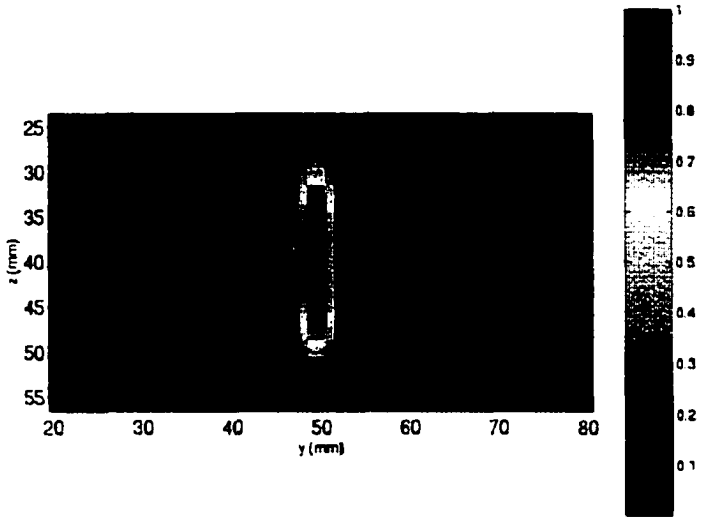

Fig. G.11. Image of tumor response reconstructed with synthesized data for 9 rows of 30 antennas. The array is centered on the tumor location (z=40 mm) and rows are spaced by 2 mm. The image is reconstructed with calibration at each antenna location, averaging skin subtraction, and correlation. The squared pixel values are displayed.

To provide insight into the number of antennas required for reliable localization in 3D. images of the planes passing through the tumor and cylinder axis were reconstructed with various arrays. The maximum signal and clutter values for the images are calculated and summarized Table G. 13. From these results, it appears that vertical antenna spacing of 6 mm spanning 30 mm and 10 antennas per vertical elevation is sufficient for detection of the 6-mm diameter tumor at minimum depth of 3 cm. The spacing intuitively makes sense, as the antenna is 12.5 mm long and it is therefore overlapping by only a small amount with the previous location when the feed is moved by 6 mm.

Table G. 13 Maximum signal-to-clutter ratio computed for various antenna arrays.

Antenna span	Antenna spacing	Number of antennas per row	S/C ratio (dB)
32	2	30	11.8
32	2	15	6.0
32	4	15	6.4
30	6	10	6.9

Summary

In this section, successful localization of the tumor response in 3D is demonstrated with synthesized data. Images are reconstructed with various numbers of antennas in order to provide insight into the array sizes required for detection. In the next section, this information is applied to localization of tumor response in a breast model with 3D heterogeneities.

G. 9 Tumor localization in 3D: correlation vs. Integration

The previous section demonstrated the feasibility of localizing tumor responses in 3D with synthesized data. In this section, tumor responses are localized in breast model 4, which contains 3D heterogeneities. As an initial test of image reconstruction algorithms for 3D localization, images are reconstructed for a plane passing through the tumor and along the axis of the cylinder. The y-z plane at x=64 mm is selected, returns recorded at 5 rows of 10 antennas are used, and the extent of the reconstruction region corresponds to the physical span of the array. The results are presented in Fig. G.12 and Fig. G.13, indicating the successful localization of the tumor response in 3D. Similar to the observations in G.3, correlation results in the presence of "sidelobes" near the maximum tumor response. While these less significant responses appear to be characteristics of the tumor response, they resemble clutter in intensity. The images obtained with integration do not contain such significant responses near the tumor, and are therefore preferable.

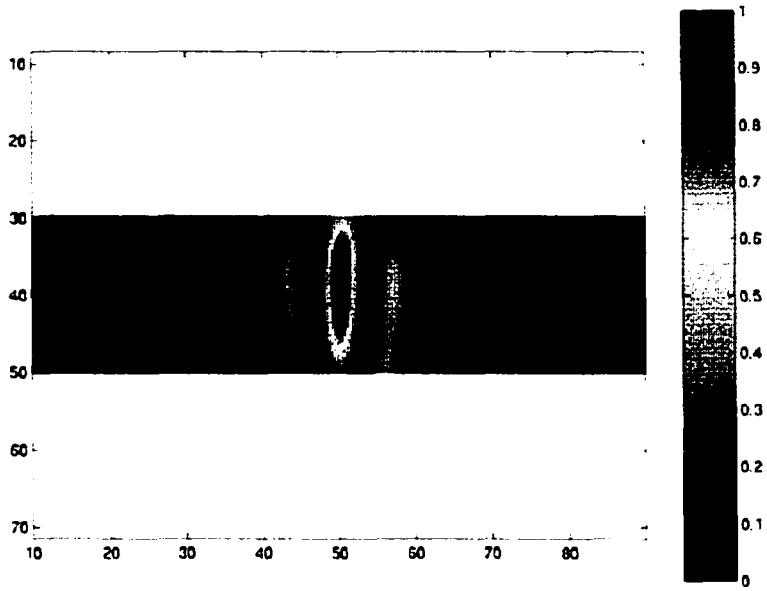

Fig. G.12. Image of y-z plane at x=64 mm. Returns at 5 rows of 10 antennas, correlation and radial spreading are used to reconstruct the image. The squared pixel values are shown, indicating that the tumor response is localized in 3D.

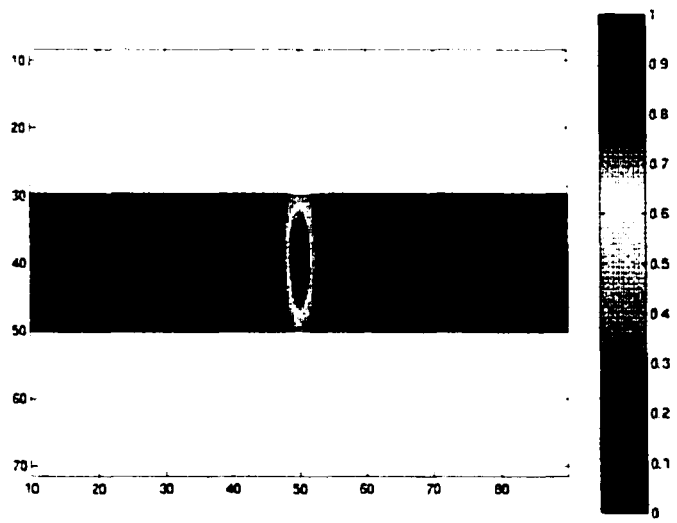

Fig. G.13. Image of y-z plane at x=64 mm. Returns at 5 rows of 10 antennas, integration and radial spreading are used to reconstruct the image. The squared pixel values are shown, indicating that the tumor response is localized in 3D.

G. 10 Tumor localization in 3D: immersion media

To test feasibility of localization of tumor responses in 3D with liquid 2, images are reconstructed for an array consisting of 9 rows of 8 antennas. Two orthogonal cuts through the maximum tumor response are shown in Fig. G.14 and Fig. G.15. The image of the remaining orthogonal plane is very similar to Fig. G.15. The tumor is well localized in the x-y plane, however the maximum response along the z-axis does not correspond well with the physical location of the tumor. This is likely due to the error in the estimated skin location, as well as the short physical span of the array. Statistics for images reconstructed with 9 rows of 8 antennas and 9 rows of 4 antennas are summarized in Table G. 14. The increase in clutter variance and decrease in signal-to-clutter ratio agree with observations made with the system immersed in liquid 1. Due to the decreased number of antennas and physical span of the array, detection is not well maintained with the array of fewer elements.

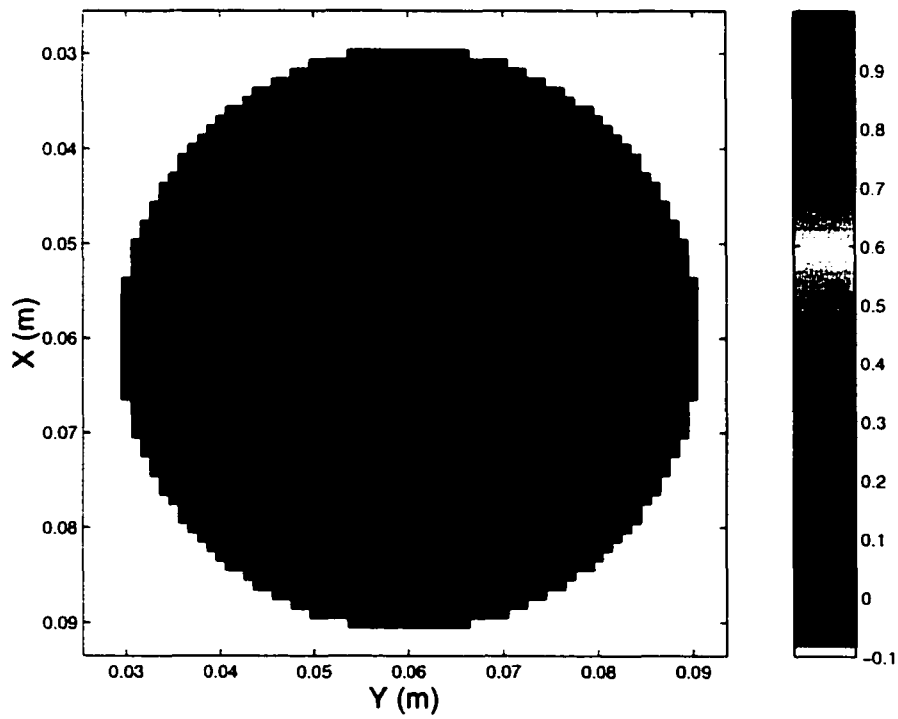

Fig. G.14. Image of plane cutting through breast model 4 at the location of the maximum tumor response. Image is reconstructed with immersion liquid 2 and a 9x8 antenna array. The tumor is located at (x=0.064, y=0.06).

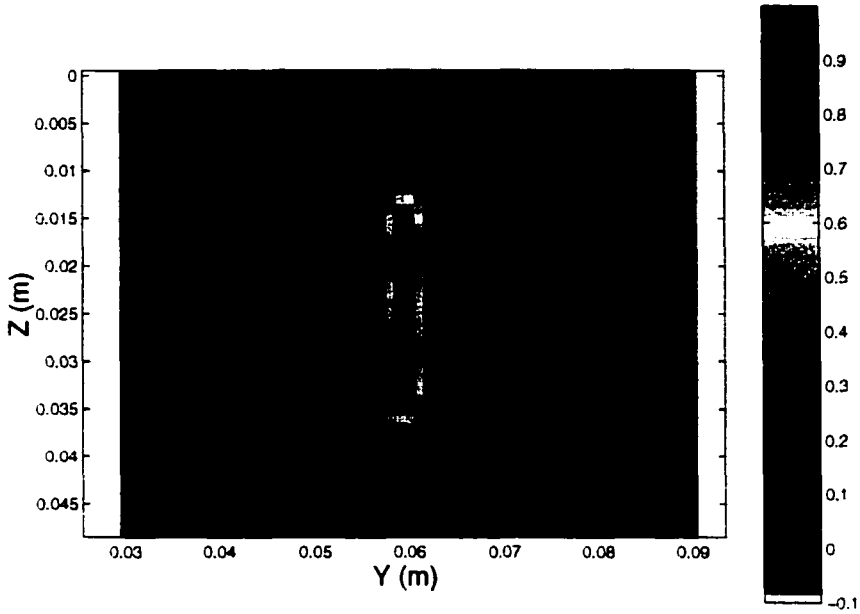

Fig. G.15. Image of plane cutting through maximum tumor response. Localization along the z direction is evident. The tumor is located at (y=0.06, z=0.025).

Table G. 14 Statistics for images in Fig. G.14 and Fig. G.15, as well as similar images reconstructed with fewer arrays.

Measure	N=72 (9 rows of 8)	N=36 (9 rows of 4)
FWHM tumor size:		
• Extent (mm)	x=4, y=4, z=24	x=4, y=5, z=23
Signal-to-clutter ratio:		
• Within breast (dB)	3.78	0.97
Clutter statistics:		
• Mean	0.0275	0.0278
• Standard deviation	0.0425	0.0552
• number of pixels	142665	144681

For a more meaningful comparison of the results obtained with the two immersion liquids, images are reconstructed with 5 rows of 10 antennas. In liquid 1, the rows are separated by 0.5 cm, while the separation is 0.25 cm in liquid 2. Statistics for the images are summarized in Table G. 15. Similar signal-to-clutter ratios are obtained. A smaller FWHM response in the z direction is obtained with liquid 1 due to the greater physical extent of the array. This larger array also results in increased variance in the clutter, however this does not appear to degrade detection ability. The larger array also provides a scan of more of the breast and provides improved localization of the tumor response.

Table G. 15 Statistics for images of breast models immersed in liquids 1 and 2. Images are reconstructed over a volume bounded by the antenna and skin locations in the x-y plane, and extending 5 mm past the maximum and minimum antenna feed locations in the z direction. Pixel size is 1 mm.

Measure	Liquid 1	Liquid 2
FWHM tumor size:		
• Extent (mm)	x=4, y=5, z=18	x=3, y=3, z=29
Signal-to-clutter ratio:		
• Within breast (dB)	6.53	6.64
Clutter statistics:		
• Mean	0.0244	0.0144
• Standard deviation	0.03	0.0206
• number of pixels	157935	147268